Doctoral Dissertations and Master's Theses

Fall 11-2018

Topology Optimization Using Load Path and Homogenization

Kaveh Gharibi
Embry-Riddle Aeronautical University

TOPOLOGY OPTIMIZATION USING LOAD PATH AND HOMOGENIZATION

A Dissertation

Submitted to the Faculty

of

Embry-Riddle Aeronautical University

by

Kaveh Gharibi

In Partial Fulfillment of the

Requirements for the Degree

of

Doctor of Philosophy in Aerospace Engineering

November 2018

Embry-Riddle Aeronautical University

Daytona Beach, Florida

TOPOLOGY OPTIMIZATION USING LOAD PATH AND HOMOGENIZATION

By

Kaveh Gharibi

This Dissertation was prepared under the direction of the candidate's Dissertation Committee Chair, Dr. Ali Tamijani, Department of Aerospace Engineering, and has been approved by the members of the dissertation committee. It was submitted to College of Engineering and was accepted in partial fulfillment of the requirements for the

Degree of
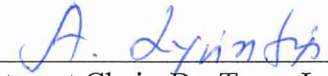
Doctor of Philosophy in Aerospace Engineering

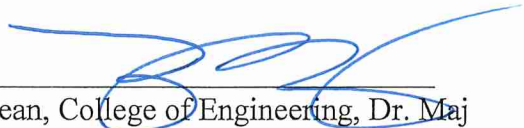## DISSERTATION COMMITTEE

Chair, Dr. Ali Tamijani

Member, Dr. Susan Davis Allen

Member, Dr. Habib Eslami

Member, Dr. Marwan Al-Haik

Department Chair, Dr. Tasos Lyrintzis

Date 11-27-2018

Dean, College of Engineering, Dr. Maj Mirmirani

Date 11-27-2018

Senior Vice President for Academic Affairs and Provost, Dr. Lon D Moeller

Date 11-28-18

DEDICATION

I dedicate this dissertation to my parents Parvaneh and Ardeshir, my sister Ghazaleh, my cousin Pardis, and my amazing grandmother Mehran Khanom for their unconditional love and their endless support and encouragement.

تقدیم به پدر و مادر عزیزم، پروانه و اردشیر، خواهرم غزاله، دخترخاله ام پردیس و مادر بزرگ عزیزم
مهران خانم بخاطر عشق و پشتیبانی بی کرانشان.

ACKNOWLEDGMENTS

TABLE OF CONTENTS

LIST OF TABLES

LIST OF FIGURES

SYMBOLS

σ_{ij}	Stress tensor
b_i	Body force
σ_{ij}^s	Solenoidal stress tensor
σ_{ij}^b	Non-Solenoidal stress tensor
δ_{ij}	Permutation symbol
ψ_x	Load path in x direction
ψ_y	Load path in y direction
ϕ	Airy stress function
Φ	Finite element shape function
D	Domain
∂D	Boundary of domain D
K_x	Stiffness matrix for load path in x
K_y	Stiffness matrix for load path in y
ξ_x	Load path in x related to body force
ξ_y	Load path in y related to body force
ρ	Density
g	Acceleration of gravity
N_{ij}	In plane Stress resultants
p_i	Pressure
Q_i	Shear resultants
Φ_x	Potential function in x direction

Φ_y	Potential function in y direction
Φ_z	Potential function in z direction
$\mathcal{J}_1$	Norm of stress integral
$\mathcal{J}_2$	Integral of sum of deviatoric principal stresses
$\lvert \sigma \rvert$	Norm of stress
Γ_N	Neumann boundary
Γ_D	Dirichlet boundary
f	Traction forces
n	Normal vector
σ_1	Maximum principal stress
σ_2	Minimum principal stress
Ω	Domain of optimization
σ_1^D	Maximum deviatoric principal stress
σ_2^D	Minimum deviatoric principal stress
t	Tangent vector
l	Lagrange multiplier for volume constraint
E	Module of elasticity
e_i	Principal stress vector
e_i^x	Principal stress vector component in x
e_i^y	Principal stress vector component in y
e^r	Dilation field
a_1, a_2	Microstructure hole dimensions

ϵ	Periodicity
h_c	Size of each microstructural cell
h_{min}	Size of minimum feature
ψ_1	Principal load path 1
ψ_2	Principal load path 2

ABBREVIATIONS

FEM	Finite element method
CFL	Courant-Fredric-Levy
PDE	Partial Differential Equation
S.t.	Subject to
det	Determinant
SIMP	Solid Isotropic Material with Penalization
ESO	Evolutionary Structural Optimization
MMA	Method of Moving Asymptote
SLP	Sequential Linear Programming

ABSTRACT

In this work, the connection between topology optimization and load transfer has been established. New methods for determining load paths in two dimensional structures, plates and shells are introduced. In the two-dimensional space, there are two load paths with their total derivative equal to the transferred load, their partial derivatives related to stress tensor, and satisfying equilibrium. In the presence of a body load the stress tensor can be decomposed into solenoidal and irrotational fields using Gurtin or Helmholtz decomposition. The load path is calculated using the solenoidal field. A novel method for topology optimization using load paths and total variation of different objective functions is formulated and implemented. This approach uses the total variation to minimize different objective functions, such as compliance and norm of stress subjected to equilibrium. Since the problems are convex, the optimized solution is a global optimum which is found by solving the Euler-Lagrange optimality criteria. The optimal density of a structure is derived using optimality criteria and optimized load paths. To attain the topology of the microstructure, the principal load paths that follow the optimal principal stress directions are calculated. Since the principal stress vector field is not curl free, a dilation field is multiplied to extract the curl free component of principal stress vectors. The principal vector field has singularities which are removed by an interpolation scheme that rotates the vectors by π to construct a coherent vector field. The optimal periodic rectangular microstructure is constructed using the load functions and microstructure dimensions. The advantage of this scheme is that using the load path reduces the equilibrium constraints from two to one, and the variables are reduced from three stresses to two load functions. The non-linear elliptic partial differential equations which are

derived from the total variation equations (Euler-Lagrange) are solved using the Gauss-Newton method which has a quadratic convergence, speeding up the convergence towards the optimal structure.

1   INTRODUCTION

In structural mechanics, the knowledge of the load paths could provide critical insights into the performance, functionality, and efficiency of the structure. The load paths in a structure help the designer to understand how the loads flow throughout the structure and ensure that the loads are transmitted and distributed according to the desired structural responses. In fact, the use of loads in design optimization can be traced back to the Michell structure, which was designed based on the total tension and total compression loads (Michell, 1904). After the emergence of numerical methods, mainly the finite element method (FEM), the design process has moved away from the calculation of internal forces and focused to a greater extent on the approximation of stress. The local stresses are aggregated into a single relationship and used as a constraint or as an objective function in most of the current design methods.

These types of approximations cause the loss of physics in the design process, which sometimes results in difficulty in determining the optimal design. Indeed, it has been proven that approximations based on internal forces in the design optimization process, which are more invariant than stresses and strains are more accurate than stress- or strain-based approximations (Vanderplaats et al., 1989; Vanderplaats et al., 1993). Despite the importance of load paths in structural mechanics, the computational structural methods (e.g., FEM, the Ritz method, and the meshless method), and as a result the commercial software (e.g., ANSYS, MSC Nastran, and ABAQUS), do not provide information regarding the load transformation throughout the structure. The existing approaches used to identify and visualize load paths are discussed in the following.

Principal stress trajectories formed the basis of the first method used to determine the load paths in structures. The principal stresses are directed along axes with null shear stresses. In this method, load paths are assumed to be tangent to the vector field of the compressive and tensile principal stresses. Although the tension and compression forces may be made constant on the principal stress trajectories with proper equivalent thicknesses, the paths along them do not, in general, describe the load transfer from applied load to reaction points.

Another method for identifying the load paths uses the direction and the trajectory of the stress pointing vectors (Kelly et al., 2011; Kelly et al., 1995; Kelly et al., 2000; Waldman et al., 2002). In this approach, the load paths are defined as curves along 'load tubes' that carry a constant load. The continuity in the load path is ensured by using the equilibrium of forces acting on the load tube. It has been shown that the stress applied on the walls of the force tubes does not contribute to the equilibrium, meaning that the sum of all forces acting on the walls is equal to zero. The Runge-Kutta algorithm is used in this method to trace the contours of the vector field.

The concept of transferred forces and potential transferred forces is also used to investigate load paths in structures (Harasaki et al., 2001). To find the transferred force in an element using this method, first the displacements of the whole structure and the load transferred to the support are calculated. The next step is to remove the element and apply the displacements that were calculated in the first step and then calculate the load that is transferred to the support. The difference between the transferred loads in these two steps is the load that is transferred through the element. Since the number of analyses is equal to the number of elements in the structure in which the transferred load is of interest, this

method requires many simulations and extensive computation time to calculate the load transfer in the entire structure. A method for load path determination was also proposed based on a compliance energy that is calculated using the transferred forces (Hoshino et al., 2003; Sakurai et al., 2007). In this method, the compliance energy was obtained according to the ratio of the reactive force with an arbitrary point in the structure unfixed and the reactive force with the point fixed when force is applied to the structure.

Therefore, the defined compliance energy quantifies the connective strength between the loading point and an arbitrary point. Recently, this method has been extended to rotational and translational six degrees of freedom instead of three translational degrees of freedom (Wang, Telichev, et al., 2017). Same authors extended this method to orthotropic composites and nonlinear materials (Wang, Pejhan, et al., 2017; Wang et al., 2016). The experimental validation of this method has also been carried out (Pejhan et al., 2017), and it has been used for different applications such as public transportation vehicles (Pejhan et al., 2018), and submarines (Shang et al., 2018).

In recent years, physical descriptions of load paths have been used to synthesize optimal compliant mechanisms (Lu et al., 2005; Santer et al., 2009). The load paths in compliant mechanisms are defined using geometric descriptions for the connectivity of the point of application and the point of support. Optimization of the compliant mechanism uses binary variables to indicate the presence or absence of a load path. This method may have a limited range of applications due to the difficulties in presenting the load paths by connectivity for continuum structures (Venkataraman et al., 2009).

In this research, the definition and formulations for load functions are introduced and the theoretical and computational foundation of an efficient and robust load path

algorithm based on the load functions are established. The proposed load function method can define the load paths and obtain the load flow using an Airy stress function for problems with available closed form solution, and can be easily integrated into the numerical approaches to provide load path contours and load flow for complex problems. Since the load paths are represented using a load function, the algorithm can provide information for sensitivity analysis in the design process. Additionally, the method introduced in this work does not need starting points to define the load paths, as are required in vector-based methods; the load paths are obtained from only a single computational analysis; and heuristic optimization is not needed in the process of determining the load paths.

Next, the load function method is extended to plates and shells. The significant difference from load function method in 2D, plates and shells is that the equilibrium equations are not divergence-free. Therefore, Helmholtz decomposition is used to decompose the stress field to divergence and curl free components to calculate the load function and find load paths. Mathematical formulations are presented to support the proposed method, and numerical and analytical examples show the application of this method.

Finally, the similarities of load path trajectory and Michell structure motivates an investigation to find the relationship of load path and structural optimization (Bouchitté et al., 2008; Kelly et al., 2000). The purpose of topology optimization is to determine the material distribution or shape and lay-out that minimizes an objective function e.g. compliance, and satisfies certain constraints such as equilibrium. The topologically optimized designs can be achieved by restricting the design space to obtain the solid-void

material distribution or relaxing the design space using microstructures or composite materials. The relaxation of the design variables is the direct results of homogenized macroscopic properties of microstructures.

The relaxation of the design variables to obtain optimized structural response was suggested by (Kohn et al., 1986a, 1986b, 1986c), and implemented in topology optimization process by (Bendsøe et al., 1988), and (Allaire et al., 1993) by using square cell with a rectangular hole and rank-two laminates, respectively. Bendsoe and Kikuchi used the strain based formulation, and Allaire and Kohn used stress based formulation to optimize structural stiffness. While for rank-two laminates the homogenized material properties can be obtained analytically, the homogenized material properties for square cell with a rectangular hole are obtained using numerical homogenization (Guedes et al., 1990).

Later, the homogenization-based topology optimization method was extended to maximize the macrostructure performance with an optimization of the microstructure using inverse homogenization through a hierarchical computational scheme (Fujii et al., 2001 ; Rodrigues et al., 2002; Sivapuram et al., 2016; Zhang et al., 2006; Zhu et al., 2016). In this method, the macroscopic distribution of material is obtained in the outer loop, while the optimized microstructures and their corresponding homogenized properties are found in the inner optimization loop. The disconnectivity between microstructures of adjacent elements arises in this method, as the connectivity of microstructures is not considered as a constraint in the optimization process.

One solution could be addressing disconnectivity issue in post-processing step, which is not only a tedious task, may result in unintended effect on objective function

and/or violating the constraints, and a structural design that would not perform as expected. Another disadvantage of separation of scales is the computational cost associated with finite element analysis for microstructure of each element. To alleviate the computational costs, parallel processing has been suggested. After determining the macroscopic distribution of material, each element can be separately analyzed to establish the optimized microstructure (Aage et al., 2017; Aage et al., 2014; Coelho et al., 2011). The use of parallel processing in multiscale topology optimization have been extended to non-linear materials (Nakshatrala et al., 2013) and laminated composites (Coelho et al., 2015). An interesting application of parallel processing in topology optimization is its application for an airplane wing with resolution of two orders of magnitude higher than usual microstructure, which resembles the bone structure of birds (Aage et al., 2017).

To address the computational issues in topology optimization of microstructures is multi scale finite element methods (MsFEM). The MsFEM has the capability of solving the equilibrium equations of composite microstructures equations with high accuracy on coarse mesh. The heterogonous nature of the composite structures causes the stiffness change drastically from one point to another, i.e. fiber to matrix. This periodic behavior can create noisy solutions. The idea is to use shape functions that capture small scale information within each element. Small scale information is brought into large scale through coupling of the global stiffness (Hou et al., 1997). The MsFEM method has been improved by (Allaire & Brizzi, 2005) through the change of variables for construction of the finite element basis, which allows a simple extension to high order finite element methods.

(Pantz et al., 2008) introduced a post-processing step to find the optimized microstructures and address the disconnectivity and computational cost issues in multiscale optimization. In this post-processing step the optimized homogenized density is determined on the macroscale and then projected on the fine mesh to find the optimized microstructures. The optimized structure is constructed as periodic square microstructure with its edges oriented in the directions of the principal stress directions. A Lagrangian is minimized for the post processing step to find two mapping functions according to the principal stress directions. Since the principal stress directions have singularities and possible sudden changes in the direction, Pantz et al. (2008) used several constraints in the Lagrangian to circumvent the principal stress directions singularities which resulted in a complex formulation.

(Groen et al., 2018) modified the method by implementing the labeling method for the principal stress directions, and thus simplifying the process of obtaining the mapping functions. In both studies, while the mapping functions are determined by minimizing the norm of gradient of the mapping functions and principal stress directions, a conformal mapping may not be generated as the principal stress direction is not necessarily a curl-free vector field. To resolve this issue, (Allaire et al., 2018) recently included the curl-free condition in the optimization process and uses covering space to address the singularities of the optimized orientation. The above mentioned post-processing methods decrease the computational costs significantly by performing the homogenization on the coarse mesh, and construction of the microstructure on the fine mesh through one finite element analysis for each mapping function.

The focus of the current study is on the optimized periodic micro-lattices that are obtained for minimized compliance and norm of stress. A lattice is a network of struts connected for the purpose of creating stiff, strong load-bearing structures using as little material as possible, to be as light as possible (Ashby, 2006). The optimization of lattice structures can be traced back to Michell truss (Graczykowski et al., 2007; Hemp, 1966; Michell, 1904) which is designed based on maximum compression and tension loads. While the Michell structures are, the optimized lattice lay-outs that transfer the load from point of application to point of support (i.e. load paths), the relationship between load paths and optimized lattice lay-outs has not been established. As mentioned earlier, understanding the load flow within a structure provide valuable insight about the performance and efficiency of the structure and can serve as a tool to measure the structural functionality of a design. However, the load flow and load paths show the existing structural functionality and are not necessary optimal for a given structure. Therefore, in this work three important questions will be studied:

(1) what is the definition of optimized load paths

(2) how optimized load paths are determined

(3) how the lattice lay-out is obtained from optimized load paths

To address these questions, the objective and constraint functions for the optimized lattice structures must be defined. Two objective functions are considered, the structural stiffness and the norm of stress, and the results are compared. The constraints include the equilibrium equations and the traction boundary conditions. Then, the stiffness of structures, norm of stress, and equilibrium equation are written in term of the load functions.

It will be shown that by using the load functions as intermediate variables the number of design variables will be reduced to two and the constraints decreased to one which result in a lower computational cost. This process will clarify the calculation of optimized load paths. Since the derived optimization formulation is convex, total variation is used to find the stationary or global optimum. Total variation of Lagrangian leads to Euler-Lagrange optimality partial differential equations (PDEs), and will lead to non-linear PDEs that are solved using finite element, and Gauss-Newton method. The convergence of the Gauss-Newton method is quadratic compared to iteratively solving the compliance problem. Next, the principle load paths are defined and linked to the optimized load paths, and utilized to find the material orientation.

In order to find the lattice layout using the principle load paths, rank-2 laminates are considered and the associated homogenized properties are written with respect to the principle stresses. To construct a mapping function from the principal load function, the singularities in the principal vector field are fixed and the vector field is converted to a coherent vector field using the tensor interpolation methods (Hotz et al., 2010). A dilation field is also used to establish the curl-free component of the principal vector field (Allaire et al., 2018). To construct the optimal orientation, the principal load paths are obtained along the reconstructed coherent vectors. Then, the principle load functions are used to project the material distribution to finite size micro-lattices, and a post processing step is implemented to remove small size members that are not manufacturable.

2   LOAD PATH IN TWO DIMENSIONAL STRUCTURES

2.1   Methodology

In this section, the derivation of the new load path identification and visualization method for plane elasticity problems is discussed. First, the structural load flow and load paths are defined. Then, the numerical approaches to solve the load functions to characterize and visualize load paths are discussed.

Definition 1. *Structural load flow is the component of internal loads, ΔF_x or ΔF_y, that is transferred from-and-to external and reaction load application points throughout the structure.*

Definition 2. *Structural load paths are the paths that trace the structural load flow (F_x or F_y enters or leaves only through the load path ends).*

To illustrate the above two definitions, consider a 2D continuum structure subjected to a traction (f_A) on the ∂D_A boundary of surface and supported on the ∂D_R boundary of surface shown in Figure 2.1 (a). The supports are removed and instead the reaction traction (f_R) is shown in Figure 2.1 (b). As can be seen Figure 2.1 (c), the reaction force is transferred to another reaction point through region Ω_1 between paths Ψ_1 and Ψ_2, and to the external force application points through region Ω_2; the external force is also divided and transferred to another external force application point through region Ω_3, and to the reaction point through region Ω_2.
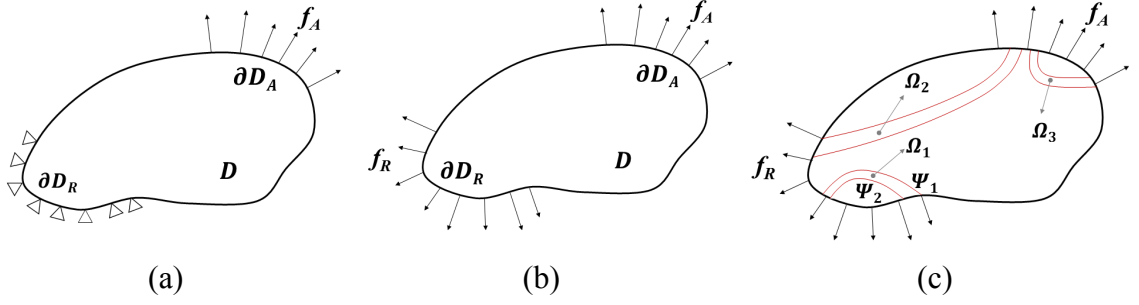
Figure 2.1 (a) Continuum structure model (b) external and reaction loads (c) load transfer in the model

Consider a plane elasticity problem subjected to boundary tractions f_A and f_R and body force b, but with no stress couples, or concentrated or distributed couples within the body. The equilibrium equations can then be written as,

$$\sigma_{ij,j} + b_i = 0 \ \text{ in } \Omega, \sigma_{ij} = \sigma_{ji} \tag{1}$$

when referred to a rectangular Cartesian frame $\boldsymbol{x} = (x_i)$. Here and in the sequel, italic indices take the values 1 or 2, the summation convention applies, Ω is the domain and $(\cdot)_{,i} \equiv \partial(\cdot)/\partial x_i$. In addition, we assume that the domain to be possibly multiply-connected with N interior boundaries $\partial \Omega = \bigcup_{\alpha=1}^{N} \partial_\alpha \Omega$, that are subject to resultants of force, $F_i^{(\alpha)}$, and moment, $M^{(\alpha)}$.

Such stress tensor admits Gurtin's decomposition of a symmetric rank two tensor (Admal et al., 2016; Fosdick et al., 2005; Fosdick et al., 2003; Gurtin, 1963):

$$\sigma_{ij} = \sigma_{ij}^S + \sigma_{ij}^b, \tag{2}$$

where σ_{ij}^S is the following totally self-equilibrated stress

$$\sigma_{ij}^S = \varepsilon_{i3n}\varepsilon_{j3q}\varphi_{,nq} \tag{3}$$

with φ the Airy function and ε_{ijk} the permutation symbol; and σ_{ij}^b is a second order

tensor (Gurtin, 1963),

$$\sigma_{kl}^b = \zeta_{k,l} + \zeta_{l,k} - \delta_{kl}\zeta_{i,i} \tag{4}$$

where δ_{kl} is the Kronecker delta, with $\zeta_i = \zeta_i^p + \zeta_i^0$ such that

$$\zeta_{k,ii}^p + b_k = 0 \ \text{ in } \Omega \tag{5}$$

$$\zeta_k^p = 0 \text{ on } \partial\Omega$$

and,

$$\zeta_k^0 = \sum_{\alpha=1}^{N} \frac{1}{2\pi} \widehat{F}_k^{(\alpha)} \ln|\boldsymbol{x} - \boldsymbol{x}^{(\alpha)}| - \frac{1}{4\pi}\left(\widehat{M}^{(\alpha)} - \varepsilon_{ij}\boldsymbol{x}^{(\alpha)}\widehat{F}_j^{(\alpha)}\right)\frac{\varepsilon_{kj}\left(x_j - x_\beta^{(\alpha)}\right)}{|\boldsymbol{x} - \boldsymbol{x}^{(\alpha)}|^2}$$

where,

$$\widehat{F}_i^{(\alpha)} \equiv -F_i^{(\alpha)} - \int_{\partial_\alpha\Omega} \zeta_{i,j}^p n_j dl \tag{6}$$

$$\widehat{M}^{(\alpha)} \equiv -M^{(\alpha)} - \int_{\partial_\alpha\Omega}\left(\varepsilon_{ij}x_i^{(\alpha)}\zeta_{j,k}^p n_k - \varepsilon_{ji}\zeta_i^p n_j\right)dl$$

If the domain is simply connected, then $\zeta_i^0 = 0$, and if the body force is null,

Gurtin's representation reduces to the usual Beltrami one. In the case of simply connected

domain where $\zeta_i^0 = 0$, the tangential derivative $d\zeta_i/ds = 0$, and ζ_i is tangent to the

boundary.

In analogy to the Helmholtz representation of vector fields, these equations

describe two components of the stress field: a solenoidal and an irrotational. The

component σ_{ij}^s is analogous to the solenoidal component of a vector field in a Helmholtz

representation and is called solenoidal (Admal et al., 2016). A solenoidal vector field, for

instance in fluid mechanics, admits a stream function and accompanying streamlines; and

streamlines have become the staple of fluid flow visualization, especially for complex

flows. The flow portrayed by streamlines let an analyst quickly locate recirculating zones,

separation lines, high shear regions, stagnation points, stagnant regions, etc. For the rank

two stress field σ_{ij}^S, not one but an infinite number of similar stream functions exist: one

for each traction associated to a fixed direction t_i, $\tau_i^t = \sigma_{ij}^S t_j$, $t_i t_i = 1$. Among that

infinite possibilities, we single out the two stream functions corresponding to tractions

that are aligned with xy frame axes. The *load functions* are defined by the following

equations:

$$\Psi_x = \frac{\partial \varphi}{\partial y}, \qquad \Psi_y = -\frac{\partial \varphi}{\partial x} \tag{7}$$

and,

$$\sigma_{xx}^S = \frac{\partial \Psi_x}{\partial y}, \qquad \sigma_{xy}^S = -\frac{\partial \Psi_x}{\partial x}, \qquad \sigma_{yy}^S = -\frac{\partial \Psi_y}{\partial x}, \qquad \sigma_{yx}^S = \frac{\partial \Psi_y}{\partial y}, \tag{8}$$

using Cauchy stress symmetry,

$$\frac{\partial \Psi_y}{\partial y} = -\frac{\partial \Psi_x}{\partial x}$$

The integration of total differential of $\Psi_x(x, y)$ and $\Psi_y(x, y)$ between two

consecutive paths (paths 1 and 2) gives,

$$\Delta \Psi_x = \Psi_{x2} - \Psi_{x1} = \int_1^2 \left(\frac{\partial \Psi_x}{\partial x} dx + \frac{\partial \Psi_x}{\partial y} dy \right)$$

$$\Delta \Psi_y = \Psi_{y2} - \Psi_{y1} = \int_1^2 \left(\frac{\partial \Psi_y}{\partial x} dx + \frac{\partial \Psi_y}{\partial y} dy \right) \tag{9}$$

By substituting Eq. (8) into Eq. (9):

$$\Delta\Psi_x = \Psi_{x2} - \Psi_{x1} = \int_1^2 \left(-\sigma_{xy}^s dx + \sigma_{xx}^s dy\right) \tag{10}$$

$$\Delta\Psi_y = \Psi_{y2} - \Psi_{y1} = \int_1^2 \left(-\sigma_{yy}^s dx + \sigma_{xy}^s dy\right) \tag{11}$$

From Figure 2.2, Eqs. (10) and (11) can be written as:

$$\Delta\Psi_x = \int_1^2 \left(-\sigma_{xy}^s dx + \sigma_{xx}^s dy\right) = \Delta F_x^s \tag{12}$$

$$\Delta\Psi_y = \int_1^2 \left(-\sigma_{yy}^s dx + \sigma_{xy}^s dy\right) = \Delta F_y^s \tag{13}$$

Similarly, if the total differential of Ψ_x and Ψ_y are evaluated on the lines which $\Psi_x = const$ and $\Psi_y = const$

$$0 = \int_{\Psi_x=const} \left(-\sigma_{xy}^s dx + \sigma_{xx}^s dy\right) = \Delta F_x^s \tag{14}$$

$$0 = \int_{\Psi_y=const} \left(-\sigma_{yy}^s dx + \sigma_{xy}^s dy\right) = \Delta F_y^s \tag{15}$$

Eqs. (12-15) show that paths of constant load functions (Ψ_x and Ψ_y) represent constant force component lines and the changes in Ψ_x and Ψ_y between their two constant paths are equal to the constant load flow of the totally self-equilibrated component of the force that is transferred between those two paths. Indeed, we have shown the following result.

There exist load functions, Ψ_x and Ψ_y, such that the changes in them between their two constant paths, $\Delta\Psi_x$ and $\Delta\Psi_y$, equals to the constant load flow of the totally self-equilibrated stresses, ΔF_x^s and ΔF_y^s, that is transferred between those two paths.

Therefore, Ψ_x and Ψ_y can be used to plot the structural load paths due to the totally self-equilibrated component of the load. In addition, in the case of a totally self-

equilibrated stress, author's load path definition and load functions agree with those of

Kelly et al. (Kelly et al., 2011), who defined the load path as the field lines of the

tractions $\overrightarrow{\tau_x} = \sigma \cdot i = \sigma_{xx}i + \sigma_{xy}j$, and $\overrightarrow{\tau_y} = \sigma \cdot j = \sigma_{xy}i + \sigma_{yy}j$.

(a)   (b)
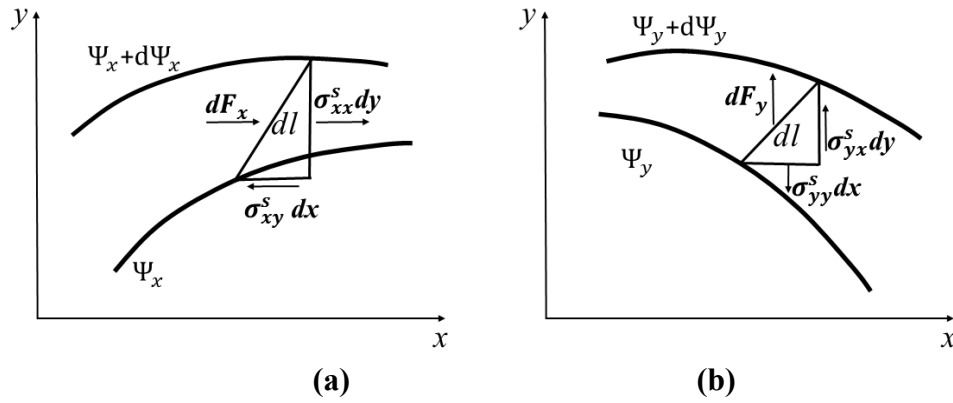
Figure 2.2 Load flow and load functions

To determine the load paths using Eq. (8), first the stress components σ_{ij}^s in the

structure should be calculated. As will be shown later in the result section, if the Airy

stress function is determined for a problem, then the load functions, and subsequently the

load paths, can be easily obtained using Eq. (7). However, for complex problems, such as

those with irregular geometry, computing the closed form of the Airy stress function

might not be feasible. In these problems, usually numerical approaches (e.g. finite

element method) are used to calculate the stresses. Therefore, a more desirable approach

is to develop a numerical method to compute the load functions from the stress

components. To do so, we use the weighted residual method. By taking the derivative of

normal stress and shear stress with respect to y and x in Eq. (8) and using the weighted

residual method, the following equation can be derived,

$$\int\int_D \left(\frac{\partial^2 \Psi_x}{\partial^2 y} + \frac{\partial^2 \Psi_x}{\partial^2 x}\right) \Phi dxdy = \int\int_D \left(\frac{\partial \sigma_{xx}^S}{\partial y} - \frac{\partial \sigma_{xy}^S}{\partial x}\right) \Phi dxdy$$

$$\int\int_D \left(\frac{\partial^2 \Psi_y}{\partial^2 y} + \frac{\partial^2 \Psi_y}{\partial^2 x}\right) \Phi dxdy = \int\int_D \left(\frac{\partial \sigma_{yx}^S}{\partial y} - \frac{\partial \sigma_{yy}^S}{\partial x}\right) \Phi dxdy$$

(16)

where Φ is the weight function. The major issue in Eq. (16) is computing the derivative

of the stress components ($\frac{\partial \sigma_{xx}^S}{\partial y}$, $\frac{\partial \sigma_{xy}^S}{\partial y}$, and $\frac{\partial \sigma_{yy}^S}{\partial y}$). These stresses are computed from the

first derivatives of the displacements, multiplied by the elasticity matrix, and are not

continuous in general over the structural domain. Since the stress field is not continuous,

determining its derivatives is a challenge. A possible solution is to remove the derivatives

on stresses and place them on the weight function (Φ) by using integration by parts on

both sides of Eq. (16):

$$-\iint_D \left(\frac{\partial \Psi_x}{\partial y}\frac{\partial \Phi}{\partial y} + \frac{\partial \Psi_x}{\partial x}\frac{\partial \Phi}{\partial x}\right) dxdy + \int_{\partial D} \left(-\frac{\partial \Psi_x}{\partial y}\Phi dx + \frac{\partial \Psi_x}{\partial x}\Phi dy\right)$$

$$= -\int\int_A \left(\sigma_{xx}^S \frac{\partial \Phi}{\partial y} - \sigma_{xy}^S \frac{\partial \Phi}{\partial x}\right) dxdy$$

$$+ \int_{\partial D} \left(-\sigma_{xx}^S \Phi dx - \sigma_{xy}^S \Phi dy\right)$$

(17)

$$-\iint_D \left(\frac{\partial \Psi_y}{\partial y}\frac{\partial \Phi}{\partial y} + \frac{\partial \Psi_y}{\partial x}\frac{\partial \Phi}{\partial x}\right) dxdy + \int_{\partial D} \left(-\frac{\partial \Psi_y}{\partial y}\Phi dx + \frac{\partial \Psi_y}{\partial x}\Phi dy\right)$$

$$= -\int\int_A \left(\sigma_{xy}^S \frac{\partial \Phi}{\partial y} - \sigma_{yy}^S \frac{\partial \Phi}{\partial x}\right) dxdy$$

$$+ \int_{\partial D} \left(-\sigma_{xy}^S \Phi dx - \sigma_{yy}^S \Phi dy\right)$$

By using the definition given in Eq. (8), Eq. (17) can be written as:

$$\iint_D \left(\frac{\partial \Psi_x}{\partial y} \frac{\partial \Phi}{\partial y} + \frac{\partial \Psi_x}{\partial x} \frac{\partial \Phi}{\partial x} \right) dxdy = \int \int_D \left(\sigma_{xx}^S \frac{\partial \Phi}{\partial y} - \sigma_{xy}^S \frac{\partial \Phi}{\partial x} \right) dxdy$$

$$\iint_D \left(\frac{\partial \Psi_y}{\partial y} \frac{\partial \Phi}{\partial y} + \frac{\partial \Psi_y}{\partial x} \frac{\partial \Phi}{\partial x} \right) dxdy = \int \int_D \left(\sigma_{xy}^S \frac{\partial \Phi}{\partial y} - \sigma_{yy}^S \frac{\partial \Phi}{\partial x} \right) dxdy$$

(18)

Now that the derivatives on the stress components are removed, solutions in the

form of $\Psi_x = \Sigma \Phi_i \psi_{xi}$ and $\Psi_y = \Sigma \Phi_i \psi_{yi}$ are used for Eq.(18). By substituting the weight

function and load functions in Eq. (18), ψ_{xi} and ψ_{yi}, can be determined,

$$[K_x]\{\Psi_{xi}\} = \{f_x\}$$

$$[K_y]\{\Psi_{yi}\} = \{f_y\}$$

(19)

where K_x and K_y are the load-path coefficient matrices that are functions of stress and

Φ_i ; Ψ_{xi} and Ψ_{yi} are the load function nodal values, and f_x and f_y are the force vectors

that are functions of the stress components and Φ_i.

The second component of the stress in Eq. (2) is the irrotational component–so

named because of its analogy with the homonymous component in the Helmholtz

decomposition of a vector field. For a vector field, the irrotational component is defined

by the gradient of a function, whereas the symmetric rank-two tensor σ_{ij}^b is defined by the

symmetric part of the gradient of a vector. In that sense, as recognized in (Admal et al.,

2016), regardless of the origin of the stress, this component is akin to the elastic stress of

a small strain field.

The irrotational component accounts for two effects: multiply-connected domains

and body forces. Let us consider the case of a simply connected domain under body

force. In this case Eq. (5) needs to be solved. Like the load function, the weighted

residual method is used to solve Eq. (5):

$$-\iint_D \left(\frac{\partial \zeta_x}{\partial y} \frac{\partial \Phi}{\partial y} + \frac{\partial \zeta_x}{\partial x} \frac{\partial \Phi}{\partial x} \right) dxdy + \int_{\partial D} \frac{\partial \zeta_x}{\partial n} \Phi ds = -\int \int_D b_x \, \Phi dxdy$$

$$-\iint_D \left(\frac{\partial \zeta_y}{\partial y} \frac{\partial \Phi}{\partial y} + \frac{\partial \zeta_y}{\partial x} \frac{\partial \Phi}{\partial x} \right) dxdy + \int_{\partial D} \frac{\partial \zeta_y}{\partial n} \Phi ds = -\int \int_D b_y \, \Phi dxdy$$

(20)

For the general case of multiply connected domains with body forces, we must compute the irrotational component σ_{ij}^b from Eqs. (4)- (6). From its definition in Eq. (4) the irrotational component is analogous to an elastic stress resulting from the small strain associated with the "displacement" ζ_i for an isotropic pseudo-material with Lamé constants $\lambda = -1$ and $\mu = 1$ (note that in a more general form of the Gurtin representation (Admal et al., 2016) these values can be set to different numbers).

This pseudo displacement is itself made of two contributions: ζ_i^p reflects the effects of the body force, whereas ζ_i^0 the effects of the multiply connectedness of the domain. The first is obtained by solving the Poisson's equation Eq. (5), and is thus analogous to the transverse displacement of a membrane subject to a pressure field; the second, is harmonic and is chosen in the form above for concreteness (Fosdick et al., 2003).

The proposed approach using Gurtin's decomposition works for both conservative and non-conservative body loads. Another approach to study the case of a simply connected domain under conservative body force is using the body force potential function. If b is conservative, $b = -\nabla V$, where V is the potential function. The equilibrium equations (Eq. (1)) can be written as (Timoshenko et al., 1951),

$$\frac{\partial}{\partial x}(\sigma_{xx} - V) + \frac{\partial \sigma_{yx}}{\partial y} = 0$$

(21)

$$\frac{\partial \sigma_{xy}}{\partial x} + \frac{\partial}{\partial y}(\sigma_{yy} - V) = 0$$

The irrotational and solenoidal components are defined as:

$$\sigma_x^b = V \quad \sigma_y^b = V$$

$$\sigma_{xx}^s = \sigma_{xx} - V = \frac{\partial \Psi_x}{\partial y} = \frac{\partial^2 \varphi}{\partial y^2}, \qquad \sigma_{xy}^s = \sigma_{xy} = -\frac{\partial \Psi_x}{\partial x} = \frac{\partial^2 \varphi}{\partial x\,\partial y}, \tag{22}$$

$$\sigma_{yy}^s = \sigma_{yy} - V = -\frac{\partial \Psi_y}{\partial x} = \frac{\partial^2 \varphi}{\partial x^2}, \qquad \sigma_{yx} = \sigma_{yx}^s = \frac{\partial \Psi_y}{\partial y} = \frac{\partial^2 \varphi}{\partial x\,\partial y},$$

$$\frac{\partial \Psi_y}{\partial y} = -\frac{\partial \Psi_x}{\partial x}$$

2.2   Results and Discussion

2.2.1   Cantilever Beam Subjected to Shear Load and Body Force

A cantilever beam with a rectangular cross section (height *2b,* and length *L=20b*) subjected to a shear force p at its free-end, and its weight (ρg) is considered (Figure 2.3). The potential function associated with the weight is $V = -\rho g y$. Based on the boundary conditions and V, the following Airy stress function is used.

$$\phi = c_1 y^5 + c_2 yx^2 + c_3 y^3 x^2 + c_4 y^3 + c_5 xy + c_6 xy^3 \tag{23}$$

The boundary conditions are:

$$\sigma_{xy}\big|_{y=\pm c} = 0, \quad \sigma_y\big|_{y=\pm c} = 0 \tag{24}$$

$$\sigma_{xy}\big|_{x=0} = p, \quad \int_{-c}^{c} \sigma_x y\, dy\,\bigg|_{x=0} = 0$$

The constants ($c_1 \text{ to } c_6$) can be determined by substituting Eq. (23) in Eq. (22), (24) and (1):

$$c_1 = \frac{\rho g}{20b^2}, \quad c_2 = \frac{3\rho g}{4}, \quad c_3 = -\frac{\rho g}{4b^2} \tag{25}$$

$$c_4 = \frac{\rho g}{15}, \quad c_5 = -\frac{3p}{4b}, \quad c_6 = -\frac{p}{4b^3}$$

The final stress field is therefore

$$\sigma_{xx} = \frac{\rho g y^3}{b^2} - \frac{3\rho g y}{5} + \frac{3Pxy}{2b^3} - \frac{3\rho g x^2 y}{2b^2} \tag{26}$$

$$\sigma_{xy} = -\frac{3\rho g x}{2} + \frac{3p}{4b} - \frac{3Py^2}{4b^3} + \frac{3\rho g x\, y^2}{2b^2}$$

$$\sigma_{yy} = \frac{\rho g y}{2} - \frac{\rho g y^3}{2b^2}$$

Let's first neglect the effect of body forces ($\rho g = 0$). From Eqs. (7) and (23), the load functions are found. Figure 2.4 (a) and (b) shows the six load paths plotted in x (Ψ_x) and y (Ψ_y) directions. The change in the Ψ_x between two consecutive load paths is $\Delta\Psi_x = -2.14\, p$. By substituting σ_{xx}, and σ_{xy} from Eq. (26) in Eq. (10), and taking the integral on a section between any pairs of load paths, we find that the x-direction load flow between each pair of load paths is also $\Delta F_x = -2.14\, p$. As shown in the x-direction load paths (Ψ_x), the load flows from one support point to another support point, and it is positive above the x-axis and negative below the x-axis. Since the load flow is equally divided between six load paths, the load flow from above and below the x-axis cancels out each other and the net x-direction load flow is zero.

The moment created by the equal load flow between each pair can be calculated by multiplying the load flow by the distance to the x-axis, which is found to be equal to the moment at the right edge boundary ($M = 20Pb$). Therefore, the x-direction load paths clearly indicate the development of bending moment and show how the load is

transferred in the structure to create it. On the other hand, the change in the Ψ_y between two y-direction load paths is $\Delta\Psi_y = p/7$. By substituting Eq. (23) in Eq. (11), the y-direction load flow between each pair of load paths is also found to be $p/7$. This finding shows how the shear load is equally divided and transferred between load paths from application edge to the support edge. Since there are six load paths plotted in Figure 2.4 (b), the applied load (p) is divided by 7, and equal load ($p/7$) is transferred from point of application to the point of support.

Next, the effect of body force in the absence of shear load is studied. The load functions and the load paths in x (Ψ_x) and y (Ψ_y) directions can be obtained using Eqs. (7) and (23). The load paths in x $-$direction are shown in Figure 2.5 (a). The self-equilibrated component of the body force ($\Delta F_x = 10.71\ \rho g$) flows between paths. Although the load paths shape in this direction are like those of shear force, the paths are closer to the fixed end due to the changes in σ_{xx} and σ_{xy}. The load paths in y $-$direction (Figure 2.5 (b)) are different than the y-direction load paths of shear load (Figure 2.4 (b)) due to the existence of σ_{yy}. By substituting σ_{yy}, and σ_{xy} from Eq. (26) in Eq. (11), we find that the y-direction load flow is $1.42\ p$.

Finally, both shear load and body force are considered. The load paths in x (Ψ_x) and y (Ψ_y) directions are shown in Figure 2.6. The x $-$direction self-equilibrated component of the body force and shear force (Figure 2.6 (a)) is found to be $\Delta F_x = 8.67\ p$. This approximately equals to the superposition of the two load flows from shear load (Figure 2.4 (a)) and body force (Figure 2.5 (a)) in $x -$ direction ($\Delta F_x = 10.71p - 2.14p$). The small difference is a round-off error which can be reduced by increasing the number of contour lines. Similarly, for the $y -$ direction load flow, the total load (Figure

2.6 (b)) can be found by subtracting the shear force load flow (Figure 2.4 (b)) from body force load flow (Figure 2.5 (b)).

The load paths for the beam subjected to the shear load and its weight can also be obtained using the Gurtin's decomposition Eqs. (3-4). First, ζ_y is obtained using Eq. (20) (Figure 2.7 (a)), and then the irrotational stress components are calculated from Eq. (4). Finally, the solenoidal stress components are found by subtracting the irrotational stress from total stress, and the load paths are determined by using Eq. (18). As can be seen in Figure 2.7 (b) and (c), the load paths corresponding to the totally self-equilibrated stress field are similar to those found using potential function (Figure 2.6). The small discrepancies between the load flows ($\Delta\Psi_y$ and $\Delta\Psi_x$) of potential function and Gurtin decomposition methods are due to the use of numerical procedure (Eqs. (18) and (20)) in latter.
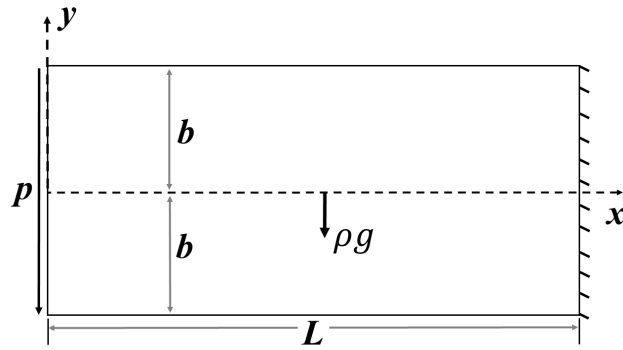
Figure 2.3 End-loaded cantilever beam
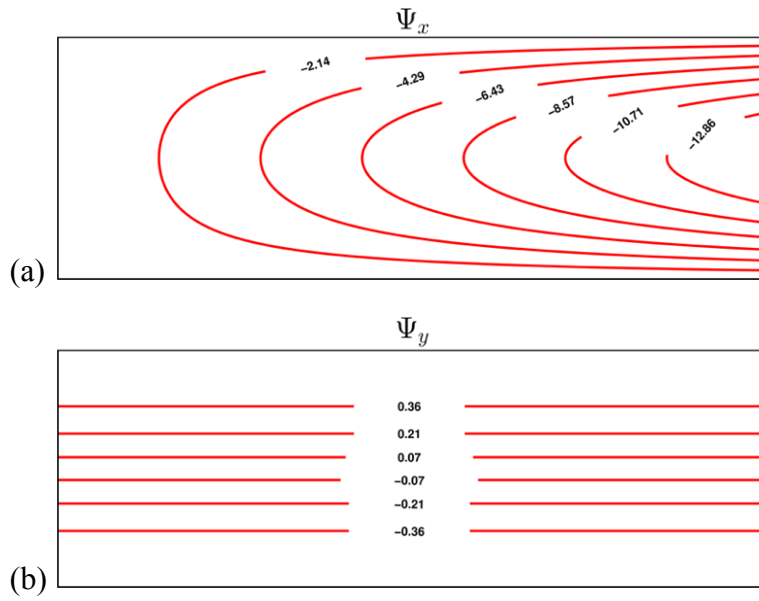
Figure 2.4 Load paths in (a) x-direction (Ψ_x) and (b) y-direction (Ψ_y) for a cantilever beam subjected to shear load in absence of body forces
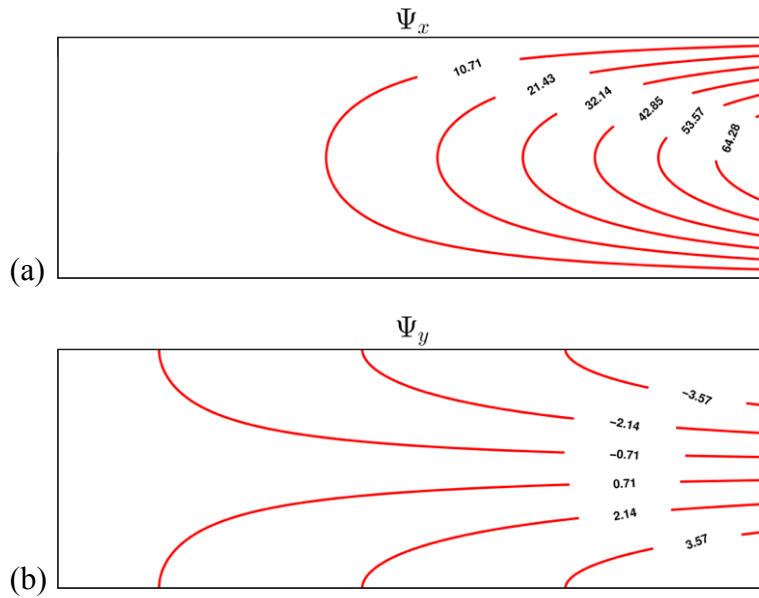
Figure 2.5 Load paths in (a) x-direction (Ψ_x) and (b) y-direction (Ψ_y) for a cantilever beam subjected to its weight
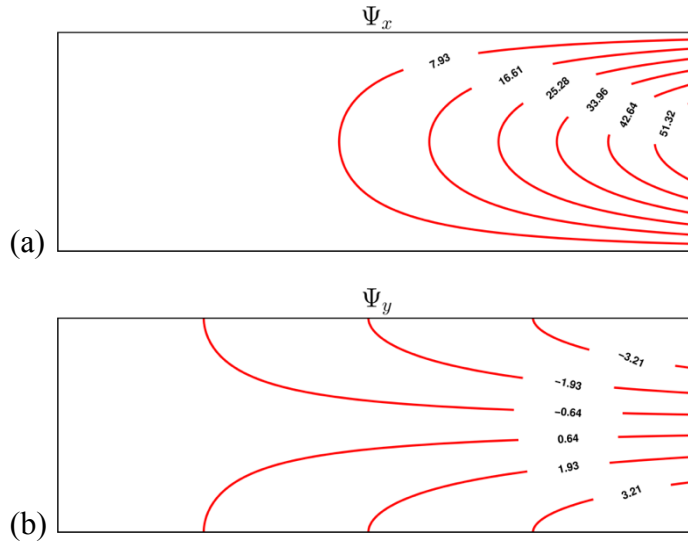
Figure 2.6 Load paths in (a) x-direction (Ψ_x) and (b) y-direction (Ψ_y) for a cantilever beam subjected to shear force and its weight
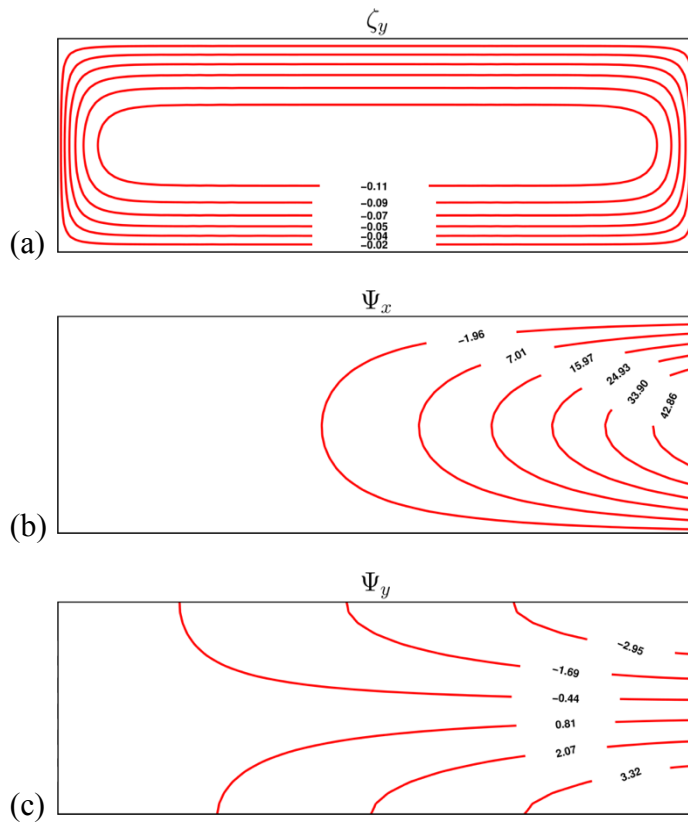
Figure 2.7 Cantilever beam subjected to shear force and its weight (a) irrotational part in y −direction (ζ_y); (b) load paths in x-direction (Ψ_x); and (c) load paths y-direction (Ψ_y) using Gurtin's decomposition

2.2.2 Plate with Hole Under Uniaxial Tension

For the second test case with a closed form solution, a plate with a small traction-free circular hole of radius a subjected to uniform tension of magnitude S in x-direction is considered (Figure 2.8). The boundary conditions imply that for large r the stress field approaches a uniaxial tension of magnitude S (i.e. $\sigma_{xx} = S, \sigma_{yy} = 0, \sigma_{xy} = 0$). The Airy stress function and the corresponding stresses for this test case are (Timoshenko et al., 1951):

$$\varphi = S\left(\frac{r^2}{4} - \frac{a^2 Ln(r)}{2}\right) + S\left(-\frac{r^2}{4} - \frac{a^4}{4r^2} + \frac{a^2}{2}\right)\cos(2\theta)$$

$$\sigma_{rr} = \frac{S}{2}\left(1 - \frac{a^2}{r^2}\right) + \frac{S}{2}\left(1 + \frac{3a^4}{r^4} - \frac{4a^2}{r^2}\right)\cos(2\theta)$$

$$\sigma_{\theta\theta} = \frac{S}{2}\left(1 + \frac{a^2}{r^2}\right) - \frac{S}{2}\left(1 + \frac{3a^4}{r^4}\right)\cos(2\theta) \tag{27}$$

$$\sigma_{r\theta} = -\frac{S}{2}\left(1 - \frac{3a^4}{r^4} + \frac{2a^2}{r^2}\right)\sin(2\theta)$$

By using Eq. (3) and then the chain rule to transform the partial derivatives of the Airy stress function to polar coordinates, the load functions can be written as:

$$\Psi_x = \frac{\partial\varphi}{\partial y} = \frac{\partial\varphi}{\partial r}\sin\theta + \frac{\partial\varphi}{r\partial\theta}\cos\theta$$

$$\tag{28}$$

$$\Psi_y = -\frac{\partial\varphi}{\partial x} = -\frac{\partial\varphi}{\partial r}\cos\theta + \frac{\partial\varphi}{r\partial\theta}\sin\theta$$

The load paths in the x and y directions (Ψ_x and Ψ_y) are shown in Figure 2.9. As was mentioned earlier, for large r the only available stress on the outer boundaries is σ_{xx}; the hole surface is traction-free, therefore, the external load can only be transferred through x-direction load paths. This can be seen in Figure 2.9, as the load path in the y

direction has wide circulations which indicates that there is no load transfer in this direction. It is quite interesting to note that the $y-$direction load paths resemble the potential fluid flow around a circular cylinder.
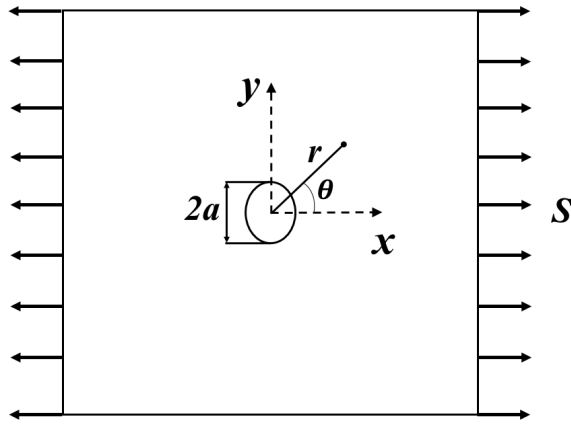
Figure 2.8 Plate with a hole under axial load
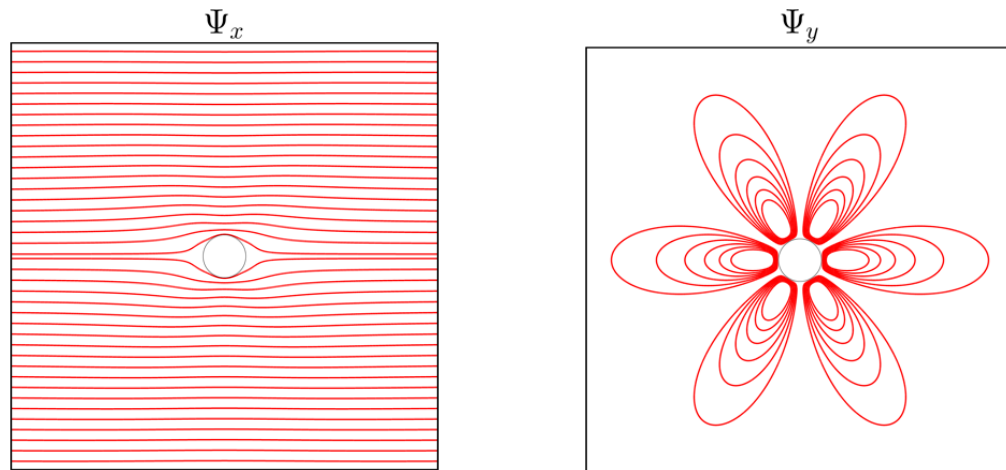
Figure 2.9 Load path in x-direction (Ψ_x) and y-direction (Ψ_y) for a plate with hole under uniaxial tension

2.2.3 Square Plate Under Shear Load

As was mentioned earlier, the stress components cannot be presented using an analytical expression for a complex system, and the load functions may not be derived using analytical approaches. In these problems, usually numerical approaches such as FEM are utilized. The present formulation associated with the determination of the load paths can be integrated into a finite element package to provide load path contours. To test and validate this, a one-sided, clamped, square plate subjected to a shear load on the right corner (Figure 2.10) was solved using FEM and the stress components are determined.

Then the stresses are substituted in Eq. (18) and load functions are obtained. To verify the accuracy of the proposed load-path functions, the plots of σ_{xx} and $\frac{\partial \Psi_x}{\partial y}$ (Figure 2.11 (a)), σ_{xy} and $-\frac{\partial \Psi_x}{\partial x}$ (Figure 2.11 (b)), and σ_{yy} and $-\frac{\partial \Psi_y}{\partial x}$ (Figure 2.11 (c)) were compared. The comparison of the results of the load function derivatives ($\frac{\partial \Psi_x}{\partial y}$, $\frac{\partial \Psi_x}{\partial x}$, and $\frac{\partial \Psi_y}{\partial x}$) with the results of the stresses determined by the finite element method (σ_{xx}, σ_{xy}, and σ_{yy}) showed the accuracy of the approximation of Ψ_x and Ψ_y.

After verification of the proposed numerical method, the load paths were determined by finding the load functions. The load functions, which demonstrate the load paths for equilibrium in the x and y directions, are shown in Figure 2.11 (d). The load paths in the y direction (Ψ_y) show how the concentrated load at the right corner is transferred and distributed to the points of support on the left edge. The Ψ_y contours also indicate that the load paths near the right corner line up with σ_{yy}, since it is the dominant

stress in this region, and as we get further from the point of application, the σ_{xy}

contribution increases and the orientation angle decreases.

As we get closer to the top and bottom left corners, the load paths are further under

the influence of σ_{yy} and the orientation angle increases. The load paths in the x direction

also provide physical insight into the load transfer and aid in understanding how various

resultant stresses are developed inside the structure. As can be seen in Figure 2.11 (d)-

Ψ_x, the load flows from one support point to another support point. As we get further

from the support edge, the load paths bend towards the point of application at the right

corner, and, at some point, they even reach the location of the concentrated load. These

two observations explain how the bending moments due to normal and shear stresses are

developed inside the structure.
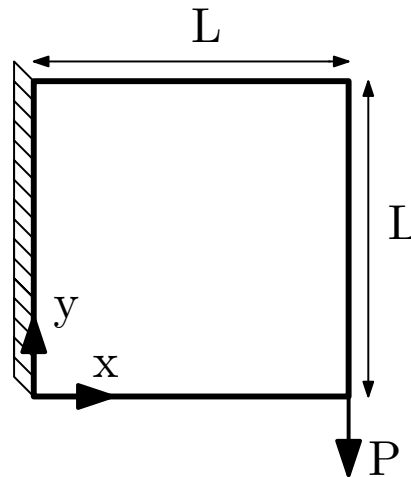
Figure 2.10 Clamped plate under shear load

(a) **(b)** **(c)** **(d)**
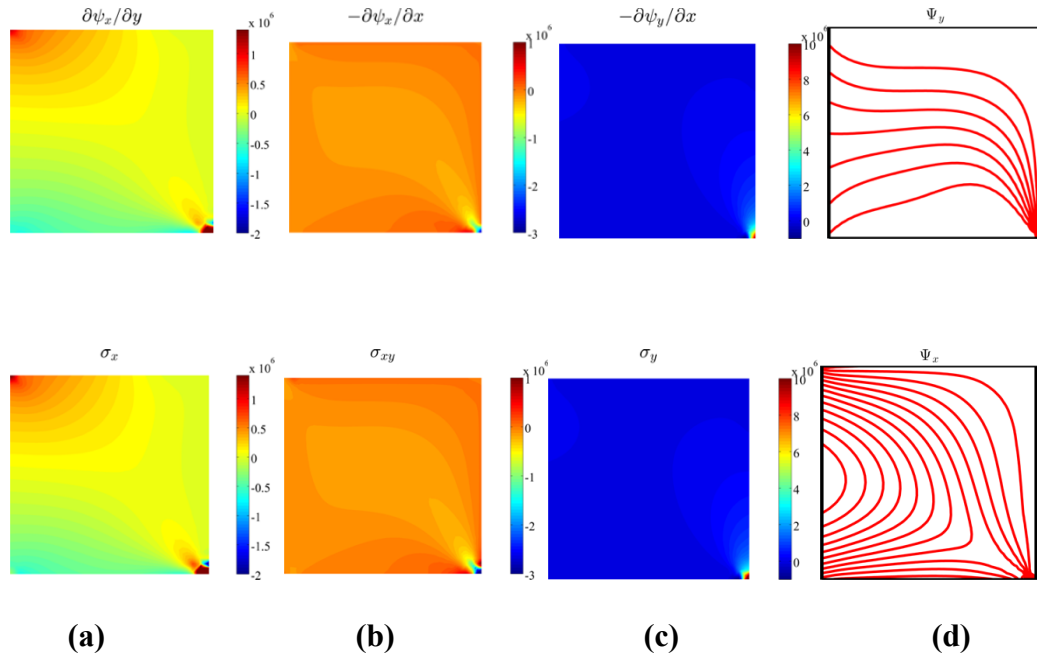
Figure 2.11 (a) Comparison of $\frac{\partial \Psi_x}{\partial y}$ and σ_{xx}; (b) Comparison of $-\frac{\partial \Psi_x}{\partial x}$ and σ_{xy}; (c) Comparison of $-\frac{\partial \Psi_y}{\partial x}$ and σ_{yy}; (d) Load paths in the y and x directions

Next, a square plat restrained at top and bottom left corners and subjected to a concentrated load at 45-degree at bottom right corner is considered (Figure 2.12). The stress components σ_{xx}, σ_{xy}, and σ_{yy} are compared with $\frac{\partial \Psi_x}{\partial y}$, $\frac{-\partial \Psi_x}{\partial x}$, and $\frac{-\partial \Psi_y}{\partial x}$ in Figure 2.13 (a), (b), and (c), respectively, and the x and y direction load paths are shown in Figure 2.13 (d). As can be seen in Figure 2.13 (d), the load paths start from the load application point and end at one of the support points instead of the entire left edge. It is also noted from Figure 2.13 (d), that the hole is deflecting the load paths, compared to those derived for the plate without hole in Figure 2.11 (c). Since the load is applied at 45-degree, the load paths in x and y directions are very similar to each other except close to the support where the x direction load paths show the bending close to the bottom corner of plate.
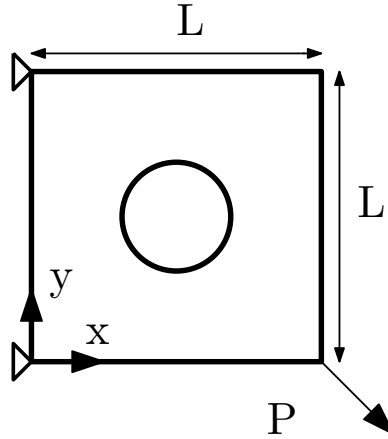
Figure 2.12 Square plate with a hole

(a)　　　　　　　(b)　　　　　　　(c)　　　　　　　(d)
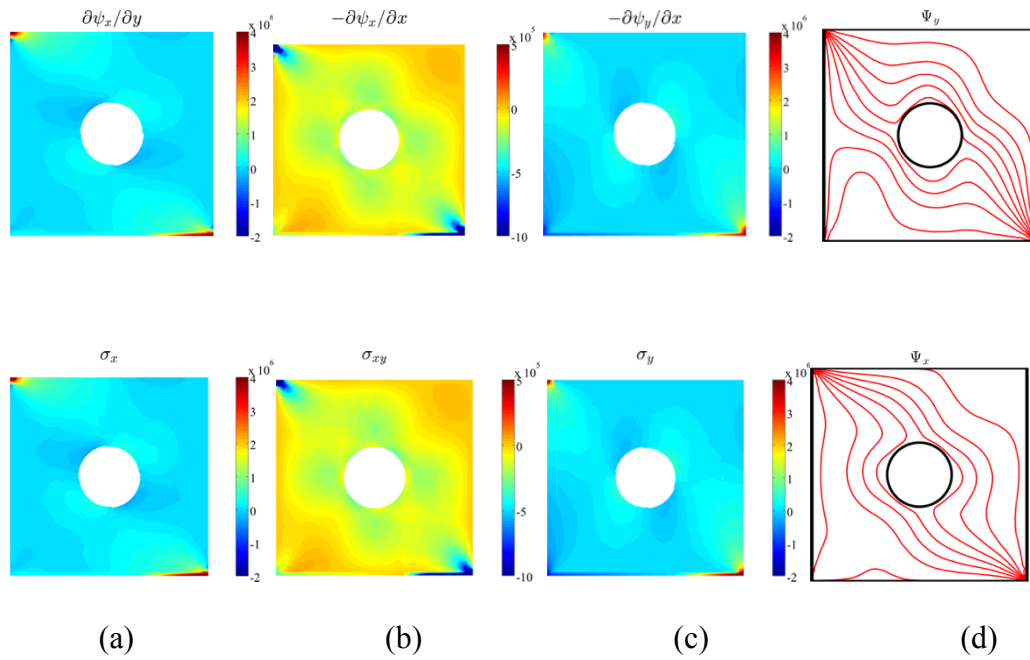
Figure 2.13 (a) Comparison of $\frac{\partial \Psi_x}{\partial y}$ and σ_{xx}; (b) Comparison of $-\frac{\partial \Psi_x}{\partial x}$ and σ_{xy}; (c) Comparison of $-\frac{\partial \Psi_y}{\partial x}$ and σ_{yy}; (d) Load paths in the y and x directions

2.2.4 Superposition of Load Functions

Since the load functions and load paths are obtained from the Poisson's equation

presented in Eq. (18), the superposition principle can be applied to them. Therefore, if the

load functions for two sets of loadings and boundary conditions are (Ψ_{x1}, Ψ_{y1}) and

(Ψ_{x2}, Ψ_{y2}), then the superposition of the two load functions ($\Psi_{x1} + \Psi_{x2}$, $\Psi_{y2} + \Psi_{y2}$) are

the load functions for the combination of two sets and satisfies the corresponding Poisson

equations:

$$\frac{\partial^2(\Psi_{x1} + \Psi_{x2})}{\partial^2 y} + \frac{\partial^2(\Psi_{x1} + \Psi_{x2})}{\partial^2 x} = \frac{\partial(\sigma_{xx1} + \sigma_{xx2})}{\partial y} - \frac{\partial(\sigma_{xy1} + \sigma_{xy2})}{\partial x}$$

$$(29)$$

$$\frac{\partial^2(\Psi_{y1} + \Psi_{y2})}{\partial^2 y} + \frac{\partial^2(\Psi_{y1} + \Psi_{y2})}{\partial^2 x} = \frac{\partial(\sigma_{xy1} + \sigma_{xy})}{\partial y} - \frac{\partial(\sigma_{yy1} + \sigma_{yy2})}{\partial x}$$

An application of the method of superposition is illustrated for the plate with a hole

when the concentrated 45-degree load is decomposed into vertical and horizontal loads

(Figure 2.14). The load paths in the x and y directions for two loading conditions are

shown in Figure 2.15 (a) and (b). By applying the superposition principle, the load paths

for the combined loading are determined. As can be seen in Figure 2.15 (a)-(b) and

Figure 2.13 (d), the superposed load paths are identical to the load paths determined for

the 45-degree load. The ability to use the superposition method for the load functions

provides the capability to break the loading into simpler components to simplify the load

path calculation of complex problems.
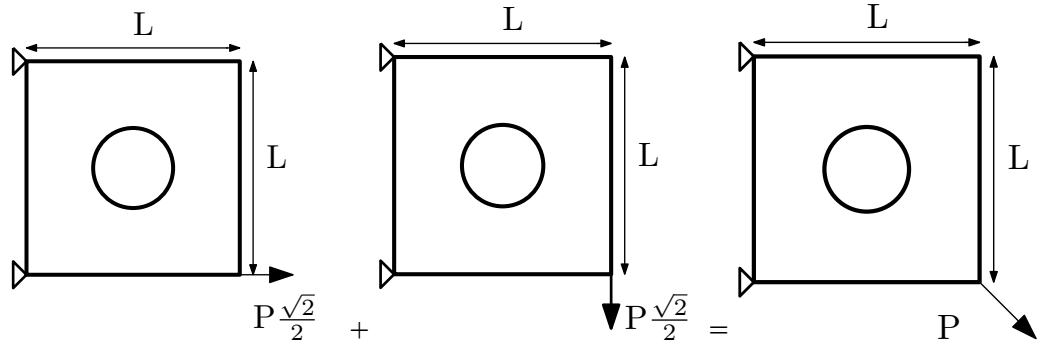
Figure 2.14 superposition of vertical and horizontal loads for the square plate with a hole
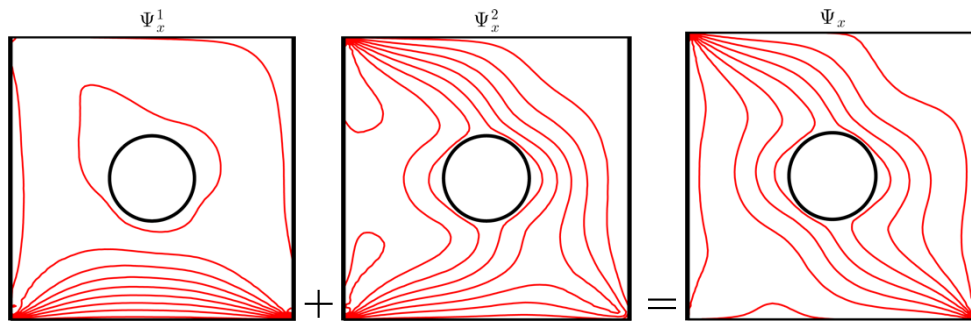
(a)
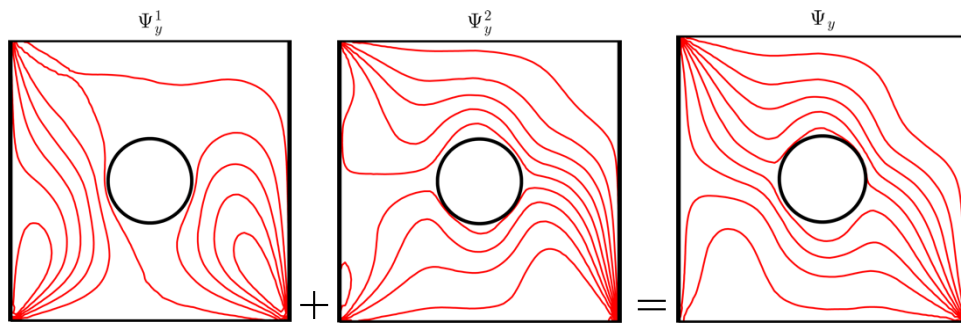
(b)

Figure 2.15 (a) x-direction and (b) y-direction load paths produced by the method of superposition

2.2.5 L-Bracket Under Shear Load

To further check the accuracy of the present formulations the load paths for an L-shaped cantilever bracket (Figure 2.16) are determined and compared with those obtained by (Kelly et al., 2011). As can be seen in Figure 2.17 (a) and (b) both load paths in the x and y directions are in good agreement with Kelly et al.'s results. The load paths in the x direction (Ψ_x) have wide circulations at the top and bottom of the L-shaped domain. These circulations show the regions that do not contribute to the load transfers in the x direction, and the load transfer in the x direction is primarily through the regions above and below the circulations. There are two sets of load paths in the y direction (Ψ_y), one set in the right region that shows how the applied load is transferred from the application point to the middle corner, and another set in the left region from one support point to another that implies the bending moment in the domain.
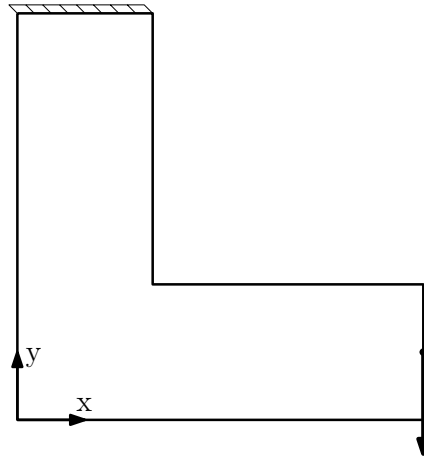
Figure 2.16 L-shaped domain under transvers load

$$\Psi_x \qquad\qquad \Psi_y$$

(a)

(b)
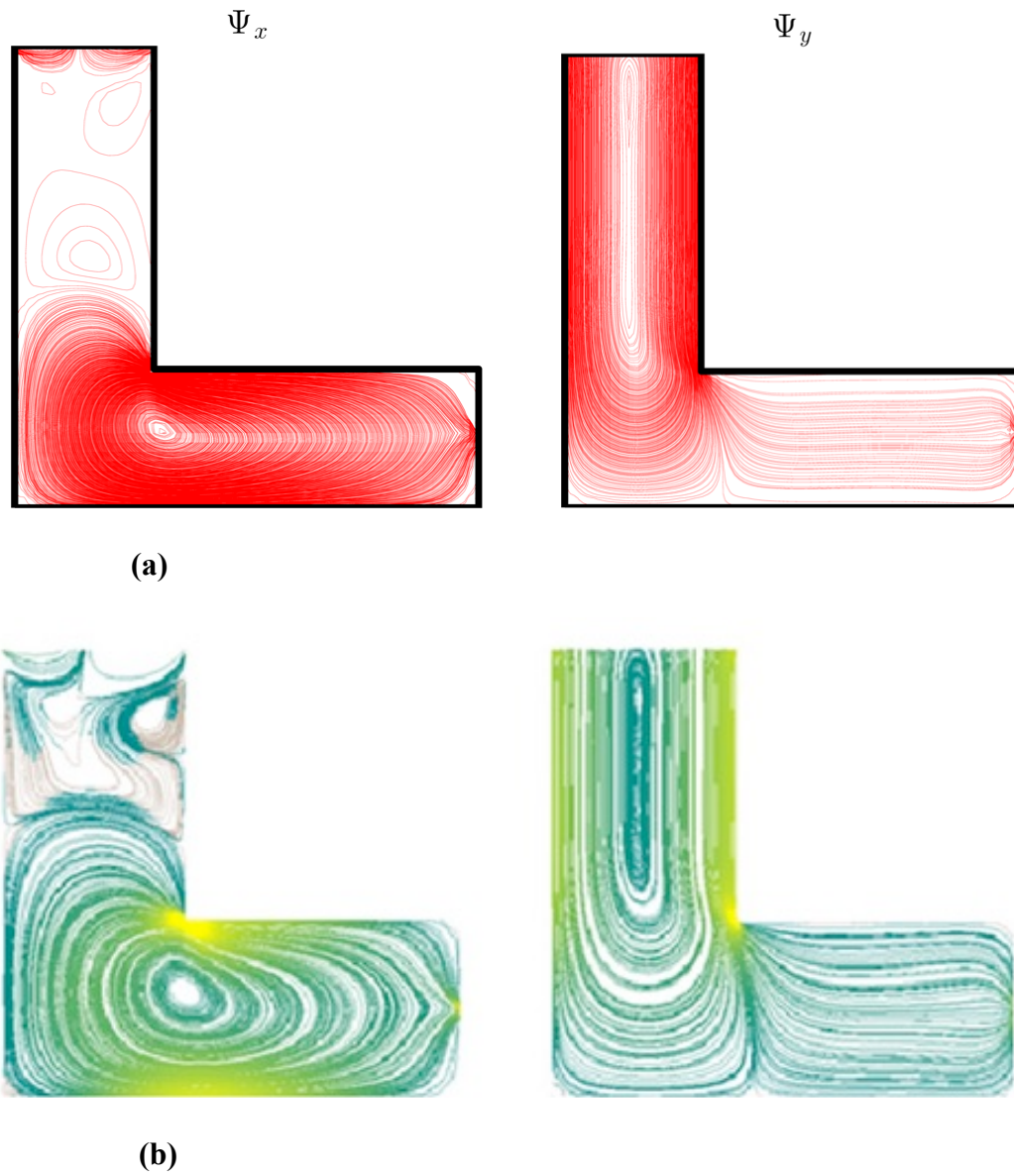
Figure 2.17 Load path in an L-bracket (a) using load paths functions (b) presented by (Kelly et al., 2011)

2.2.6   Wing Subjected to Aeroelastic Load

Because the loading and boundary conditions have not been used in any stages of the theoretical or computational development, the proposed load path algorithm should also be able to provide the load paths for any type of loading and boundary conditions, such as mechanical, thermal, and aerodynamic loads. If the numerical solver can calculate the stress components in the structure, the proposed load path algorithm can determine the load flow and load paths.

We plan to validate this through an example of a generic supersonic fighter wing under Aeroelastic loading (Locatelli, 2012). The wing plan-form is shown in Figure 2.18. The Aeroelastic analysis is conducted using the Doublet-Lattice Method and MSC-Nastran's Aeroelastic Trim analysis. The Aeroelastic pressure distribution on the aerodynamic mesh is presented in Figure 2.19 (a). The load paths in the x and y directions (i.e. $\Psi_x(x, y)$ and $\Psi_y(x, y)$) are determined by using Eq. (18) and are shown in Figure 2.19 (b) and (c). The load path in the x direction (Ψ_x) starts from the leading edge on the left side of the wing with small angle in the region close to the wing root.

The angle starts increasing closer to the wing tip, which means close to the root, σ_{xx} has a larger contribution to the load flow in the x direction, whereas, close to the tip, the load flow is the resultant of both σ_{xx} and σ_{xy} . The load path in the y direction (Ψ_y) starts from the leading edge with approximately 45-degree angle, which means the σ_{xy} and σ_{yy} have the same contribution in the y directional load transfer. It is also quite interesting to note that the pattern in the x and y directions load-paths resembles the spars and ribs patterns in a wing box.
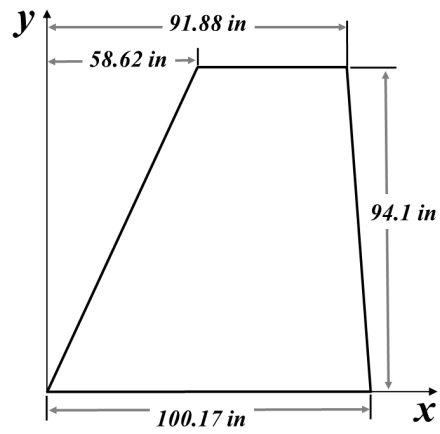
Figure 2.18 Generic supersonic fighter wing plan-form

<div align="center">(a)   (b)   (c)</div>
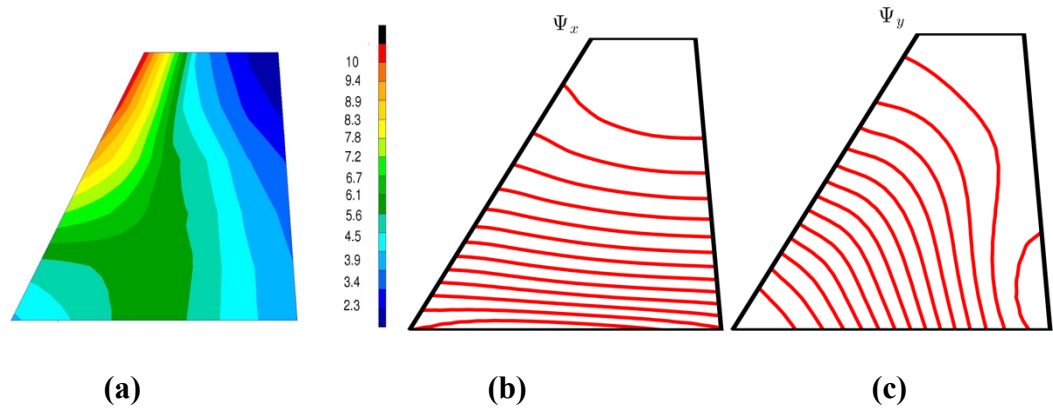
Figure 2.19 (a) Aeroelastic pressure distribution on the Aerodynamic mesh; Load paths in (b) x direction and (c) y direction for a wing plane

3   LOAD PATH IN PLATES AND SHELLS

3.1   Methodology

In the previous chapter, the load function formulation was presented for two-dimensional structures loaded in a state of plane stress and is derived from the equilibrium equations in terms of stresses (Tamijani et al., 2016). The stresses are written in terms of the load functions, and the load flow is calculated using the load function level sets. However, A problem is raised; if the stress varies with thickness so would the load paths, i.e. multiple load paths through the thickness would exist. This problem is solved by writing the equilibrium equations based on the stress resultant equilibrium equations (Gharibi et al., 2017), as in Eq. (30).

$$\frac{\partial N_x}{\partial x} + \frac{\partial N_{xy}}{\partial y} + p_x = 0$$

$$\frac{\partial N_{xy}}{\partial x} + \frac{\partial N_y}{\partial y} + p_y = 0 \tag{30}$$

$$\frac{\partial Q_x}{\partial x} + \frac{\partial Q_y}{\partial y} + p_z = 0$$

where N_x, N_{xy}, N_y, are in plane stress resultants, Q_x and Q_y are transverse shear stress resultants, and p_x, p_y, and p_z are applied pressures on surface in x, y, and z directions (Ugural, 1999). Next, the load field with respect to rectangular frame is defined as follows:

$$R_1 = N_x i + N_{xy} j$$

$$R_2 = N_{xy} i + N_y j \tag{31}$$

$$R_3 = Q_x i + Q_y j$$

Using this definition, the equilibrium equations can be written as:

$$\nabla . R + p = 0 \qquad (32)$$

where $R = [R_1\ R_2\ R_3]$, and $p = [p_x\ p_y\ p_z]$. The load vector field is decomposed into

divergence-free and curl-free components using the Helmholtz decomposition:

$$R = \nabla\Phi + \nabla\times\psi \qquad (33)$$

The decomposition concept is shown in Figure 3.1. Any vector field R, can be

decomposed to irrotational $\nabla\Phi$, and solenoidal $\nabla\times\psi$ vector fields.

$$\mathbf{R} \quad = \quad \nabla\Phi \quad + \quad \nabla\times\psi$$
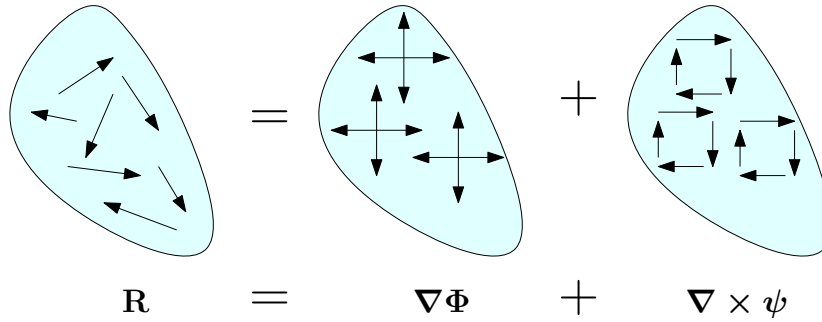
Figure 3.1 The visual representation of decomposition into solenoidal $\nabla\times\psi$ and
irrotational fields $\nabla\Phi$

In Eq. (33) the first component ($\nabla\Phi$) is the irrotational component (R^b), and the

second component ($\nabla\times\psi$) is self-equilibrated or solenoidal component (R^s). The

solenoidal vector field admits a load function ($\psi = [\Psi_x\ \Psi_y\ \Psi_z]$) and accompanying load

paths. The changes in ψ between their two paths equals to the constant load flow of the

totally self-equilibrated stress resultants ΔR^s that is transferred between those two paths.

Using the Helmholtz decomposition, first the divergence-free component (R^s) is

solved for the given boundary conditions and then the curl-free component is determined

as the residual ($R^b = R - R^s$). Given a stress resultant field, Eq. (33) can be written as:

$$\nabla\times R = \nabla\times\nabla\Phi + \nabla\times(\nabla\times\psi) \tag{34}$$

where $\nabla\times\nabla\Phi$ is zero by definition and the second term according to the vector calculus identity is as follows:

$$\nabla\times(\nabla\times\psi) = \nabla(\nabla.\psi) - \Delta\psi \tag{35}$$

Hence, using Eqs. (34), and (35), Eq. (36) is as follows:

$$\nabla\times R = \nabla(\nabla.\psi) - \Delta\psi \tag{36}$$

By using the weighted residual method, Eq. (36) can be written as:

$$-\int_\Omega \Delta\psi\, v d\Omega = \int_\Omega \nabla\times R v d\Omega \tag{37}$$

where v is the weight function, and the boundary condition associated with Eq. (37) is:

$$\frac{\partial\psi}{\partial n} = -R\times n \tag{38}$$

Using the boundary conditions, and integration by part, Eq. (37) can be written as:

$$\int_\Omega \nabla\psi\, \nabla v d\Omega = \int_\Omega R\nabla\times v d\Omega \tag{39}$$

The field lines of solenoidal components (R^s) are the level sets of ψ. After obtaining ψ, then solenoidal components can be written as:

$$R^s = \nabla\times\psi \tag{40}$$

by using the irrotational components (R^b), Φ can be found

$$\nabla\Phi = R^b = R - R^s \tag{41}$$

The integration of total differential of each load function, $e.g.\,\psi_x$, between two consecutive paths (paths 1 and 2) is as follows:

$$\Delta\Psi_x = \int_1^2 d\Psi_x = \int_1^2 \left(\frac{\partial\Psi_x}{\partial x} dx + \frac{\partial\Psi_x}{\partial y} dy \right)$$

$$= \int_1^2 (-N_{xy}^s dx + N_x^s dy) = \Delta F_x^s$$

(42)

If the differential of load function is evaluated on its constant lines, then $\Delta F_x^s = 0$, which means the solenoidal component of a load vector field in a Helmholtz representation does not pass through the level sets of load function.
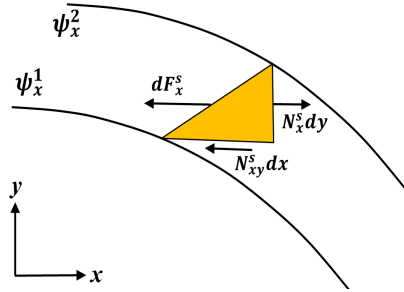
Figure 3.2 The change in ψ_x between two consecutive level sets is equivalent to the change in force between them.

For the case of general thin-shell structures, e.g. the wing or fuselage skin of an aircraft, where the normal stress through the thickness is negligible (because of plane stress in a thin walled shell), the resultant stresses (i.e. $N_{xy}, N_x, N_y, Q_x, Q_y$) must be transformed to the canonical coordinate system x-y-z (i.e. $\overline{N}_{xy}, \overline{N}_x, \overline{N}_y, \overline{Q}_x, \overline{Q}_y$) from curvilinear shell coordinate system. Assuming the shell's mid surface can be presented as $z = f(x, y)$. The transformation is as follows:

$$\overline{N}_{xy} = (N_{xy} \cos\theta - Q_x \sin\theta \cos\phi)/\cos\theta$$

$$\overline{N}_{yx} = (N_{yx} \cos\phi - Q_y \sin\phi \cos\theta)/\cos\phi$$

(43)

$$\overline{N}_x = (N_x \cos\phi - Q_x \sin\phi \cos\theta)/\cos\theta$$

$$\bar{N}_y = (N_y \cos\theta - Q_y \sin\theta \cos\phi)/cos\phi$$

$$\bar{Q}_x = (Q_x \cos\phi \cos\theta + N_x \sin\phi + N_{yx} \sin\theta)/cos\theta$$

$$\bar{Q}_y = (Q_y \cos\phi \cos\theta + N_y \sin\theta + N_{xy} \sin\phi)/cos\phi$$

where,

$$tan\,\phi = \frac{\partial z}{\partial x} \quad and \quad tan\,\theta = \frac{\partial z}{\partial y} \tag{44}$$

and, $z = f(x, y)$ represents the shell mid-surface and ϕ, and θ are the shell surface slope

with respect to canonical axis *x-y* as seen in Figure 3.3.
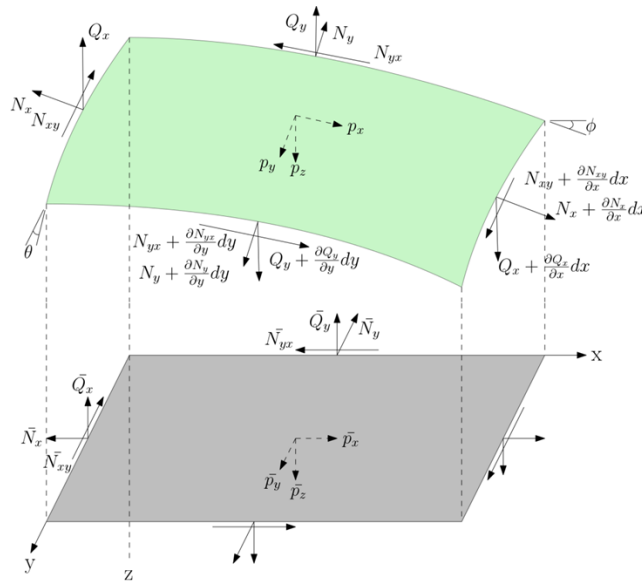
Figure 3.3 The projection of shell forces onto the *x-y* plane

The equilibrium equations based on the projected forces on the *x-y-z* plane are:

$$\frac{\partial \bar{N}_x}{\partial x} + \frac{\partial \bar{N}_{xy}}{\partial y} + \bar{p}_x = 0$$

$$\frac{\partial \bar{N}_{yx}}{\partial x} + \frac{\partial \bar{N}_y}{\partial y} + \bar{p}_y = 0 \tag{45}$$

$$\frac{\partial \bar{Q}_x}{\partial x} + \frac{\partial \bar{Q}_y}{\partial y} + \bar{p}_z = 0$$

By using the projected forces in Eq. (43), the load field can be defined as:

$$\boldsymbol{R_1} = \overline{N}_x i + \overline{N}_{xy} j$$

$$\boldsymbol{R_2} = \overline{N}_{xy} i + \overline{N}_y j \tag{46}$$

$$\boldsymbol{R_3} = \overline{Q}_x i + \overline{Q}_y j$$

Then, similar to Eq. (33), the irrotational and solenoidal components as well as load function can be obtained.

The shear force field ($\overline{Q} = \overline{Q}_x i + \overline{Q}_y j$) for any plates and shells, in general, can be decomposed as:

$$\overline{Q} = \nabla \Phi_z + \nabla \times \Psi_z \tag{47}$$

By comparing Eq. (33), the shear force components for any plate or shell can be written as follows:

$$\overline{Q}_x = \left(\frac{\partial \Phi_z}{\partial x} + \frac{\partial \Psi_z}{\partial y}\right), \qquad \overline{Q}_y = \left(\frac{\partial \Phi_z}{\partial y} - \frac{\partial \Psi_z}{\partial x}\right) \tag{48}$$

When Eq. (19) is inserted into the equilibrium equation Eq. (30), the following expression is yielded,

$$\frac{\partial^2 \Phi_z}{\partial x^2} + \frac{\partial^2 \Phi_z}{\partial y^2} = -p_z \tag{49}$$

There is an especial case of plates and not shells that will be discussed here, where $\overline{Q}_x = Q_x$, $\overline{Q}_y = Q_y$, $\overline{N}_x = N_x$, $\overline{N}_y = N_y$, $\overline{N}_{xy} = N_{xy}$, $\bar{p}_x = p_x$, $\bar{p}_y = p_y$, and $\bar{p}_z = p_z$, and Eq. (49) is similar to the plate moment equilibrium as seen in Eq. (50).

$$\frac{\partial^2 M}{\partial x^2} + \frac{\partial^2 M}{\partial y^2} = -p_z, \quad \text{where } M = \frac{M_x + M_y}{1 + v} \tag{50}$$

By comparing Eqs. (49), and (50), it is evident that the potential function, Φ_z, is

mathematically equivalent to the moment. Therefore, the values of M_x and M_y can be

used as boundary conditions for solving Eq. (49). In this situation, the contours of Φ_z are

similar to the level sets of moment function.

3.2   Results and Discussion

3.2.1   Plate Under Uniform Pressure

Assume two plates subjected to a uniform pressure, p_z, one with simply-supported

edges and the other with clamped edges (Figure 3.4). By assuming Kirchoff-Love plate

theory, we can utilize Navier's plate solution for the lateral deflection (Ugural, 1999, p.

433), w, of the simply-supported plate as,

$$w = \frac{16p_z}{D\pi^6} \sum_{n=1,3,5}^{\infty} \sum_{m=1,3,5}^{\infty} \frac{\sin\left(\frac{m\pi x}{a}\right) \sin\left(\frac{n\pi y}{b}\right)}{mn\left(\left(\frac{m}{a}\right)^2 + \left(\frac{n}{b}\right)^2\right)^2} \tag{51}$$

where D is the flexural rigidity of plate. The transverse shear resultants can be found as,

$$Q_x = -D\frac{\partial}{\partial x}\left(\frac{\partial^2 w}{\partial x^2} + \frac{\partial^2 w}{\partial y^2}\right)$$

$$= \frac{16p_z}{\pi^4} \sum_{n=1,3,5}^{\infty} \sum_{m=1,3,5}^{\infty} \frac{\left(\frac{m\pi}{a}\right)\cos\left(\frac{m\pi x}{a}\right) \sin\left(\frac{n\pi y}{b}\right)}{mn\left(\left(\frac{m}{a}\right)^2 + \left(\frac{n}{b}\right)^2\right)} \tag{52}$$

$$Q_y = -D\frac{\partial}{\partial y}\left(\frac{\partial^2 w}{\partial x^2} + \frac{\partial^2 w}{\partial y^2}\right)$$

$$= \frac{16p_z}{\pi^4}\sum_{n=1,3,5}^{\infty}\sum_{m=1,3,5}^{\infty}\frac{\left(\frac{n\pi}{b}\right)\sin\left(\frac{m\pi x}{a}\right)\cos\left(\frac{n\pi y}{b}\right)}{mn\left(\left(\frac{m}{a}\right)^2 + \left(\frac{n}{b}\right)^2\right)}$$

Additionally, the total moment sum, M, can be found as,

$$M = \frac{M_x + M_y}{1 + \nu} = -D\left(\frac{\partial^2 w}{\partial x^2} + \frac{\partial^2 w}{\partial y^2}\right)$$

$$= \frac{16p_z}{\pi^4}\sum_{n=1,3,5}^{\infty}\sum_{m=1,3,5}^{\infty}\frac{\sin\left(\frac{m\pi x}{a}\right)\sin\left(\frac{n\pi y}{b}\right)}{mn\left(\left(\frac{m}{a}\right)^2 + \left(\frac{n}{b}\right)^2\right)} \qquad (53)$$

In this example, the author's focus is on the z equilibrium equation Eq. (45) because of the special case of plates happens only in the z equilibrium. The load paths in x, and y are using the same formulation in all plates and shells structures. By using the transverse shear resultants of Eq. (52) we can see that $\nabla \times R_3 = 0$, which means $\nabla \times \nabla \times \Psi_z$ is also zero. It can then be concluded that the vector field, R_3, only has an irrotational component, R^b. The potential function can be found by using Eq. (41) by allowing $R^b = R_3$, and $R^s = 0$. Figure 3.5(a) shows the potential functions level sets compared to Figure 3.5(b), the level sets of moment function. The change in Φ_z between two level sets, $(\Delta\Phi_z)$, is $0.01229p_z$, and the ΔM is $0.01227p_z$.

Again, by utilizing Eq.(41), the potential function for plate with clamped boundary conditions can be determined. Figure 3.6(a) shows the potential function level sets compared to (b) the level sets of moment function. The gradient of Φ_z represent the curl-free component of the R_3. The $\Delta\Phi_z$ between consecutive sets of contours is $0.01430p_z$ and the ΔM is $0.01406p_z$.

This example shows three important intuitions. First, the shear resultant stresses

$(\overline{Q} = \overline{Q}_x i + \overline{Q}_y j)$ create an irrotational field $\nabla \times R_3 = 0$. It can be seen in Figure 3.5, and

Figure 3.6 that the potential function which is caused by pressure p_z, see Eq. (49), has a

non-zero gradient, i.e. $\nabla \Phi_z \neq 0$, and it is not solenoidal. This is expected since the source

term p_z generates the non-solenoidal field $\nabla . \nabla \Phi_z \neq 0$. Which can be seen in Eq. (49), i.e.

$\nabla . \nabla \Phi_z = p_z$. The Second intuition is that physical equivalent of the potential function is

the total moment transfer, i.e. $M = \frac{M_x + M_y}{1+v}$, in the structure. Third, in the case of simply

supported plate, the moment is not transferred to the supports as seen in Figure 3.5,

whereas in clamped plate the moments are transferred to the supports as seen in

Figure 3.6.

(a)   (b)
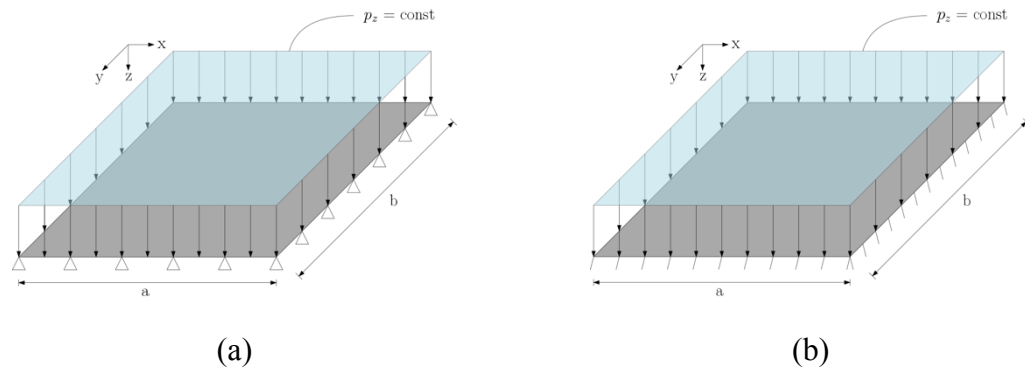
Figure 3.4 A plate subjected to a uniform pressure, p_z, with (a) simply-supported edges
and (b) clamped edges.

$$\Phi_z \qquad\qquad M$$

0.0122p_z
0.0245p_z
0.0368p_z
0.0491p_z
0.0614p_z

0.0122p_z
0.0245p_z
0.0368p_z
0.0491p_z
0.0613p_z

(a)   (b)
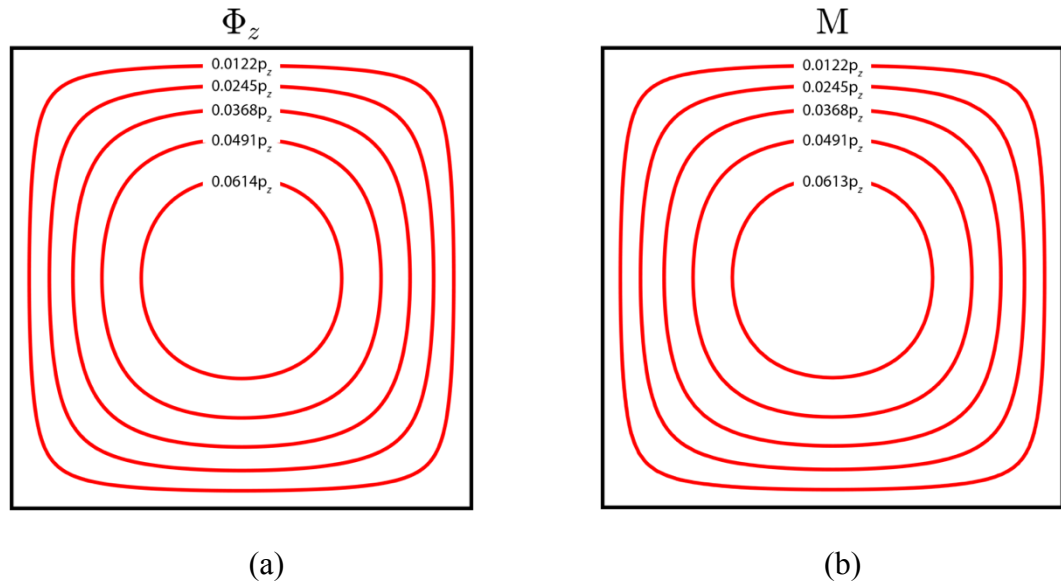
Figure 3.5 The (a) potential function level sets and (b) the level sets of total moment function for a simply-supported plate under uniform pressure, p_z

$$\Phi_z \qquad\qquad M$$

0.0362p_z
0.0219p_z
0.0076p_z
-0.0066p_z
-0.0209p_z

0.0350p_z
0.0209p_z
0.0069p_z
-0.0071p_z
-0.0212p_z

(a)   (b)
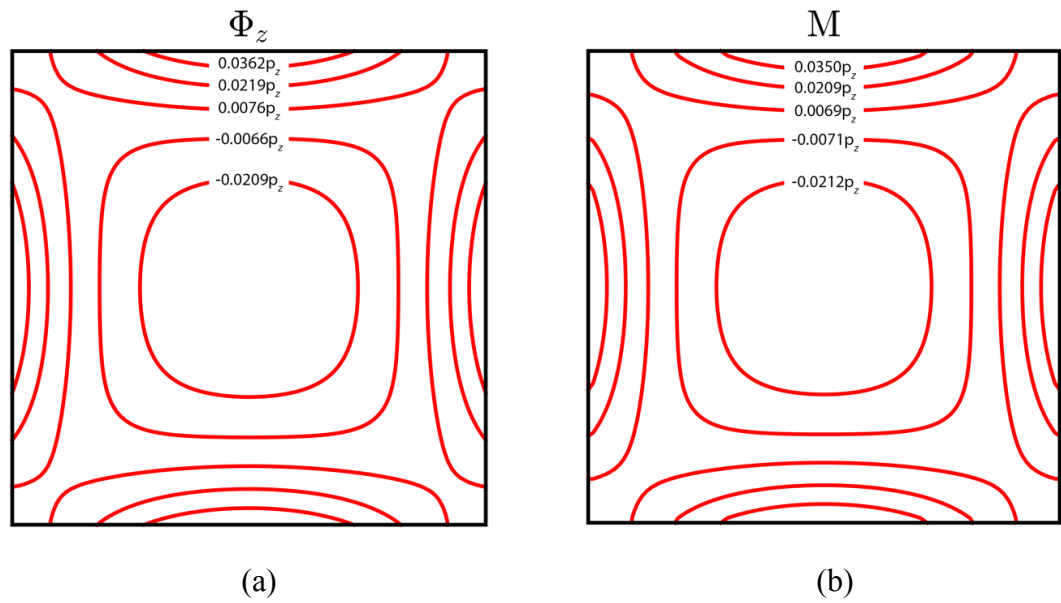
Figure 3.6 The (a) potential function level sets and (b) the level sets of total moment function for a clamped plate under uniform pressure, p_z

3.2.2   Roof Structure Subjected To Body Load

A set of panels following the form of a hyperbolic-paraboloid are pieced together to form a membrane roof structure. Figure 3.7 shows the geometry of stitched roof panel. The roof is subjected to its own weight, $p_z = \rho g$. The projected membrane forces can be described as follows (Ugural, 1999, p. 433), all edges are clamped.

$$\bar{N}_x = -\frac{\rho g y}{2} \ln \left(\frac{x + \sqrt{x^2 + y^2 + c^2}}{\sqrt{y^2 + c^2}} \right)$$

$$\bar{N}_y = -\frac{\rho g y}{2} \ln \left(\frac{x + \sqrt{x^2 + y^2 + c^2}}{\sqrt{x^2 + c^2}} \right) \tag{54}$$

$$\bar{N}_{xy} = \frac{\rho g}{2} \sqrt{x^2 + y^2 + c^2}$$

where $c = \frac{a^2}{h}$. The projected resultant stresses are plotted onto the geometry in Figure 3.8. Using Eq. (39), the load functions for the divergence-free membrane forces can be found. Figure 3.9 (a) and (b) shows the load paths for the load functions Ψ_x and Ψ_y respectively. Figure 3.10 (a) and (b) shows the contours of the potential functions Φ_x and Φ_y. The gradient of the potential functions, i.e. $\nabla \Phi_x$, and $\nabla \Phi_y$ are curl free or irrotational. Also, the curl of load functions i.e. $\nabla \times \Psi_x$, and $\nabla \times \Psi_y$ are divergence free or solenoidal.

As can be seen in Figure 3.9, the load paths (level sets of load functions Ψ_x and Ψ_y) transfer the load from one edge to the opposite side. This is shown mathematically in Eq. (42), also proofs and theorems of how load function represents load transfer can be found in previous chapter. Since the load functions i.e. Ψ_x and Ψ_y are related to the divergence free part of the equilibrium equation, and the potential functions i.e. Φ_x and Φ_y are related to the divergent part of the equilibrium, the former represents the transfer

of load due to traction on the boundary which is caused because of clamped boundary conditions, and the latter represents the load transfer due to the applied pressure. As can be seen in Figure 3.10, the level sets of potential functions Φ_x and Φ_y are transferring load from the applied pressure at the middle of the roof to the supports, whereas in Figure 3.9, the load functions Ψ_x and Ψ_y transfer load from application of traction forces on one support to another.

(a) (b)
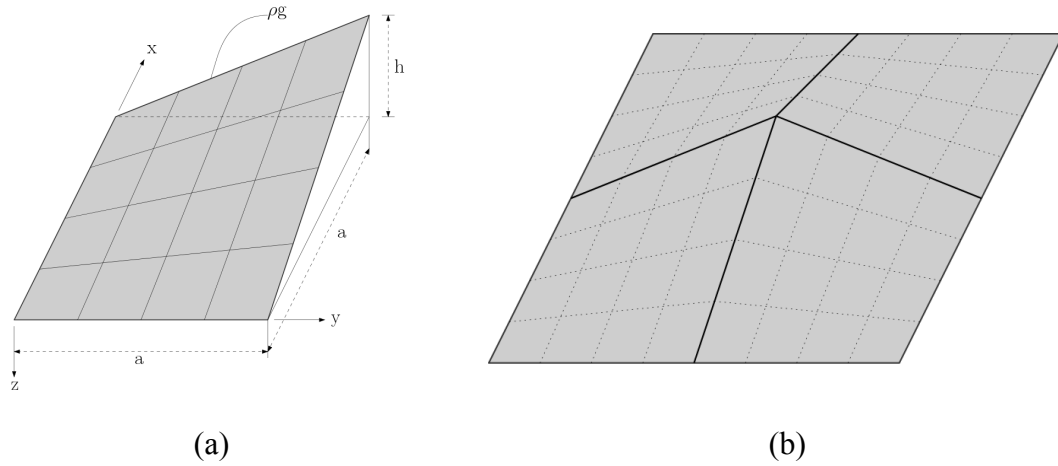
Figure 3.7 The geometry of (a) a quarter-panel and (b) the full surface of a hyperbolic-paraboloid roof structure.

(a) (b) (c)
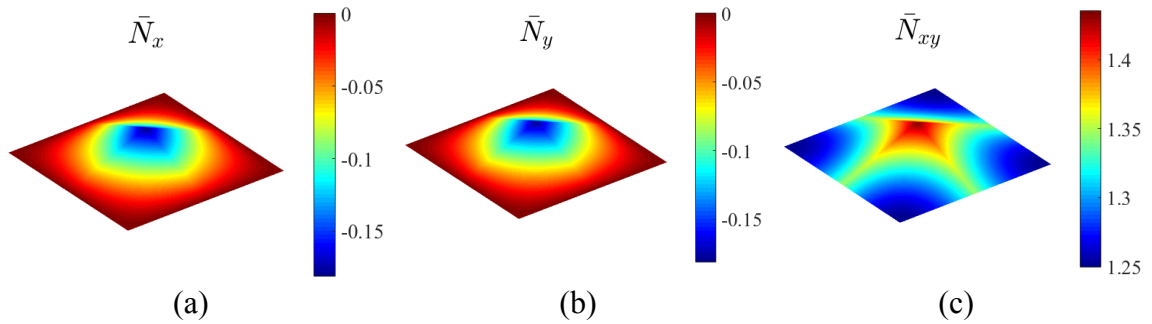
Figure 3.8 The projected shell forces from Eq. (54) showing (a) $\bar{N}_x$, (b) $\bar{N}_y$, and (c) $\bar{N}_{xy}$

$$\Psi_x \qquad\qquad \Psi_y$$

(a)   (b)
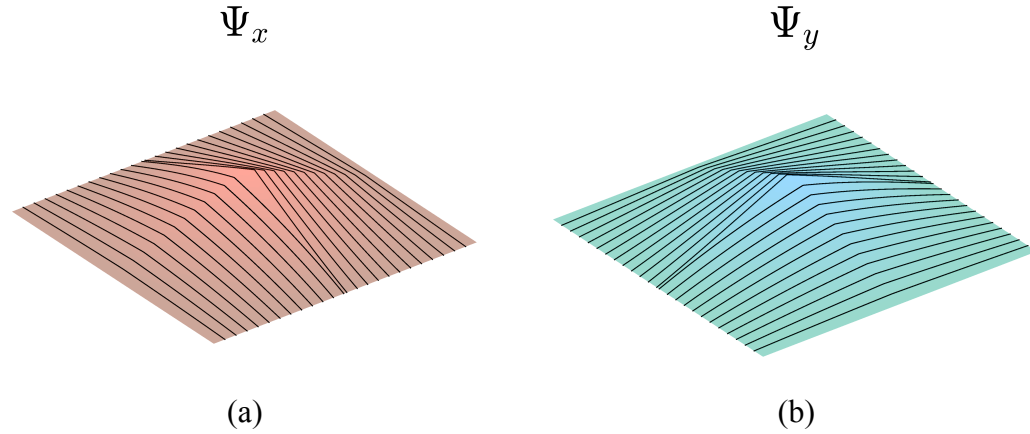
Figure 3.9 Load paths in (a) *x*-direction and (b) *y*-direction for the membrane forces of a hyperbolic-paraboloid roof under its own weight.

$$\Phi_x \qquad\qquad \Phi_y$$

(a)   (b)
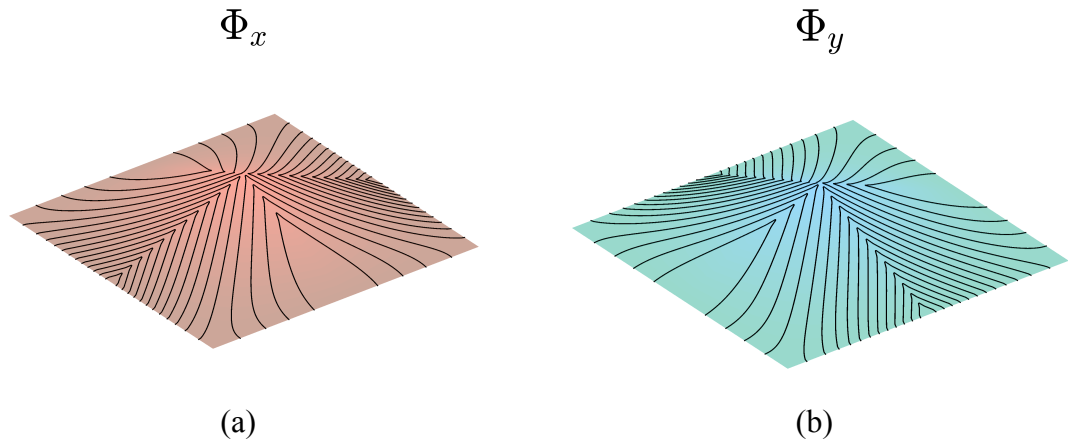
Figure 3.10 Potential function contours for (a) *x*-direction and (b) *y*-direction membrane forces of a hyperbolic-paraboloid roof under its own weight.

3.2.3   Skin Panel Subjected to Aerodynamic Loads

Assume an arbitrary wing skin panel, capable of supporting bending and membrane loads, subjected to an aerodynamic pressure load acting normal to the surface. The geometry and pressure distribution are shown in Figure 3.11. All edges are clamped. This numerical example, and one that follows, also show how the present formulation can be incorporated into numerical structural methods e.g. finite element method. Furthermore, it demonstrates that the formulation can be used regardless of the specific loading or

boundary conditions which include the possibility of internal and external loads from thermal, mechanical and aerodynamic loads. This example will also be used as a validation to show that the stress field has been decomposed into curl-free and divergence-free components. The structural solution was solved using displacement based finite element method using a pressure distribution found from vortex-lattice method. The material selected has an elastic modulus of 10^7 psi and a Poisson's ratio of 0.3.

The load functions Ψ_x, Ψ_y, and Ψ_z can be found by solving equation Eq. (39) using the stress field R which is determined by displacement based finite element. The curls of load functions represent the solenoidal component of the stress field R^s. Helmholtz decomposition implies that the curl-free forces can be found by subtraction ($R^b = R - R^s$). Figure 3.12 shows the decomposition of the (a) stress field (R) into the (b) solenoidal ($R^s = \nabla \times \psi$) and (c) curl-free ($R^b = \nabla \Phi$) components. Furthermore, it can be shown in Figure 3.12 (d) that the decomposed stress field is equivalent to the total stress field $R - (R^b + R^s) = 0$. The validation of the decomposition is to take the curl of curl-free forces ($\nabla \times R^b$) and the divergence of the divergence-free forces ($\nabla \cdot R^s$) to ensure they are zero (Figure 3.13). The load paths of Ψ_x, Ψ_y, and Ψ_z are presented in Figure 3.14 and the potential function contours of Φ_x, Φ_x, and Φ_x are presented in Figure 3.15. The load paths Ψ_x, Ψ_y, and Ψ_z are representing the solenoidal part of the solution, which is solving the equilibrium equation assuming the source term pressure is zero. The load paths i.e. level sets of Ψ_x, and Ψ_y in Figure 3.14 are transferring the load from one edge to another, and Ψ_z is transferring the moment. Ψ_x, and Ψ_y are representing the transfer of traction

loads from edge to edge. Whereas, the level sets of potential functions Φ_x, Φ_y, and Φ_z are representing the divergent equilibrium i.e. when pressure term is not zero.
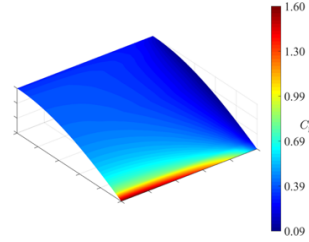
Figure 3.11 Arbitrary wing skin panel subjected to aerodynamic loading.
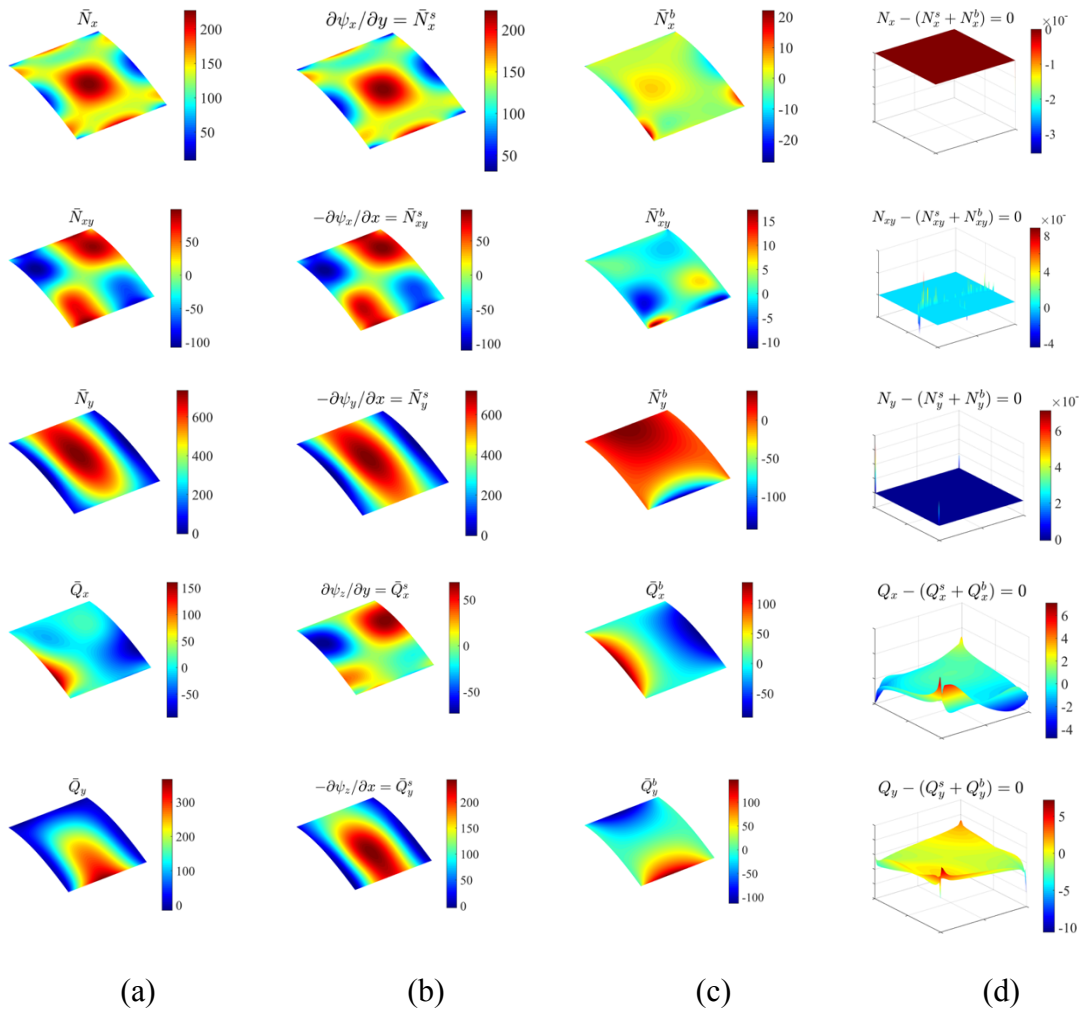
Figure 3.12 Demonstrating the decomposition of the stress field, (a) the total force, (b) the self-equilibrated component, (c) the irrotational component, and (d) the verification that they add to zero.

$\nabla \cdot \vec{N}^s = 0$ (x-dir) $\nabla \cdot \vec{N}^s = 0$ (y-dir) $\nabla \cdot \vec{Q}^s = 0$ (z-dir)

$\nabla \times \vec{N}^b = 0$ (x-dir) $\nabla \times \vec{N}^b = 0$ (y-dir) $\nabla \times \vec{Q}^b = 0$ (z-dir)

(a)   (b)   (c)
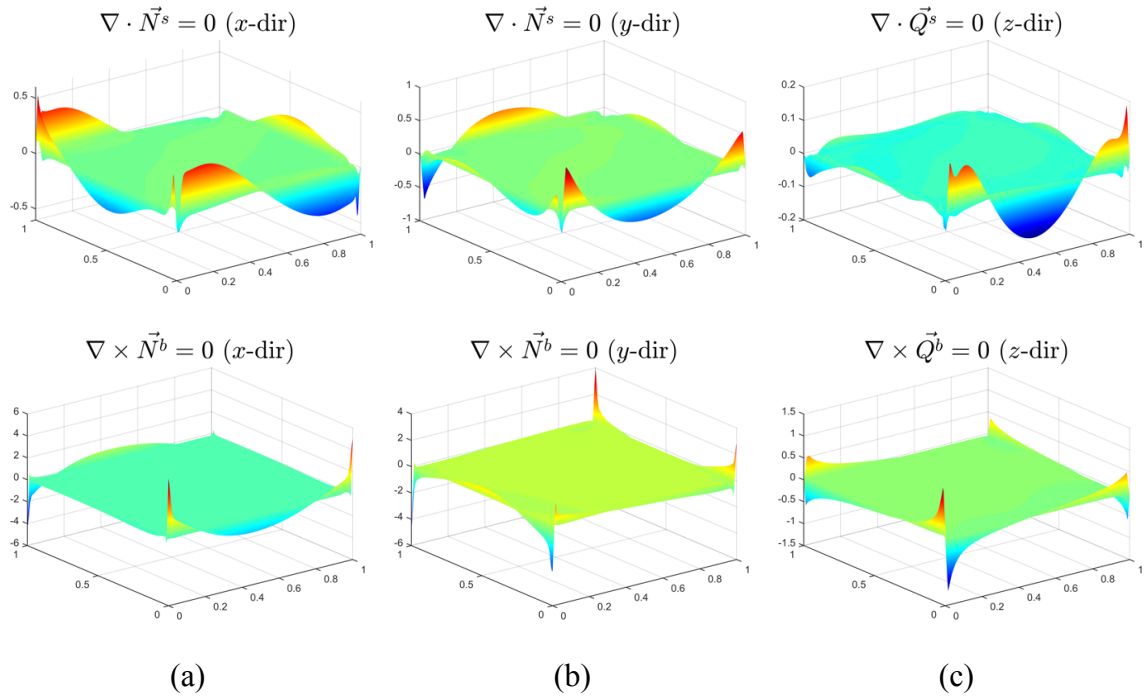
Figure 3.13 Verifying that the self-equilibrated components are divergence-free and that irrotational components are curl-free for (a) *x*-direction, (b) *y*-direction, and (c) *z*-direction forces.

Ψ_x Ψ_y Ψ_z

(a)   (b)   (c)
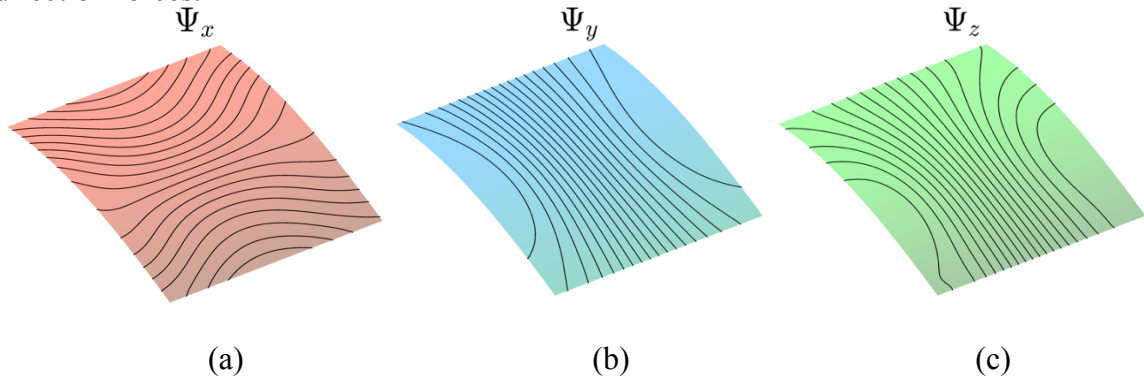
Figure 3.14 Load paths in (a) *x*-direction, (b) *y*-direction, and (c) *z*-direction for a skin panel subjected to aerodynamic loading.

Φ_x Φ_y Φ_z

(a)   (b)   (c)
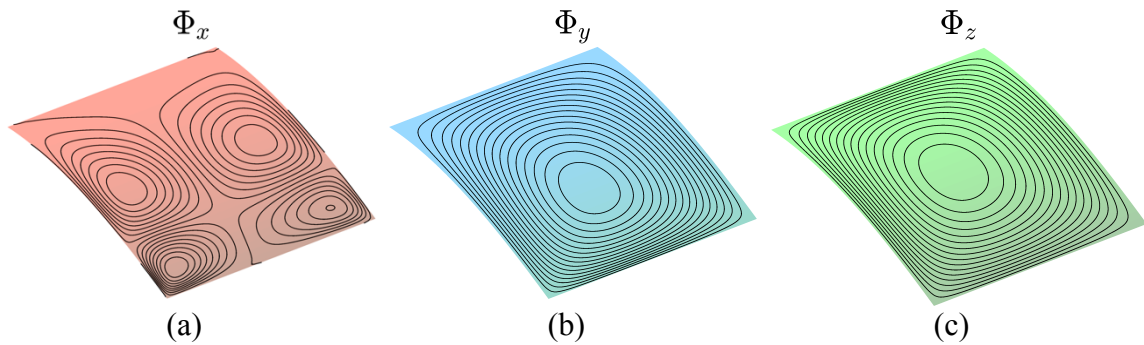
Figure 3.15 Potential function contours in (a) *x*-direction, (b) *y*-direction, and (c) *z*-direction for a skin panel subjected to aerodynamic loading.

3.2.4   Palazzetto Dello Sport Upper Dome Structure

The Palazzetto dello Sport was designed as indoor sporting arena by Pier Luigi Nervi for the 1960 Olympic games in Rome, Italy.   The upper dome structure was engineered as a thin-shell made of reinforced concrete with the inner surface overlaid with a lattice of concrete stiffeners in a radial pattern (Cutrì, 2015). The example is presented below as a thin shell dome of constant thickness, omitting the stiffeners, and supporting its own weight. A tensile modulus of 6×10^6 psi and a Poisson's ratio of 0.15 were used as material properties to model the concrete. The load paths of the functions of Ψ are shown in Figure 3.18 and the contours of the potential functions Φ are shown in Figure 3.19.
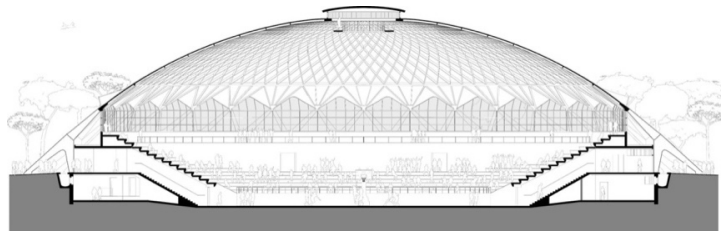
Figure 3.16 Side view of the Palazzetto dello Sport (Cutrì, 2015) .
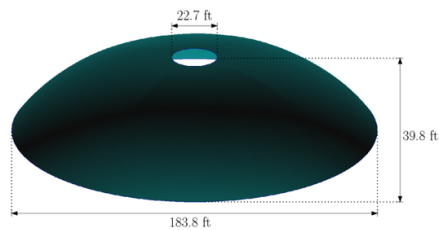
Figure 3.17 Geometry of the dome of the Palazzetto dello Sport arena.

$$\Psi_x \qquad\qquad \Psi_y \qquad\qquad \Psi_z$$

(a)   (b)   (c)
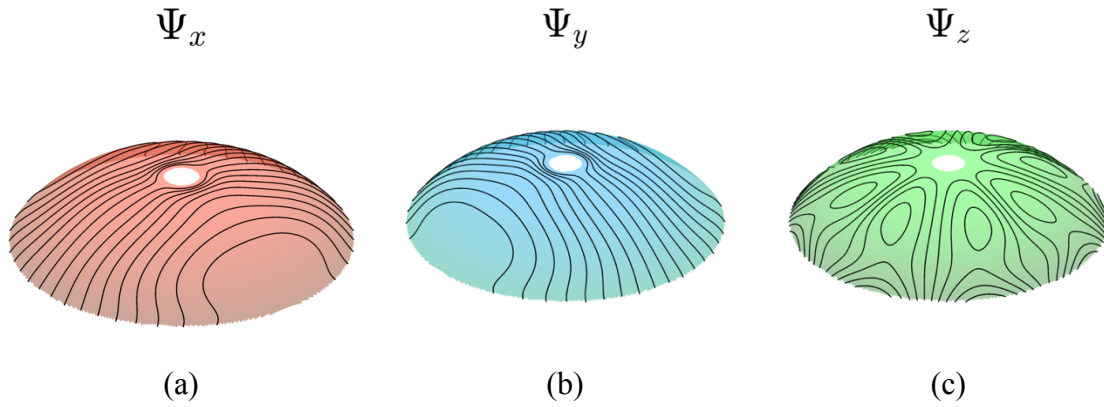
Figure 3.18 Load paths in (a) *x*-direction, (b) *y*-direction, and (c) *z*-direction for the dome of the Palazzetto dello Sport arena under its own weight.

$$\Phi_x \qquad\qquad \Phi_y \qquad\qquad \Phi_z$$

(a)   (b)   (c)
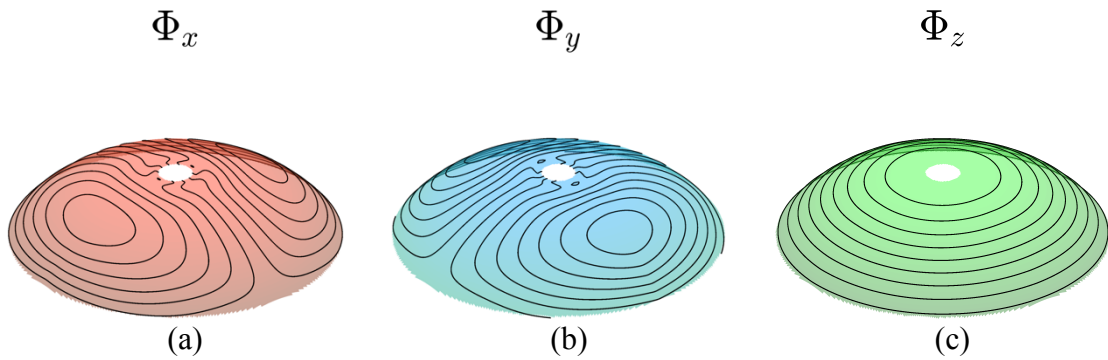
Figure 3.19 Potential function level sets in (a) *x*-direction, (b) *y*-direction, and (c) *z*-direction for the dome of the Palazzetto dello Sport arena under its own weight.

The level sets of load functions Ψ_x, and Ψ_y show the transfer of the membrane forces. The contours of the load function for the transverse shear resultants show the transfer of the bending loads from application to support. Inspection of Figure 3.18(c) shows that the level sets of the load function are similar to the stiffener reinforcement scheme selected by Nervi during design (Cutrì, 2015).

4 TOPOLOGY OPTIMIZATION USING LOAD PATH & HOMOGENIZATION

4.1 Load Path Based Optimization

The goal of this section is to develop the norm of stress and stiffness based optimization using the load function as the intermediate variables. Therefore, *the optimized load paths are defined as the load paths that minimize the norm of stress or compliance objective functions*. Assume the structure in the domain Ω is under traction loads f, and no body loads. The boundary Γ is union of Neumann, Γ_N and Dirichlet boundary conditions Γ_D. The problem statement to find the optimal structure for minimum norm of stress subjected to the equilibrium equations is as follows:

$$\min_{\sigma} \mathcal{J}_1 = \int_{\Omega} |\sigma| d\Omega \tag{54}$$

$$\text{S.t. } \nabla . \sigma = 0 \ in \ \Omega$$

$$\sigma . n = f \ on \ \Gamma_N$$

The norm of stress tensor is $|\sigma| = \sqrt{\sigma : \sigma}$ (i.e. $|\sigma_{ij}| = \sqrt{\sigma_{ij}\sigma_{ji}}; i, j = 1,2$), the integral $\mathcal{J}_1$ is on the fixed design domain Ω, and the constraints include the equilibrium equations $\nabla . \sigma = \sigma_{ij,j} = 0$, and the traction boundary conditions on Γ_N, $\sigma . n = f$, (i.e. $\sigma_{ij}n_j = f_i$), where n is the outward normal vector to the boundary Γ_N.
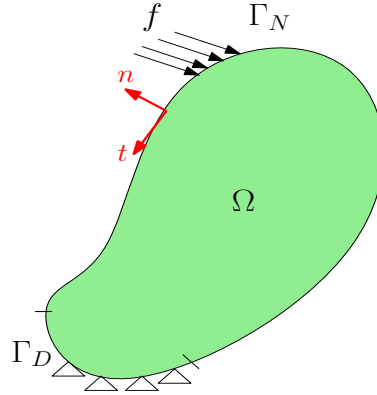
Figure 4.1 Domain Ω , the boundry conditions Γ_D, and Γ_N. Normal n and tangent t vectors to boundry

To find the optimized lattice lay-out for maximum stiffness, or alternatively minimum compliance, it is assumed each strut carries the maximum failure loads in tension or compression, and are in equilibrium. As a result, the cross section of each member is adopted to the amount of stress it is carrying, the higher the stress, the higher the cross section. Hence, the thickness of each member in the structure is proportional to the magnitude of principal stresses, $|\sigma_1|$, and $|\sigma_2|$ (Graczykowski et al., 2006). Therefore, to minimize the volume of the truss with the same limit stresses at compression and tension in the two-dimensional domain Ω, the objective function can be written as:

$$\min_{\sigma} \mathcal{J}_0 = \int_{\Omega} (|\sigma_1| + |\sigma_2|)d\Omega \tag{55}$$

subjected to equilibrium constraints,

$$\nabla.\sigma = 0 \; in \; \Omega \tag{56}$$

and satisfying the traction boundary conditions,

$$\sigma.n = f \; on \; \Gamma_N \tag{57}$$

If the limit stresses at compression and tension are equal, then the objective function in Eq. (55) can be written in terms of deviatoric stress tensor, and its principal stresses (Strang et al., 1983). In continuum mechanics, the hydrostatic pressure changes

the volume, and deviatoric stress causes the shape change. Therefore, only deviatoric part of stress is used to calculate the deformation energy $(\frac{J_2}{2})$. The compliance objective function (J_2) written in terms of deviatoric principal stresses subjected to equilibrium can be stated as follows:

$$\min_{\sigma} J_2 = \int_{\Omega} (|\sigma_1^D| + |\sigma_2^D|)d\Omega \tag{58}$$

$$\text{S.t. } \nabla.\sigma = 0 \ in \ \Omega$$

$$\sigma.n = f \ on \ \Gamma_N$$

Based on the our load path formulation (Tamijani et al., 2017; Tamijani et al., 2018), the stresses are written in terms of load functions in Eq. (59). This reduces the equilibrium equations from two to one, and the variables from three stresses $(\sigma_x, \sigma_y, \sigma_{xy})$ to two load functions $(\psi_x \ and \ \psi_y)$.

$$\sigma_{xy} = -\frac{\partial \psi_x}{\partial x}, \qquad \sigma_x = \frac{\partial \psi_x}{\partial y}$$

$$\sigma_y = -\frac{\partial \psi_y}{\partial x}, \qquad \sigma_{xy} = \frac{\partial \psi_y}{\partial y} \tag{59}$$

By using Eq. (59) the norm of stress and deviatoric principal stresses objective functions are written in terms of load functions:

$$|\sigma|^2 = \sigma_x^2 + \sigma_y^2 + 2\sigma_{xy}^2 \tag{60}$$

$$= |\nabla \psi_x|^2 + |\nabla \psi_y|^2$$

$$|\sigma_1^D| + |\sigma_2^D| = \sqrt{(\sigma_x - \sigma_y)^2 + 4\tau_{xy}^2} = \sqrt{\left(\frac{\partial \psi_x}{\partial y} + \frac{\partial \psi_y}{\partial x}\right)^2 + 4\left(\frac{\partial \psi_y}{\partial y}\right)^2} \tag{61}$$

Then, the minimization problem of norm of stress tensor, in terms of load functions becomes:

$$\min_{\psi_x, \psi_y} \mathcal{J}_1 = \int_\Omega \sqrt{|\nabla\psi_x|^2 + |\nabla\psi_y|^2}\, d\Omega \tag{62}$$

$$S.t. \quad \frac{\partial\psi_x}{\partial x} + \frac{\partial\psi_y}{\partial y} = 0$$

$$\psi_x = g_1 \text{ on } \Gamma_N$$

$$\psi_y = g_2 \text{ on } \Gamma_N$$

$$\lambda = 0 \text{ on } \Gamma_D$$

For the stiffness based optimization, the formulation becomes:

$$\min_{\psi_x, \psi_y} \mathcal{J}_2 = \int_\Omega \sqrt{\left(\frac{\partial\psi_x}{\partial y} + \frac{\partial\psi_y}{\partial x}\right)^2 + 4\left(\frac{\partial\psi_y}{\partial y}\right)^2}\, d\Omega \tag{63}$$

$$S.t. \quad \frac{\partial\psi_x}{\partial x} + \frac{\partial\psi_y}{\partial y} = 0$$

$$\psi_x = g_1 \text{ on } \Gamma_N$$

$$\psi_y = g_2 \text{ on } \Gamma_N$$

$$\lambda = 0 \text{ on } \Gamma_D$$

To solve these two minimization problems, total variation of the Lagrangian must be stationary which leads to Euler-Lagrange optimality equations. The Lagrangian corresponding to the norm of stress $\mathcal{J}_1$, and stiffness based optimization formulation $\mathcal{J}_2$ are constructed as follows:

$$\mathcal{L}_1(\psi_x, \psi_y, \lambda) = \sqrt{|\nabla\psi_x|^2 + |\nabla\psi_y|^2} - \lambda\left(\frac{\partial\psi_x}{\partial x} + \frac{\partial\psi_y}{\partial y}\right) \tag{64}$$

$$\mathcal{L}_2(\psi_x, \psi_y, \lambda) = \sqrt{\left(\frac{\partial \psi_x}{\partial y} + \frac{\partial \psi_y}{\partial x}\right)^2 + 4\left(\frac{\partial \psi_y}{\partial y}\right)^2}$$

$$- \lambda\left(\frac{\partial \psi_x}{\partial x} + \frac{\partial \psi_y}{\partial y}\right)$$

(65)

and the Euler-Lagrange equations for $\mathcal{L}_1$ and $\mathcal{L}_2$ are:

$$\frac{\partial}{\partial x}\left(\frac{\frac{\partial \psi_x}{\partial x}}{\sqrt{|\nabla \psi_x|^2 + |\nabla \psi_y|^2}} - \lambda\right) + \frac{\partial}{\partial y}\left(\frac{\frac{\partial \psi_x}{\partial y}}{\sqrt{|\nabla \psi_x|^2 + |\nabla \psi_y|^2}}\right) = 0$$

$$\frac{\partial}{\partial x}\left(\frac{\frac{\partial \psi_y}{\partial x}}{\sqrt{|\nabla \psi_x|^2 + |\nabla \psi_y|^2}}\right) + \frac{\partial}{\partial y}\left(\frac{\frac{\partial \psi_y}{\partial y}}{\sqrt{|\nabla \psi_x|^2 + |\nabla \psi_y|^2}} - \lambda\right) = 0$$

$$\frac{\partial \psi_x}{\partial x} + \frac{\partial \psi_y}{\partial y} = 0$$

(66)

$$\frac{\partial}{\partial x}\left(\frac{2\frac{\partial \psi_x}{\partial x}}{\sqrt{\left(\frac{\partial \psi_x}{\partial y} + \frac{\partial \psi_y}{\partial x}\right)^2 + 4\left(\frac{\partial \psi_y}{\partial y}\right)^2}} - \lambda\right)$$

$$+ \frac{\partial}{\partial y}\left(\frac{\frac{\partial \psi_x}{\partial y} + \frac{\partial \psi_y}{\partial x}}{\sqrt{\left(\frac{\partial \psi_x}{\partial y} + \frac{\partial \psi_y}{\partial x}\right)^2 + 4\left(\frac{\partial \psi_y}{\partial y}\right)^2}}\right) = 0$$

(67)

$$\frac{\partial}{\partial x}\left(\frac{\frac{\partial \psi_x}{\partial y}+\frac{\partial \psi_y}{\partial x}}{\sqrt{\left(\frac{\partial \psi_x}{\partial y}+\frac{\partial \psi_y}{\partial x}\right)^2+4\left(\frac{\partial \psi_y}{\partial y}\right)^2}}\right)$$

$$+\frac{\partial}{\partial y}\left(\frac{2\frac{\partial \psi_y}{\partial y}}{\sqrt{\left(\frac{\partial \psi_x}{\partial y}+\frac{\partial \psi_y}{\partial x}\right)^2+4\left(\frac{\partial \psi_y}{\partial y}\right)^2}}-\lambda\right)=0$$

$$\frac{\partial \psi_x}{\partial x}+\frac{\partial \psi_y}{\partial y}=0$$

In order to solve the Euler-Lagrange equations, the boundary conditions are converted from stresses to load functions (i.e. ψ_x, and ψ_y) as elaborated in the following:

$$\sigma.n = f$$

$$\begin{bmatrix} \sigma_x & \sigma_{xy} \\ \sigma_{xy} & \sigma_y \end{bmatrix}\begin{bmatrix} n_x \\ n_y \end{bmatrix}=\begin{bmatrix} f_x \\ f_y \end{bmatrix}$$

$$\begin{bmatrix} \dfrac{\partial \psi_x}{\partial y} & -\dfrac{\partial \psi_x}{\partial x} \\ \dfrac{\partial \psi_y}{\partial y} & -\dfrac{\partial \psi_y}{\partial x} \end{bmatrix}\begin{bmatrix} n_x \\ n_y \end{bmatrix}=\begin{bmatrix} f_x \\ f_y \end{bmatrix}$$

(68)

The vector normal to the edge is $n = (n_x, n_y)$ and the vector tangent to n is $t = (-n_y, n_x)$, thus Eq. (68) is rewritten as:

$$\begin{bmatrix} \nabla \psi_x.t \\ \nabla \psi_y.t \end{bmatrix}=\begin{bmatrix} f_x \\ f_y \end{bmatrix}$$

(69)

$$\psi_x(s)=\int_{s_0}^{s} f_x ds \quad on\ \Gamma_N$$

$$\psi_y(s)=\int_{s_0}^{s} f_y ds \quad on\ \Gamma_N$$

On Dirichlet boundaries, no boundary conditions are specified for ψ_x and ψ_y. The boundary conditions for third variable, Lagrange multiplier λ, on the whole boundary is $\lambda = 0$. The two sets of PDEs in Eqs. (66) and (67) along with the boundary conditions of Eq. (69) are solved using finite element method with 6 nodded triangular elements to determine the optimized load functions (i.e. ψ_x, and ψ_y) that lead to minimized deviatoric and stress norm objective functions. Next, the optimal density distribution for rank-two laminates in terms of principle stresses is as follows (Allaire, 2001; Jog et al., 1994):

$$\rho = \min \left(1, \frac{|\sigma_1| + |\sigma_2|}{\sqrt{2El}}\right) \tag{70}$$

The principles stresses are derived from optimal stress tensor σ using the optimized load paths, ψ_x and ψ_y and Eq. (59. Lagrange multiplier l is for enforcing the volume constraint (Allaire, 2001; Jog et al., 1994) . If l is very large the density distribution will represent the Michell structure (Allaire et al., 1993).

The developed optimization formulation based on load paths lead to two important observations. The first one is as follows:

If the boundary conditions are solely represented in terms of traction, the minimization of squared von Mises stress will be equivalent of minimization of squared norm of stress.

Squared von Mises stress can be written in terms of squared stiffness based objective function, and determinant of stress tensor:

$$\mathcal{J}_4 = \int_\Omega \sigma_v^2 d\Omega = \int_\Omega (|\sigma_1| + |\sigma_2|)^2 - 2|\sigma_1\sigma_2| - \sigma_1\sigma_2 \, d\Omega \tag{71}$$

The first integrand in the right side of Eq. (71) can be written as norm of stress and its determinant:

$$(|\sigma_1| + |\sigma_2|)^2 = |\sigma|^2 + 2\,|det(\sigma)\,| \tag{72}$$

Considering the load path functions ψ_x and ψ_y, the determinant of stress tensor is as follows:

$$det(\sigma) = -\frac{\partial \psi_y}{\partial x}\frac{\partial \psi_x}{\partial y} + \frac{\partial \psi_x}{\partial x}\frac{\partial \psi_y}{\partial y} = -\left(\frac{\partial \psi_y}{\partial x}\vec{\imath} + \frac{\partial \psi_y}{\partial y}\vec{\jmath}\right).\left(\frac{\partial \psi_x}{\partial y}\vec{\imath} - \frac{\partial \psi_x}{\partial x}\vec{\jmath}\right) \tag{73}$$

$$= -\left(\nabla\times(\psi_x\vec{k})\right).(\nabla\psi_y)$$

Therefore, the integral of $det(\sigma)$ is written as

$$\int_\Omega det(\sigma)\,d\Omega = \int_\Omega -\left(\nabla\times(\psi_x\vec{k})\right).(\nabla\psi_y)d\Omega \tag{74}$$

$$= \int_\Omega \nabla.\left(\psi_x\vec{k}\times(-\nabla\psi_y)\right)d\Omega + \int_\Omega \psi_x\vec{k}.(\nabla\times(-\nabla\psi_y)d\Omega$$

The second term in the right side of Eq. (74) is zero, and the first term is written as:

$$\int_\Omega \nabla.(\psi_x\vec{k}\times - \nabla\psi_y)d\Omega = \int_\Gamma \left(\psi_x\vec{k}\times(-\nabla\psi_y)\right).\vec{n}\,d\Gamma = \int_\Gamma \psi_x\frac{\partial\psi_y}{\partial t}\,d\Gamma \tag{75}$$

The last integral is on the boundary and it is dependent on ψ_x and ψ_y on the boundary. When the traction boundary conditions are applied solely, the load functions ψ_x and ψ_y are known on the boundary according to Eq.(69). Hence, the load functions are not changing during the optimization because the traction does not change. For this reason, the term $\int_\Omega det(\sigma)\,d\Omega$ is not changing during the optimization, and it is called null Lagrangian. Therefore, $\mathcal{J}_4$ only depends on the norm of stress tensor and it is equivalent of squared stress tensor norm minimization because all the terms on the right

side of Eq. (71) can be written as $det(\sigma)$, i.e. $det(\sigma) = \sigma_1\sigma_2$. This conclusion is along with those stated by (Allaire et al., 1993).

The second observation is : The difference between optimized load paths resulted from norm of stress, and compliance minimization can be explained using Coarea formula (Strang et al., 1983). Under certain conditions the optimized load paths for norm of stress are shorter than the ones for minimum compliance, and vice versa. Norm of stress minimization is,

$$\min_{\sigma} \mathcal{J}_1 = \int_{\Omega} |\sigma| d\Omega \tag{76}$$

Replacing the stress tensor components (σ_{ij}) by load path functions (ψ_x, and ψ_y) using Eq. (59 , and algebraic manipulations yields to,

$$\min_{\psi_x,\psi_y} \mathcal{J}_1 = \min_{\psi_x,\psi_y} \int_{\Omega} \sqrt{|\nabla\psi_x|^2 + |\nabla\psi_y|^2} \, d\Omega \tag{77}$$

$$= \min_{\psi_x,\psi_y} \int_{\Omega} \sqrt{\left(\frac{\partial(\psi_x + \psi_y)}{\partial x}\right)^2 + \left(\frac{\partial(\psi_x + \psi_y)}{\partial y}\right)^2 - 2(\frac{\partial\psi_x}{\partial x}\frac{\partial\psi_y}{\partial x} + \frac{\partial\psi_x}{\partial y}\frac{\partial\psi_y}{\partial y})} d\Omega$$

If the last term of the above equation is negligible in some parts of Ω,

$$\min_{\psi_x,\psi_y} \mathcal{J}_1 = \min_{\psi_x,\psi_y} \int_{\Omega} |\nabla(\psi_x + \psi_y)| d\Omega \tag{78}$$

Using the Coarea formula, the norm of gradient of any function ($\psi = \psi_x + \psi_y$) on domain Ω is equal to the sum of the lengths of its level sets $\gamma(\psi)$ as follows:

$$\min_{\psi_x,\psi_y} \mathcal{J}_1 = \min_{\psi_x,\psi_y} \int_{\Omega} |\nabla(\psi_x + \psi_y)| d\Omega = \min_{\psi_x,\psi_y} \int_{-\infty}^{+\infty} \gamma(\psi_x + \psi_y) dt \tag{79}$$

To minimize $\mathcal{J}_1$, according to Eq.(79) the lengths of the level sets of their sum ($\psi = \psi_x + \psi_y$) must be minimized. This observation is dependent on the magnitude of

$\frac{\partial \psi_x}{\partial x}\frac{\partial \psi_y}{\partial x} + \frac{\partial \psi_x}{\partial y}\frac{\partial \psi_y}{\partial y}$ which is equal to $\sigma_{xy}(\sigma_x + \sigma_y)$. If σ_{xy} is small, or $\sigma_x = -\sigma_y$ this term

is negligible, and the optimized load paths for norm of stress become shorter that the ones

for compliance minimization. A similar argument can be made for the opposite case,

when the compliance load paths become shorter if the term $\sigma_{xy}(\sigma_x + \sigma_y) + \det(\sigma)$

becomes negligible.

4.2   Microstructure Construction

4.2.1   Principal Load Paths

It has been proven that the optimal microstructure is aligned with the principal

stress direction in (Pedersen, 1987, 1989). To construct the optimal microstructure, the

load functions, with their curls are in the direction of the principal vectors should be

found. Principal load paths are level sets of load path functions that are tangent to the

principal stress directions ($\vec{e} = e^x i + e^y j$) in the optimal design.

$$-\frac{\partial \psi_1}{\partial x} = e_1^y, \qquad \frac{\partial \psi_1}{\partial y} = e_1^x \tag{80}$$

$$-\frac{\partial \psi_2}{\partial x} = e_2^y, \qquad \frac{\partial \psi_2}{\partial y} = e_2^x \tag{81}$$

Since the gradient of ψ_1 and ψ_2 are equal to a vector field in Eqs. (80) and (81), it

means the vector fields are curl free according to Helmholtz theorem (Larson et al., 2013,

p. 347). However, the principal direction vectors are not necessarily curl free. In order to

find the curl free vector field, the principle directions are multiplied by e^r in Eq. (82)

(Allaire et al., 2018).

$$-\frac{\partial \psi_1}{\partial x} = e_1^y e^r \qquad\qquad -\frac{\partial \psi_2}{\partial x} = e_2^y e^r \qquad (82)$$

$$\frac{\partial \psi_1}{\partial y} = e_1^x e^r \qquad\qquad \frac{\partial \psi_2}{\partial y} = e_2^x e^r$$

where r can be found by setting the curl of the principal vector field to zero as follows:

$$\nabla \times e^r \left(-e_2^y i + e_2^x j\right) = 0 \qquad\qquad \nabla \times e^r \left(- e_1^y i + e_1^x j\right) = 0 \qquad (83)$$

After some algebraic manipulation, Eq. (83) will lead to Eq.(84),

$$\nabla e_2 + \nabla r. e_2 = 0 \qquad\qquad \nabla e_1 + \nabla r. e_1 = 0 \qquad (84)$$

where the projection of ∇r on e_i , $\nabla r. e_i$ is determined to be $-\nabla e_i$. Hence, ∇r can be

written as sum of its projections on e_1, and e_2 as follows:

$$\nabla r = (-\nabla. e_1)e_1 + (-\nabla. e_2)e_2 \qquad (85)$$

To find r we minimize the following Lagrangian,

$$\mathcal{L} = \int_\Omega |\nabla r + (\nabla e_1)e_1 + (\nabla e_2)e_2|^2 \, d\Omega \qquad (86)$$

Using Euler-Lagrange optimality criteria leads to the following equation that is solved by

FEM.

$$\nabla^2 r = \nabla. ((-\nabla e_1)e_1 + (-\nabla e_2)e_2) \qquad (87)$$

The following Lagrangian $\mathcal{L}_i$ is then minimized to obtain ψ_1, and ψ_2.

$$\mathcal{L}_i = \int_\Omega \left(-\frac{\partial \psi_i}{\partial x} - e_i^y e^r\right)^2 + \left(\frac{\partial \psi_i}{\partial y} - e_i^x e^r\right)^2 d\Omega \qquad (88)$$

Lagrangian $\mathcal{L}_i$ is minimized using Euler-Lagrange optimality criteria leading to

Eq.(89).

$$\nabla^2 \psi_i = \nabla \times (e^r e_i) \qquad (89)$$

The second issue with the principal stress vector fields is of it is not coherent and

the direction can change by π which leads to singularities in the vector field. To address

this issue, the inconsistency in the flow of cell propagation is first captured to modify the vector field. The edge labeling which is the dot product of the vectors of two vertices identifies the irregularities in the local element (Hotz et al., 2010); if the product of all dot products between pairs of vectors is non-positive, then the element contains degenerate points; otherwise, if some dot products are negative, there is a π difference in orientation.

The edge labelings $l(e_i)$, $l(e_j)$, $l(e_k)$ are found for a triangular finite element mesh with vertices i, j, k and edges e_i e_j, and e_k (see Figure 4.2) using the following:

$$l(e_i) = \begin{cases} 0 & if \quad v_j.v_k = 0 \\ -1 & if \quad v_j.v_k < 0 \\ 1 & if \quad v_j.v_k > 0 \end{cases} \tag{90}$$
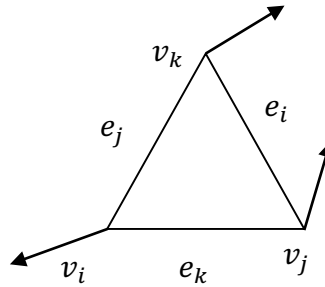
Figure 4.2 The principal vector directions and edge labeling on a finite element mesh

The next step is to interpolate the new coherent vector field after rotating some vectors by π radians. The rotation of the vectors is ensured by multiplying the vectors to the corresponding edge labels. The new vector field at any point (η, ξ) can be found as follows:

$$v_{new}(\eta, \xi) = N_i(\eta, \xi)v_i + N_j(\eta, \xi)l(e_k) + N_k(\eta, \xi)l(e_j) \tag{91}$$

In Eq. (91), N_i, N_j, N_k are linear finite element shape functions for 3 nodded triangular elements, and $l(e_i)$, $l(e_j)$, $l(e_k)$ are edge labeling.

4.2.2 Microstructure Dimensions

While the density distribution is represented for rank-two laminates in Eq. (70), the fabrication of such microstructure using the existing 3D printing technology is complicated because of different length scales. Therefore, the rank-two laminates are replaced with square cells with rectangular holes (see Figure 4.3). Considering a unit cell with unit thickness with a hole volume of $a_1 a_2$, the density of the solid area is:

$$1 - a_1 a_2 = \rho \tag{92}$$

If the cell is aligned with the principal stress direction, then following equation can be derived,

$$\frac{|\sigma_1|}{(1 - a_2)} = \frac{|\sigma_2|}{(1 - a_1)} \tag{93}$$

and a_1 and a_2 are determined by solving Eqs. (92) and (93) simultaneously (Pantz et al., 2008). To construct the cell with rectangular hole $a_1 a_2$ as seen in Figure 4.3(a), the following set is used.

$$Y = \{(x_1, x_2) \in [0,1]^2 \mid \cos(2\pi x_1) > \cos(\pi(1 - a_1)) \ \cup \ \cos(2\pi x_2) \tag{94}$$
$$> \cos(\pi(1 - a_2))\}$$

In set Y, the coordinates of any points in a unit square domain (x_1, x_2) are changing from zero to one, and the cosine functions $\cos(2\pi x_i)$ are constructing one period of a cosine function as $2\pi x_i$ changes from zero to 2π. Parts of the cosine wave that are more than threshold $\cos(\pi(1 - a_i))$ are solid parts of the structure, and the rest are void. The threshold $\cos(\pi(1 - a_i))$ is varying between -1 to 1 as a_i is changing from zero to one, and creates different periodic square based on the value of a_i.

The periodic unit square cell in set Y, Eq.(94) is extended to a host of periodic cells creating a lattice structure on domain D with periodicity ϵ using set Ω_0 as in Eq. (95).

$$\Omega_0 = \{(x_1, x_2) \in D \mid \cos\left(\frac{2\pi x_1}{\epsilon}\right) > \cos\left(\pi(1 - a_1)\right) \ \cup \ \cos\left(\frac{2\pi x_2}{\epsilon}\right) \tag{95}$$

$$> \cos\left(\pi(1 - a_2)\right)\}$$

Since a_1, and a_2 vary with cell locations, the holes in the periodic squares have different dimensions. Set Ω_0 is creating a lattice structure in direction of $x_1 x_2$ coordinate system. This set can be extended to a lattice structure on curvilinear directions $\psi_1 \psi_2$ that are the level sets of the principal load functions found using Eq.(89), as seen in Eq.(96). In set Ω_M the cosine waves are constructed along ψ_1, and ψ_2 with periodicity ϵ and the threshold is based on the size of the hole a_1 and a_2.

$$\Omega_M = \{(x_1, x_2) \in D \mid \cos\left(\frac{2\pi\psi_1(x_1, x_2)}{\epsilon}\right) \tag{96}$$

$$> \cos\left(\pi(1 - a_1)\right) \ \cup \ \cos\left(\frac{2\pi\psi_2(x_1, x_2)}{\epsilon}\right)$$

$$> \cos\left(\pi(1 - a_2)\right)\}$$

(a)   (b)
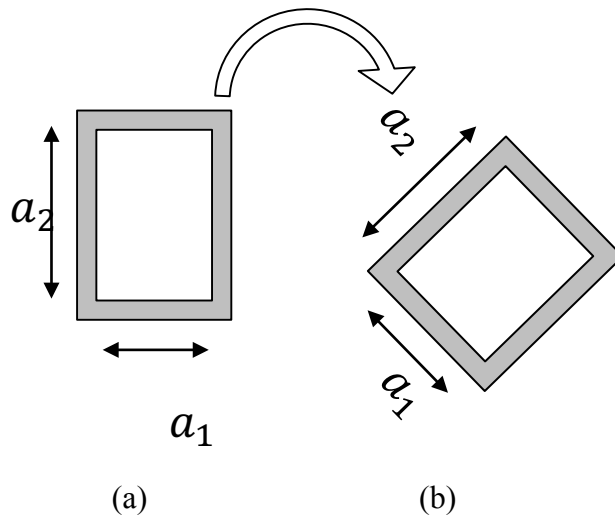
Figure 4.3 The periodic microstructure, (a) before mapping and (b) after mapping to the principal directions

4.2.3   Post-Processing

Some parts of optimal structures are not manufacturable due to the existence of thin

bars, and small members. These members can be removed or changed to manufacturable

members by post processing. The post processing used here has been used previously

(Allaire et al., 2018). A Heaviside function approach can also be utilized in the post-

processing (Groen et al., 2018). The minimum width is set to h_{min}. The size of the

original unit cells is ϵ. After the projection using the principal vector field, the size of

each cell becomes $h_c = \epsilon e^{-r}$. Hence the size of bars at each cell is $(1 - a_1)h_c$ and

$(1 - a_2)h_c$. The geometry is modified based on how small the cells are, if the cells are

too small ($h_c < 2h_{min}$), they should be either void or solid: if $a_i < 0.5$ then $a_i = 0$ is

assigned, and if $a_i > 0.5$ then $a_i = 1$ is assigned. Whereas, if the cells are large enough,

$h_c > 2h_{min}$, only the bars that are smaller than $\frac{h_{min}}{2h_c}$ are removed, and the bars with their

widths larger than $1 - \frac{h_{min}}{2h_c}$ are projected to 1. Figure 4.4 shows all the post-processing

procedure for two different regimes based on h_c, and $2h_{min}$.
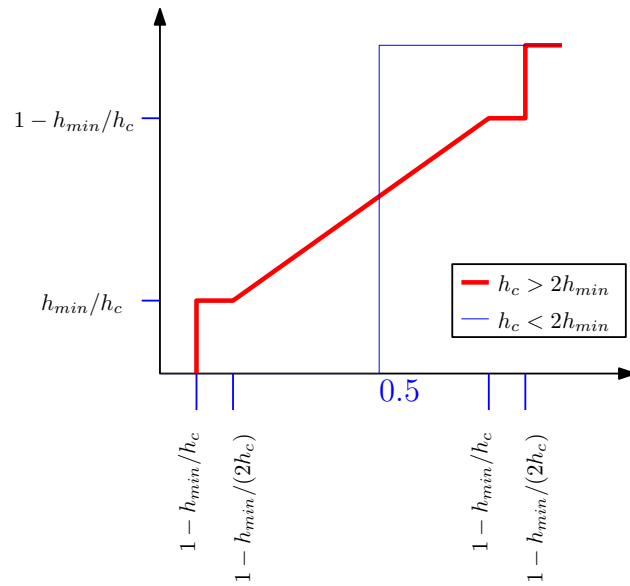
Figure 4.4 Post-processing of the optimal design (Allaire et al., 2018)

4.3   Numerical Examples

4.3.1   Square Plate Under Axial Load

The square plate under axial load (Figure 4.5) is selected to test the observation of

Eqs. (71)-(75). According to Eq. (75) the determinant of stress tensor is not changing

during the optimization when only traction boundary conditions are applied. Hence, the

optimizing variables (i.e. ψ_x , and ψ_y) of objective function $\mathcal{J}_4$ in Eq. (71) are equivalent

to ones for square of norm of stress when only traction boundary conditions are applied.

The optimized load paths are determined for $\int_\Omega (|\sigma_1| + |\sigma_2|)^2 d\Omega$ as shown in Figure 4.6

(a), and (b). The minimization of $\int_\Omega |\sigma|^2 d\Omega$ is carried out and optimized load paths are

plotted in Figure 4.6 (c), and (d). As can be seen in Figure 4.6, the optimized load paths

are identical for both cases.
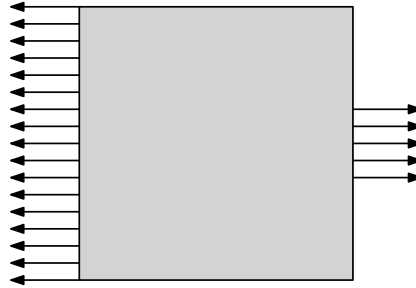
Figure 4.5 Axial tractions on a square plate

ψ_x

ψ_y

(a)

(b)

ψ_x

ψ_y

(c)

(d)
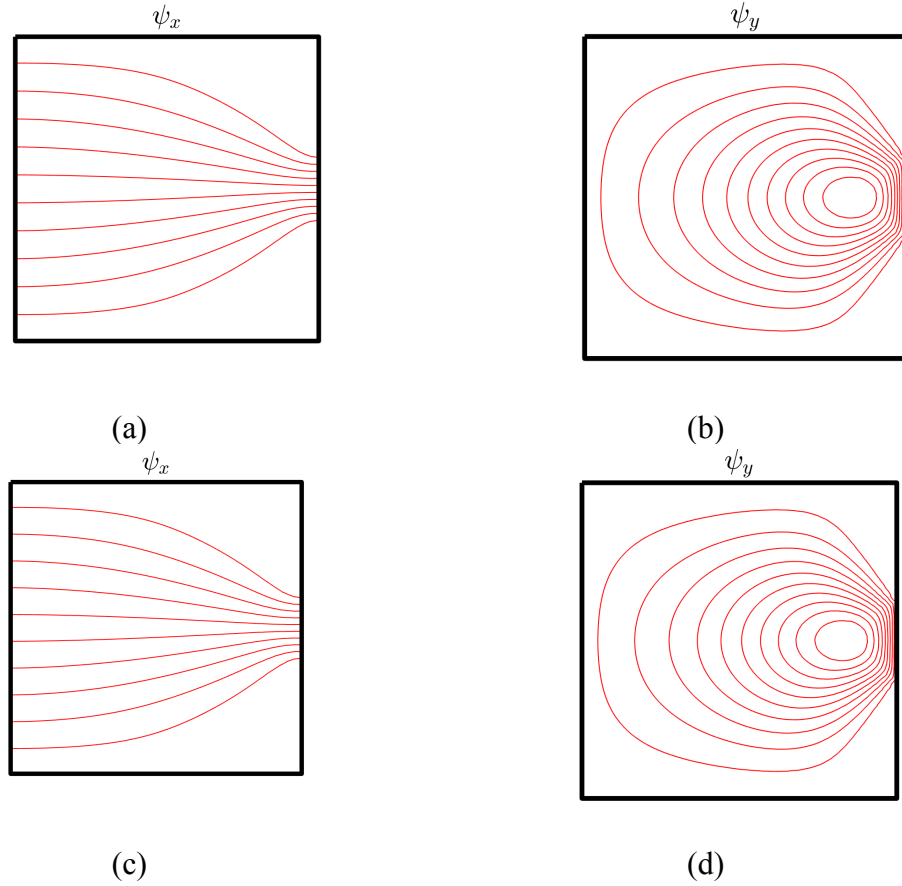
Figure 4.6 Optimized load paths for $\int_{\Omega}(|\sigma_1| + |\sigma_2|)^2 d\Omega$ minimization, (a) optimized load paths ψ_x, (b) optimized load path ψ_y. Optimized load paths for $\int_{\Omega}|\sigma|^2 d\Omega$ minimization, (c) optimized load path ψ_x, (d) optimized load paths ψ_y.

4.3.2   Cantilever Beam with Load At the Center

In this example, the optimized load paths are found by minimizing the compliance, and norm of stress subjected to the equilibrium for a rectangle cantilever beam with length 2, and unit height and thickness. The non-linear system of PDEs that are derived by Euler-Lagrange optimality criteria using Eqs. (66), and (67) are solved using finite element method. Second order polynomial shape function is used on 6 nodded triangular structured mesh. In this model, 13,000 nodes and 6,400 elements are used.

The unit load $f_y = -1$ applied on the right edge, as shown in in Figure 4.7, determines the boundary conditions on ψ_y using Eq.(69). The traction free surfaces on

top, bottom, and right edge lead to constant ψ_x, and ψ_y using Eq. (69). Since there are no

traction boundary conditions on the clamped edge, no boundary conditions are specified

for ψ_x, and ψ_y. Lagrange multiplier λ is zero on the whole boundary. Gauss-Newton

method takes 20 iterations to solve the problem with quadratic convergence.

The initial guess used to solve the non-linear PDEs (Figure 4.8 (a), and (b)) are

determined by finding the load path in the fully solid design (Figure 4.7) using authors'

load function method (Tamijani et al., 2017; Tamijani et al., 2018). However, due to the

convexity of the problem, any initial load functions that satisfy the boundary conditions

can lead to the global optimal (Svanberg, 1981). After optimization, as seen in Figure 4.8

(c) and (d), the optimized load functions ψ_x and ψ_y become flat (i.e. $\nabla\psi_x = 0$, and

$\nabla\psi_y = 0$) in areas that the optimal stresses are close to zero.

In Table 4.1, the value of each objective function at the optimal for each

minimization, and its initial value are shown. As expected for norm of stress

minimization, the value of compliance is slightly higher than its value in compliance

minimization. This is the case for compliance minimization as well. However, both

values are significantly lower than the initial values. In Figure 4.9, the difference between

the optimized load paths for compliance and norm of stress is evident. According to the

second observation in Eqs. (76)-(79), the length of the norm of stress optimized load

paths are reduced in regions at the center of domain Ω that $\sigma_{xy}(\sigma_x + \sigma_y)$ becomes

negligible.

To construct the optimal microstructure, the optimal stresses are determined from

optimized load paths using Eq. (59. The derivative of ψ_x, and ψ_y are smoothed with a

radius of two element length using the weighted average filtering method (Guest et al.,

2004). Principal stresses are also found from stresses, and Eq. (70) is used to determine the homogenized density as seen in Figure 4.10(a). Module of elasticity is $E = 1$, and Lagrange multiplier for volume fraction is $l = 20$. As can be seen in Figure 4.10(a), the density is high at the top and bottom of domain Ω because of the high stress values, and gradients of load functions. Whereas, the low-density areas are located at flat load function areas at the center and corners on the right edge seen in Figure 4.8 (c-f).

The dimensions of microstructure $1 - a_1$, and $1 - a_2$ are determined by solving Eqs. (92), and (93) simultaneously as seen in Figure 4.10 (b), and (c). Each of them are representing the solid parts of a periodic square that is aligned with its corresponding principal stress direction. The higher σ_i, the higher $1 - a_i$. The areas with high $1 - a_i$ in one direction, and low in other direction resemble a solid square cell, while the gray areas resemble the periodic microstructure with holes $a_1 a_2$.

The next ingredient for constructing the microstructure is the optimal orientation (Figure 4.11 (a), and (b)) which is proven to be the direction of principal stresses (Pedersen, 1989). As seen in Figure 4.11 (a), and (b), the principal stress directions can rotate by π and create a singular vector field. To solve this problem an interpolation using Eq. (91) is used which removes the singularity and creates a coherent vector field seen in Figure 4.11 (c), and (d). The coherency of the vector field is required to successfully establish smooth principal load paths (ψ_1, and ψ_2) and construct the microstructure.

To make the principal stress vectors curl free, a dilation field is calculated using Eq.(85) to ensure solution of Eq. (89) are tangent to the vector field $e^r e_i$. Otherwise the solution of Eq. (89) for ψ_1, and ψ_2 would have a larger error, and would not represent the vector field $e^r e_1$, and $e^r e_2$. Principal load functions (ψ_1, and ψ_2) are calculated using

finite element method on a finer mesh with 25400 elements, and 64000 nodes using Eq. (89) as seen in Figure 4.12.

Level sets of ψ_1, and ψ_2 are principal load paths that create the Michell like lattice as shown in Figure 4.13. Using load functions ψ_i, microstructure dimensions a_i, and Eq. (96) the optimized structure is determined as seen in Figure 4.14 with 500,000 nodes and 250,000 elements to achieve a higher resolution. Post processing of the structure to remove the non-manufacturable features is carried out by removing the features smaller than $h_{min} = .03\epsilon$ for all examples in Figure 4.14.

As expected the microstructure is aligned with principal load path directions seen in Figure 4.13, According to Eq. (96), the regions with no holes $a_i = 0$ will make the $cos\,(\pi(1 - a_i))$ to become -1, and $cos\left(\frac{2\pi\psi_i(x_1,x_2)}{\epsilon}\right)$ becomes always larger than $cos\,(\pi(1 - a_i))$ which makes Ω_M solid. Different periodicity or cell size ϵ are used in Figure 4.14. Fine microstructure seen in Figure 4.14(a) has a better stiffness than a coarse one seen Figure 4.14(b).

Table 4.1 Objective function values at optimal for each optimization

	$\mathcal{J}_1 = \int_\Omega |\sigma|d\Omega$	$\mathcal{J}_2 = \int_\Omega (|\sigma_1^D| + |\sigma_2^D|)d\Omega$
Values of $\mathcal{J}_1$, and $\mathcal{J}_2$ after $\min_\sigma \mathcal{J}_1 = \int_\Omega |\sigma|d\Omega$	6.52	7.36
Values of $\mathcal{J}_1$, and $\mathcal{J}_2$ after $\min_\sigma \mathcal{J}_2 = \int_\Omega (|\sigma_1^D| + |\sigma_2^D|)d\Omega$	6.63	7.17
Initial values of $\mathcal{J}_1$, and $\mathcal{J}_2$	7.41	8.02

Figure 4.7 Cantilever beam with point load at the center of right edge

Figure 4.8 Initial load functions at the beginning of optimization, (a) load function in x direction, ψ_{x1}, and (b) load function in y direction, ψ_{y1}, Optimal load functions after optimization, (c) optimal load path ψ_x, (d) optimal load path ψ_y. Optimal load functions after stress minimization, (e) optimal load function ψ_x, (f) optimal load function ψ_y

ψ_{x1}

ψ_{y1}

(a)

(b)

ψ_x

ψ_y

(c)

(d)

ψ_x

ψ_y

(e)

(f)

Figure 4.9 Initial load paths at the beginning of optimization, (a) load path in x direction, ψ_{x1}, and (b) load path in y direction, ψ_{y1}, Optimized load paths after compliance optimization, (c) optimized load path ψ_x, (d) optimized load path ψ_y. Optimized load paths after stress minimization, (e) optimized load path ψ_x, (f) optimized load path ψ_y

(a)

(b)

(c)
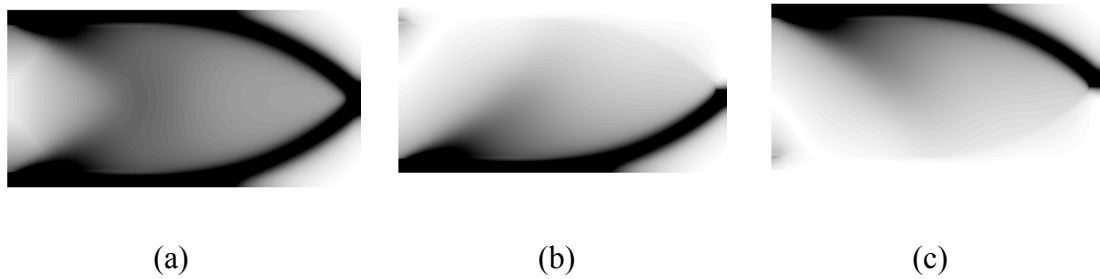
Figure 4.10 (a) The homogenized density for minimum compliance, Microstructure dimensions (b), $1 - a_1$, and (c), $1 - a_2$

(a)

(b)

(c)

(d)
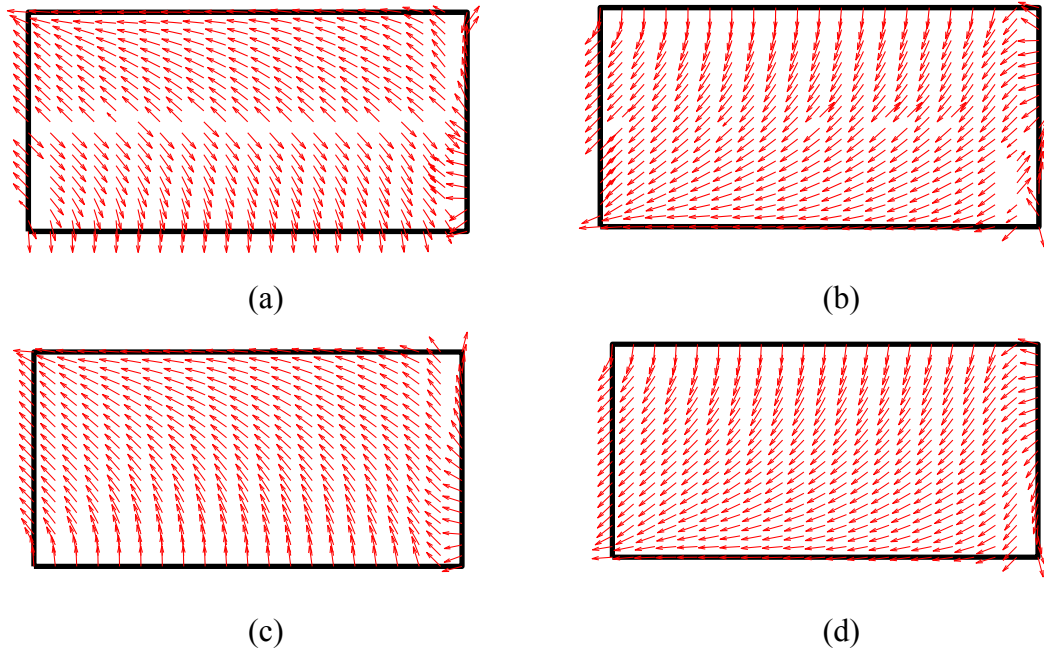
Figure 4.11 Principal stress direction before reconstructing to coherent vector field for compliance minimization (a) $\overrightarrow{e_1}$,and (b) $\overrightarrow{e_2}$ .Reconstructed principal stresses to coherent vector field (c) $\overrightarrow{e_1}$,and (d) $\overrightarrow{e_2}$.
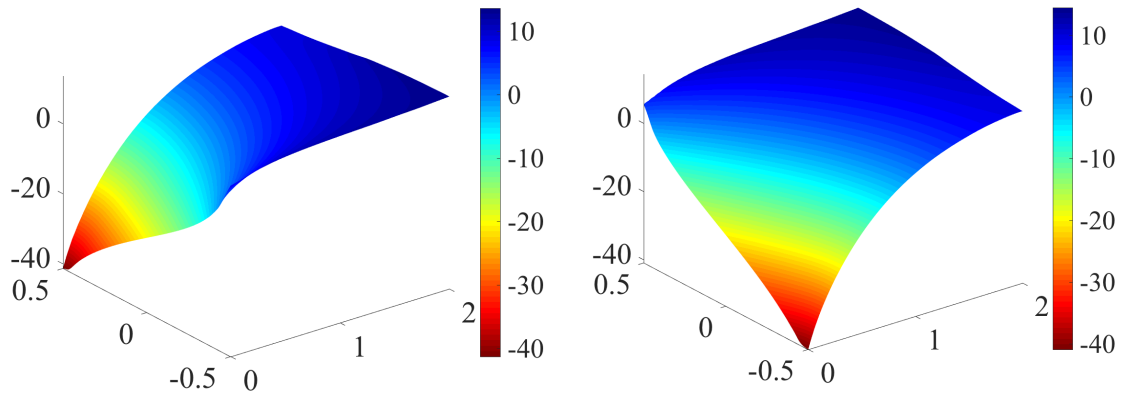
Figure 4.12 Principal Load functions ψ_1, and ψ_2 for minimum compliance
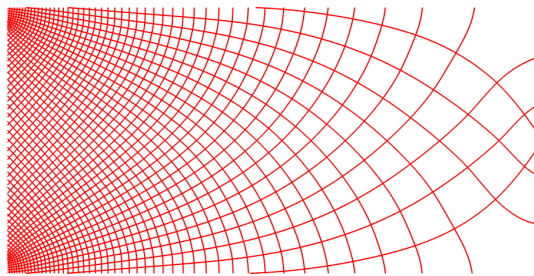
Figure 4.13 Union of principal load paths for minimum compliance $\psi_1 \cap \psi_2$.
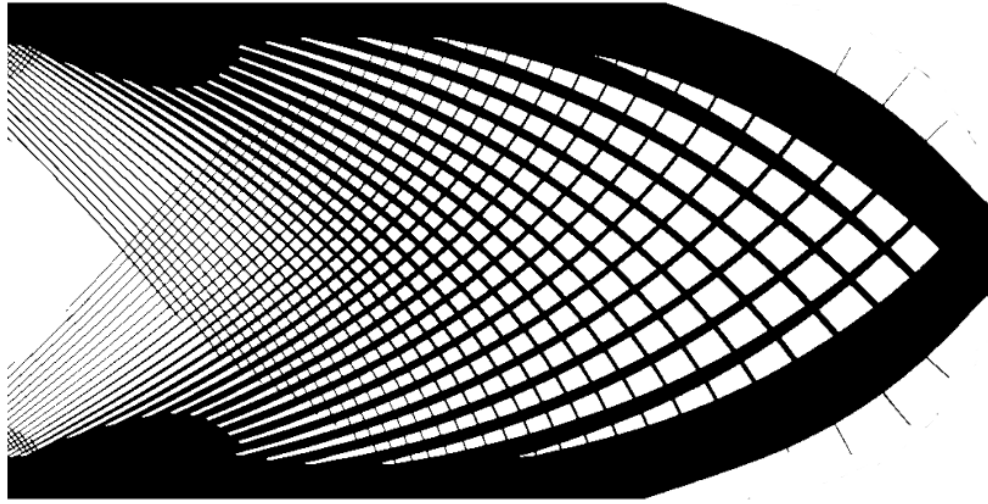
(a)
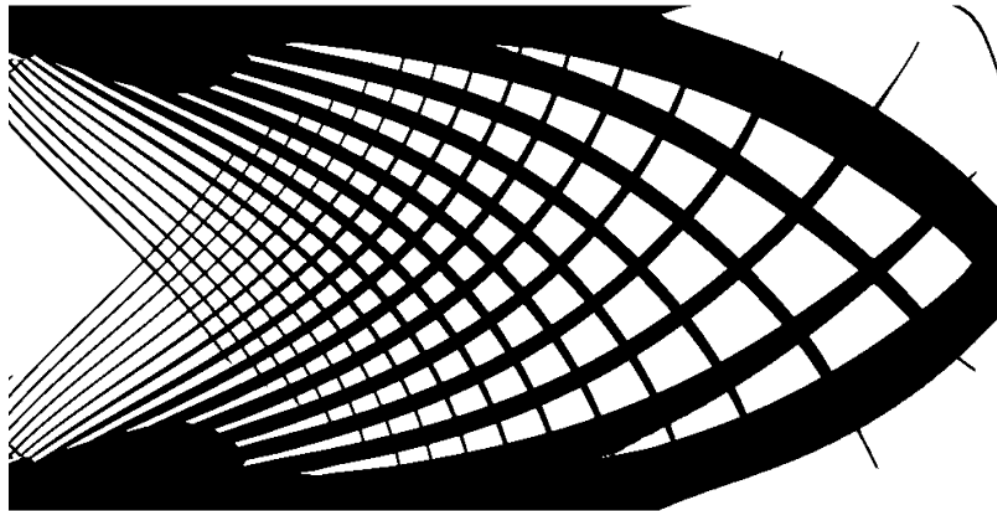
(b)

Figure 4.14 Optimized structures with two different periodicities (a), $\epsilon = 0.8$, and $\mathcal{J}_2 = 82.64$, (b) $\epsilon = 2.86$, and $\mathcal{J}_2 = 84.23$.

4.3.3 L-Shape Structure

Same as previous example, the optimized load paths are found by minimizing the compliance, and norm of stress subjected to the equilibrium for a L-beam with unit length, height, and thickness. In this model, 5000 nodes and 2500 elements are used to solve Euler-Lagrange optimality criteria Eqs. (66), and (67).

The unit load $f_y = -1$ applied on the center of right edge in Figure 4.15 determines the boundary conditions on ψ_y using Eq.(69). Gauss-Newton method takes 30 iterations to solve this problem with quadratic convergence. The initial guess used to solve the non-linear PDEs (Figure 4.16 (a), and (b)) are determined by finding the load path in the fully solid design. The optimized load paths for compliance are shown in Figure 4.16 (c), and (d).

To construct the optimal microstructure, module of elasticity is $E = 1$, and Lagrange multiplier for volume fraction $l = 70$ are selected. The optimized density and the dimensions of microstructure $1 - a_1$, and $1 - a_2$ are shown in Figure 4.17. Using load functions ψ_i and microstructure dimensions a_i, the optimized structure is determined as seen in Figure 4.18. Post processing of the structure to remove the non-manufacturable features is carried out by removing the features smaller than $h_{min} = .05\epsilon$ for all examples in Figure 4.18. Figure 4.19 shows the convergence of microstructures to the homogenized design for various sizes (ϵ). As expected, the higher stiffness is achieved for lower ϵ.
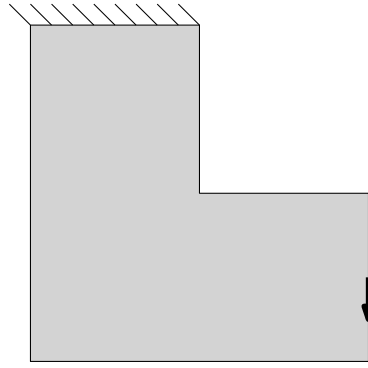
Figure 4.15 L-shaped beam with load on the right edge at center
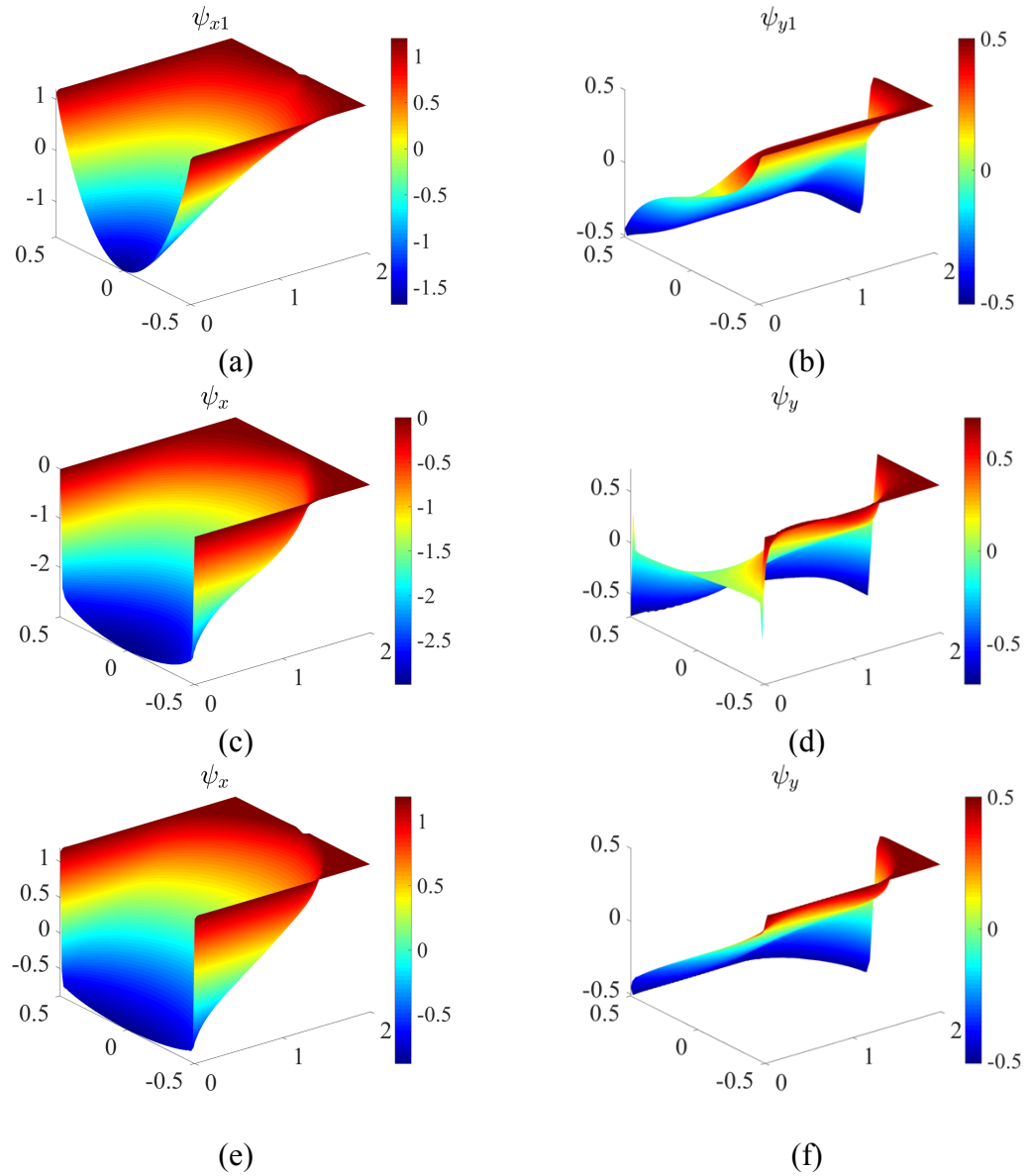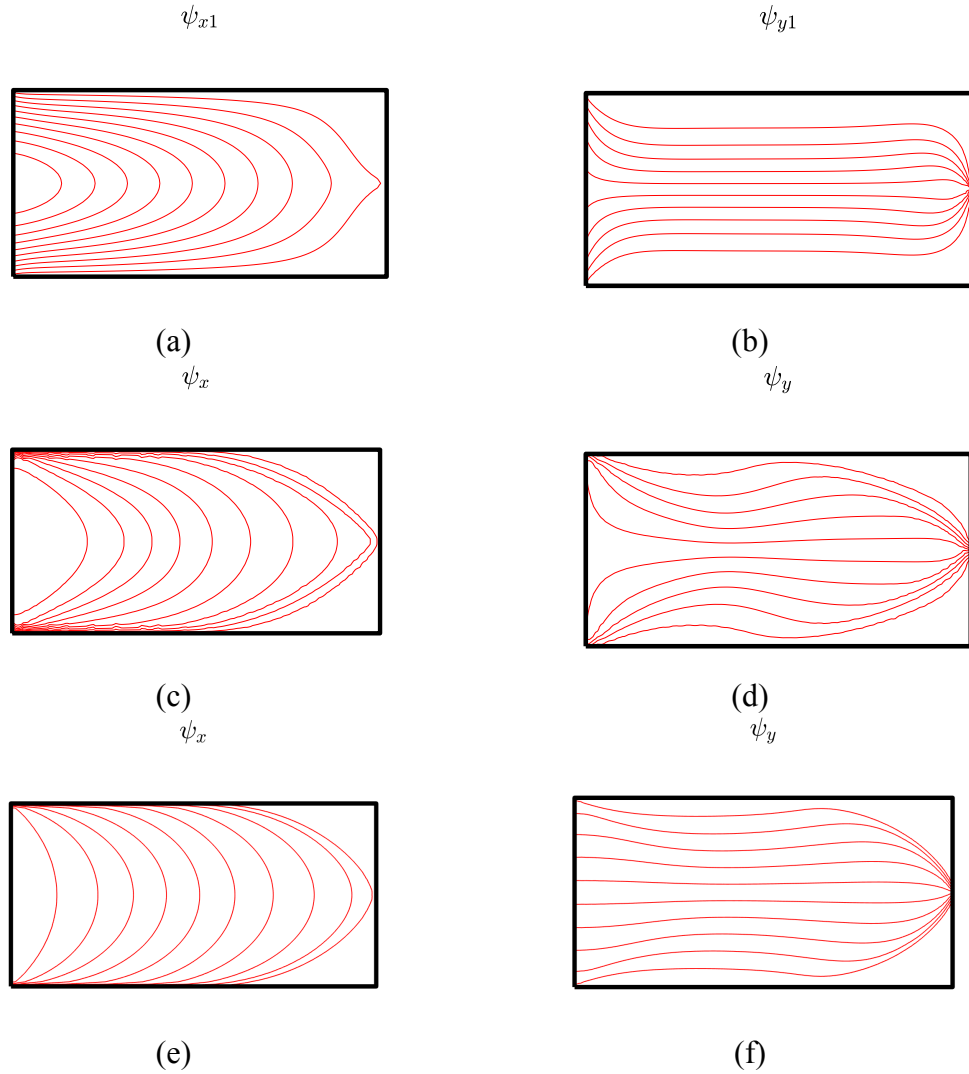

Figure 4.16 Initial load paths at the beginning of optimization, (a) load path in x direction, ψ_{x1}, and (b) load path in y direction, ψ_{y1}, Optimized load paths for compliance minimization, (c) optimized load path ψ_x.

(a) (b) (c)
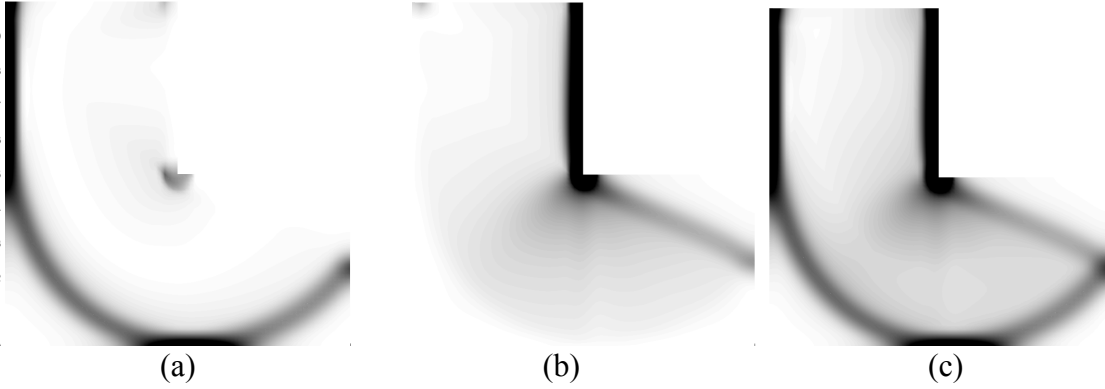
Figure 4.17 (a) The homogenized density for compliance minimization, Microstructure dimensions (b), $1 - a_1$, and (c), $1 - a_2$

(a) (b) (c)
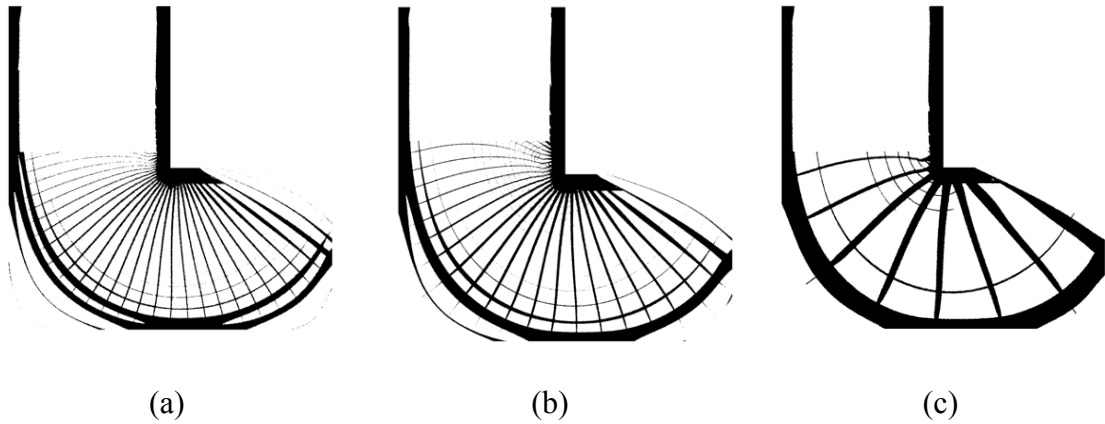
Figure 4.18 Optimized structures for minimum compliance with three different periodicity (a) ϵ=0.15, and $\mathcal{J}_2 = 200$, (b) ϵ=0.3, and $\mathcal{J}_2 = 255$, (c) ϵ=0.5, and $\mathcal{J}_2 = 330$
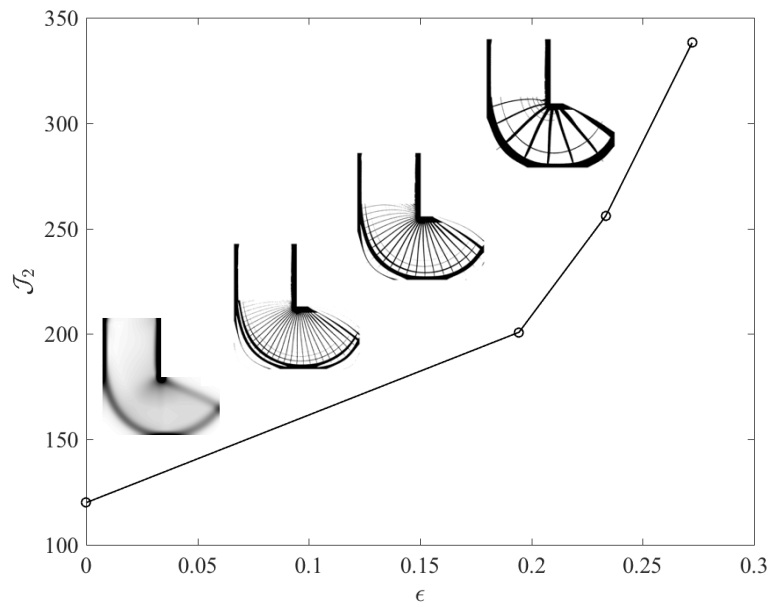
Figure 4.19 Change in objective function $\mathcal{J}_2$ based on size of microstructure ϵ

4.3.4 Power Pylon structure

A Power Pylon which consist of two horizontal, and vertical 2 by 1 rectangles is considered here. For Power Pylon, first the initial load path (ψ_{x1} , and ψ_{y1}) are found as seen in Figure 4.21 (a), and (b), then the compliance minimization is solved by using Euler-Lagrange optimality conditions to find the optimized load paths. Using the optimized load paths (ψ_x , and ψ_y) (Figure 4.21 (c), and (d)) the principal stresses and principal directions are calculated, and the coherent construction is carried and the principal load functions and load paths are calculated as seen in Figure 4.22. Next, the dimensions of the periodic microstructure are calculated using Eqs. (92), and (93), as seen in Figure 4.23, and the optimized structure is constructed (Figure 4.24).

An important numerical step in nonlinear optimization is the choice of parameter δ^2, which plays a significant role in convergence of Gauss-Newton method. Since the integrand of compliance objective function is the sum of absolutes of deviatoric principal stresses,

$$|\sigma_1^D| + |\sigma_2^D| = \sqrt{\left(\frac{\partial \psi_x}{\partial y} + \frac{\partial \psi_y}{\partial x}\right)^2 + 4\left(\frac{\partial \psi_y}{\partial y}\right)^2} \tag{97}$$

derivative of this term does not exist at zero. To fix this issue δ^2 is added under the square root,

$$\sqrt{\delta^2 + \left(\frac{\partial \psi_x}{\partial y} + \frac{\partial \psi_y}{\partial x}\right)^2 + 4\left(\frac{\partial \psi_y}{\partial y}\right)^2} \tag{98}$$

The value of δ^2 affects the convergence rate based on distance to the solution α ($e_i = x_i - \alpha$) in iteration i of any function $f(x)$ is as follows (Gerald, 2004):

$$e_{i+1} = \frac{1}{2}\frac{f''(\alpha)}{f'(\alpha)}e_i^2 \tag{99}$$

For $f(x) = \sqrt{\delta^2 + x}$, the convergence rate $\frac{1}{2}\frac{f''(x)}{f'(x)}$ would be $\frac{1}{\delta^2+x}$. Hence, the

higher δ^2 the lower e_{i+1} the distance to solution α, which means a faster convergence as

seen in Table 4.2. The value of δ^2 cannot be increased more than needed for timely

convergence because it will change the nature of the objective function as δ^2 becomes

much larger than additional terms in Eq. (98). Hence, to achieve the correct solution of

optimization problem $\mathcal{J}_2$ with a reasonable number of iterations, δ^2 must be kept as small

as possible. For example, in Table 4.2 choosing $\delta^2 = 0.04$ is a reasonable option.

Table 4.2 Rate of convergence based on δ

δ^2	Number of iterations	$\mathcal{J}_2$
0.01	78	60.83
0.04	42	60.75
0.09	28	60.70
0.16	27	60.67
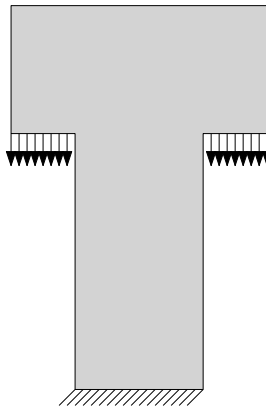
Figure 4.20 Power Pylon with applied loads and boundary conditions
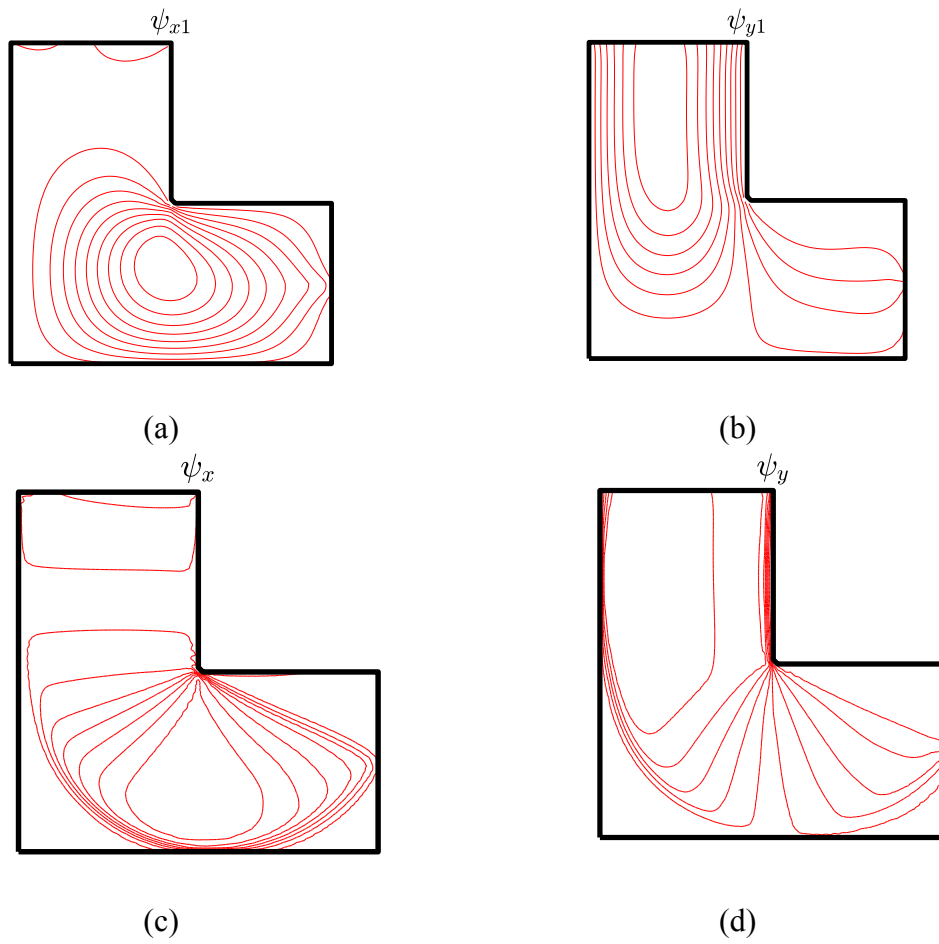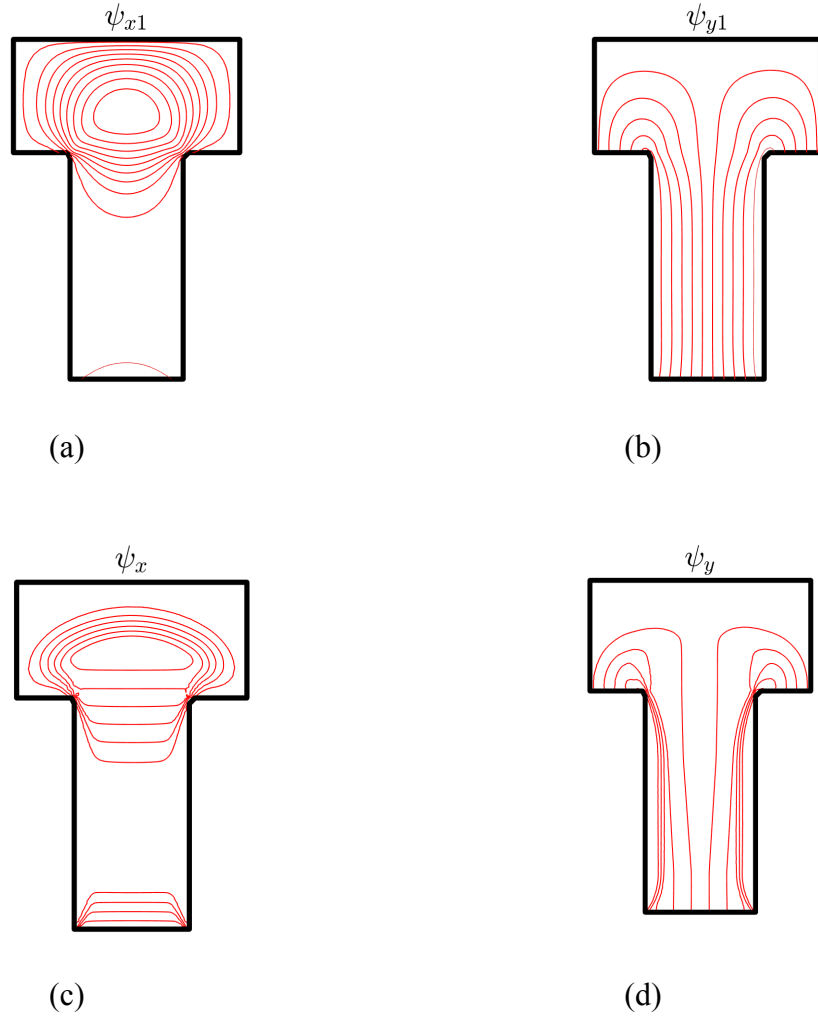
Figure 4.21 Initial load paths at the beginning of optimization, (a) load path in x direction, ψ_{x1}, and (b) load path in y direction, ψ_{y1}, Optimal load paths for compliance minimization, (c) optimal load path ψ_x, (d) optimal load path ψ_y.
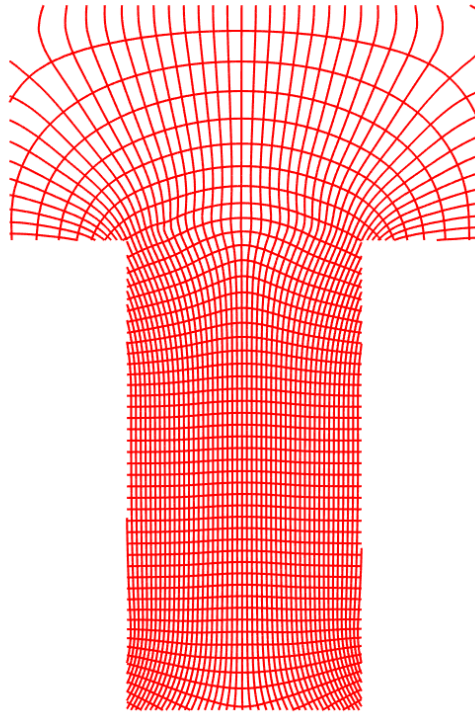
Figure 4.22 Union of principal load paths $\psi_1 \cap \psi_2$.

(b)   (c)
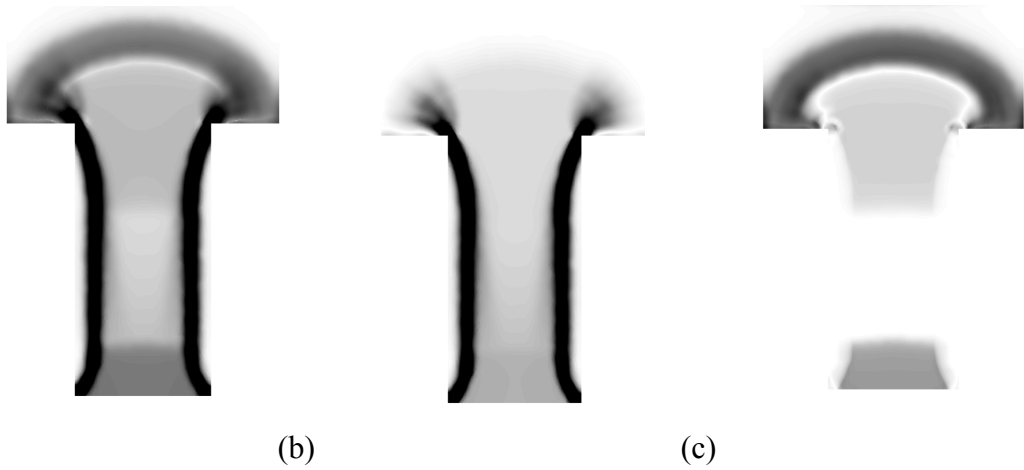
Figure 4.23 (a) The homogenized density, Microstructure dimensions (b), $1 - a_1$, and (c), $1 - a_2$
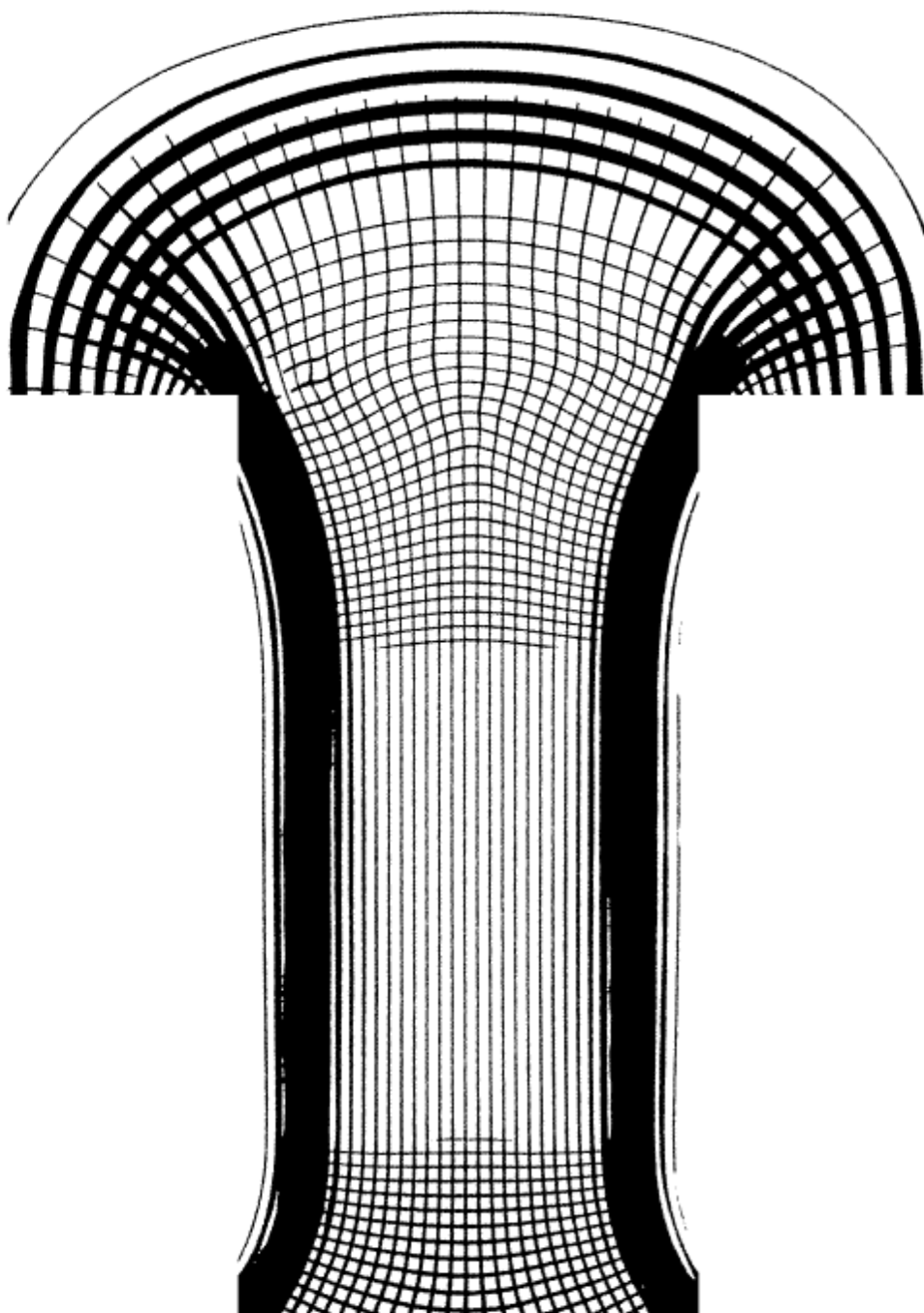
(a)
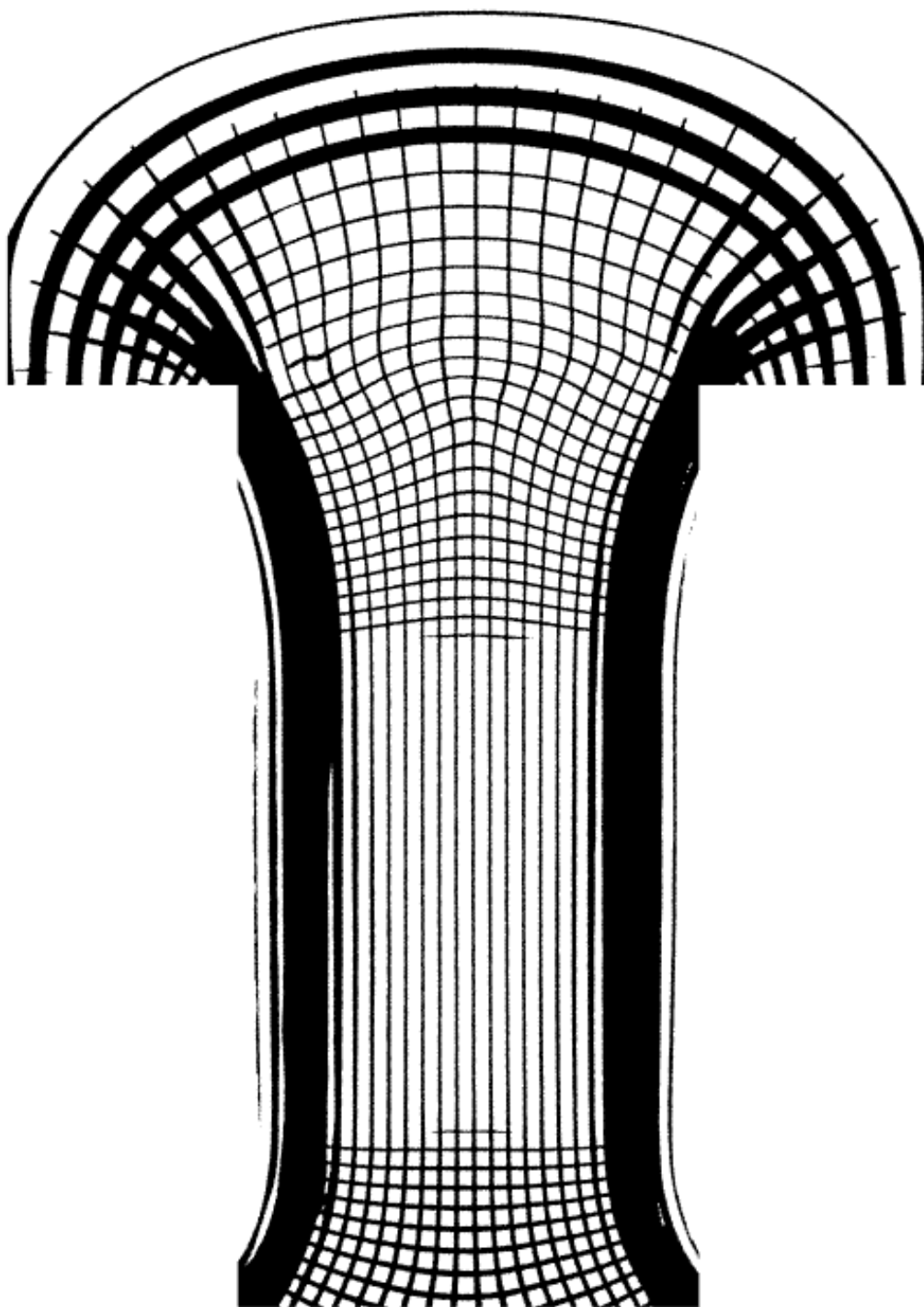
(b)
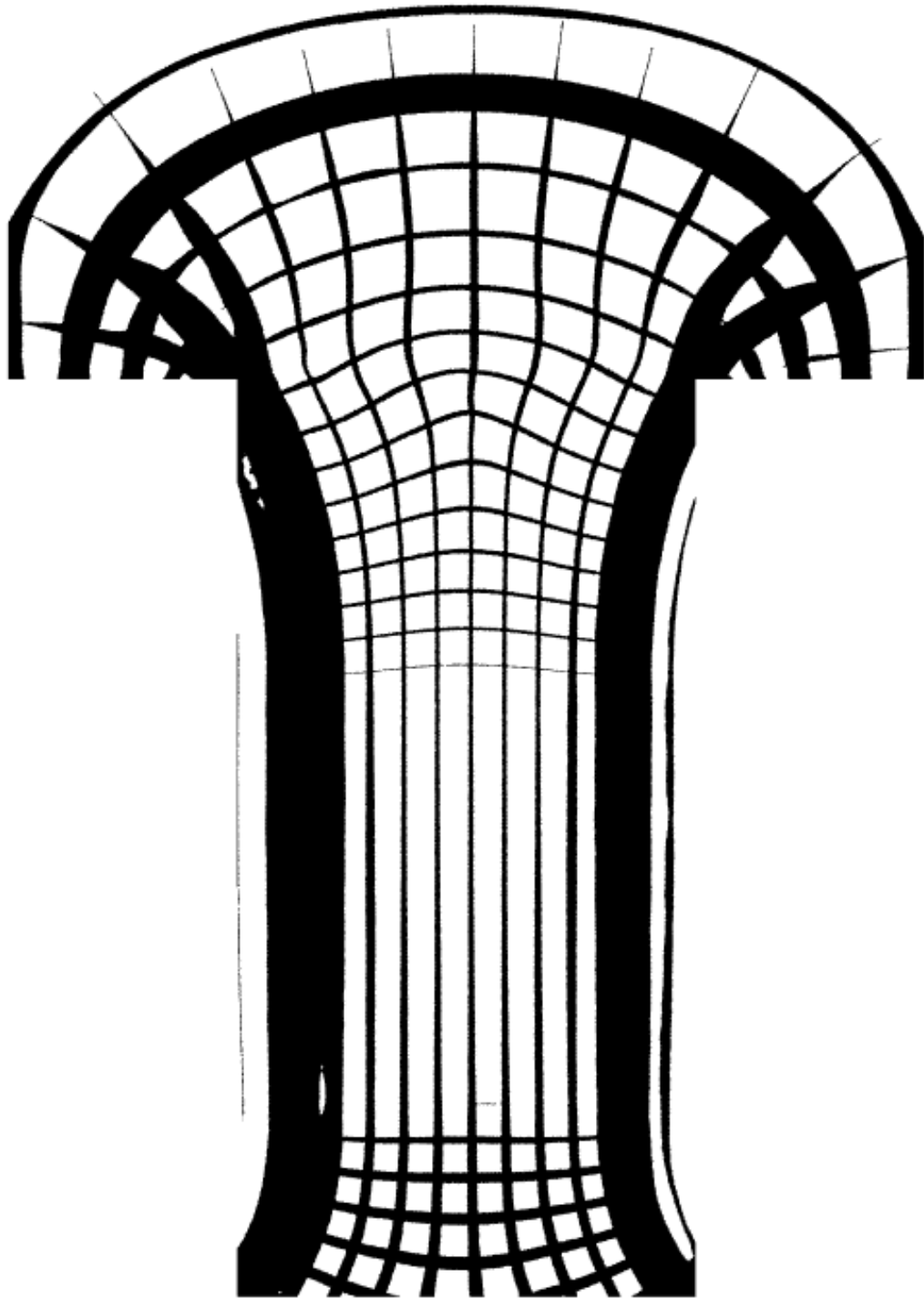
(c)
Figure 4.24 Optimized structures with three different periodicity (a) ϵ=0.375, (b) 0.5, and (c)1.

5   CONCLUSIONS

A new method for load flow determination in two-dimensional space was developed by taking advantage of the load function partial derivatives being equal to the stresses and satisfying the equilibrium equation automatically (similar to the Airy stress function in solid mechanics). The total derivative of load functions is equal to the amount of load flow similar to streamlines in fluid mechanics. No assumption for loading and boundary conditions are made in theoretical or computational development. The load paths for various plane stress structures with different boundary conditions and loadings were determined. The results were compared with those available in the literature.

The four main advantages of the proposed load path method are its *computational efficiency*, requiring only a *single structural analysis*; *computational simplicity,* which makes possible the easy integration into a computational software; *elimination of post-processing* to show the load contours, and its capability to obtain both load paths and the *amount of load flow*.

Secondly, the load function for plate and shell structures was formulated and determined. Load function was used to find the trajectory of load flow and the amount of transferred load between level sets (contours) of the load function. The expansion of the load function method in-plane elasticity to plate and shells is carried out using the Helmholtz decomposition. Because of the existence of the source term (pressure) in equilibrium equations, similar to body force in plane elasticity, it is necessary to decompose the resultant stress field to solenoidal and irrotational parts. It has been shown that the solenoidal part represents the load function in plates and shells and for the special case of plate, the irrotational part is equivalent of the moment transfer in the structure.

Finally, the closed mathematical form of the load functions in two-dimensional space was used as a tool to formulate optimization problems in terms of load functions. This approach has distinct advantages as it reduces the number of variables and constraints in compliance and stress minimization problems leading to computational cost savings. The stresses are replaced with load functions that represent the load transfer in x and y directions. Since the load path functions satisfy the equilibrium equations, the replacement reduces the number of optimization constraints, as well as the number of variables. Using the optimized load functions, the optimal stresses, principal stresses, principal directions, and density are determined.

The dimensions of the square periodic microstructure were also determined using the optimal density and optimal principal stresses. The orientation of the periodic microstructure was determined using principal load paths that are aligned with the principal stress eigenvectors. Because of singularities in the principal stress vector field (angle rotation by π), an interpolation scheme is used to reconstruct a coherent vector field. The numerical scheme to determine the principal load paths considers the principal vector field curl free. Since this is not always the case, a dilation field is used and multiplied by the principal stress field to obtain the curl free component. The optimal structure is constructed using the principal load paths and the microstructure dimensions using cosine wave functions. The resulting optimal structure resembles the lay-out in the Michell lattice design.

6   RECOMMENDATIONS FOR RESEARCH

Considering the computational efficiency of the load path optimization method, it can be extended to 3D structures. Since the load path function that satisfies equilibrium does not exist in 3D, the optimization with respect to stresses can be done directly without using any load function in the optimization process. The post processing and determination of the periodic cubic microstructure can be carried out in the same manner as in 2D. The author intends to expand this method to 3D wing structure in the future to show the application of load path optimization in aerospace structures.

Other future work would be using other microstructure geometry, such as hexagon or triangle, for structural optimization. The main challenges for non-square microstructures are that the number of variables would increase for non-regular microstructures. However, since this method performs the optimization on a coarse mesh, and then projects to the fine mesh, the computational burden of adding variables is not significant.

Another extension of this work could be using the level set method with load path and variational methods as explained in Appendix for optimization. In this scheme, the load functions would be the new variables and the boundary of the structure is varied based on the sensitivity of the objective function (e.g, compliance). The sensitivity of the objective function determines the variation of the level set function which propagates using the Hamilton-Jacobi PDE.

REFERENCES

Aage, N., Andreassen, E., Lazarov, B. S., & Sigmund, O. (2017). Giga-voxel computational morphogenesis for structural design. *Nature, 550*(7674), 84-86. doi: 10.1038/nature23911

Aage, Niels, Andreassen, Erik, & Lazarov, Boyan Stefanov. (2014). Topology optimization using PETSc: An easy-to-use, fully parallel, open source topology optimization framework. *Structural and Multidisciplinary Optimization, 51*(3), 565-572. doi: 10.1007/s00158-014-1157-0

Admal, Nikhil Chandra, & Tadmor, EB. (2016). The non-uniqueness of the atomistic stress tensor and its relationship to the generalized Beltrami representation. *Journal of the Mechanics and Physics of Solids, 93*, 72-92.

Allaire, Grégoire. (2001). *Shape optimization by the homogenization method*. New York: Springer.

Allaire, Grégoire, & Brizzi, Robert. (2005). A multiscale finite element method for numerical homogenization. *Multiscale Modeling & Simulation, 4*(3), 790-812.

Allaire, Grégoire, Geoffroy-Donders, Perle, & Pantz, Olivier. (2018). Topology optimization of modulated and oriented periodic microstructures by the homogenization method.

Allaire, Grégoire, Gournay, F de, Jouve, François, & Toader, A-M. (2005). Structural optimization using topological and shape sensitivity via a level set method. *Control and cybernetics, 34*, 59-80.

Allaire, Grégoire, Jouve, François, & Toader, Anca-Maria. (2004). Structural optimization using sensitivity analysis and a level-set method. *Journal of computational physics, 194*(1), 363-393.

Allaire, Grégoire, & Kohn, Robert. (1993). Optimal design for minimum weight and compliance in plane stress. *European Journal of Mechanics, A/Solids, 12*, 839-878.

Ashby, MF. (2006). The properties of foams and lattices. *Philosophical Transactions of the Royal Society of London A: Mathematical, Physical and Engineering Sciences, 364*(1838), 15-30.

Bendsøe, Martin P, Ben-Tal, Aharon, & Zowe, Jochem. (1994). Optimization methods for truss geometry and topology design. *Structural optimization, 7*(3), 141-159.

Bendsøe, Martin Philip, & Kikuchi, Noboru. (1988). Generating optimal topologies in structural design using a homogenization method. *Computer methods in applied mechanics and engineering, 71*(2), 197-224. doi: https://doi.org/10.1016/0045-7825(88)90086-2

Bendsoe, Martin Philip, & Sigmund, Ole. (2003). *Topology optimization: theory, methods and applications*: Springer.

Bouchitté, Guy, Gangbo, Wilfrid, & Seppecher, Pierre. (2008). Michell trusses and lines of principal action. *Mathematical Models and Methods in Applied Sciences, 18*(09), 1571-1603.

Céa, Jean. (1986). Conception optimale ou identification de formes, calcul rapide de la dérivée directionnelle de la fonction coût. *ESAIM: Mathematical Modelling and Numerical Analysis, 20*(3), 371-402.

Coelho, P. G., Guedes, J. M., & Rodrigues, H. C. (2015). Multiscale topology optimization of bi-material laminated composite structures. *Composite Structures, 132*, 495-505. doi: 10.1016/j.compstruct.2015.05.059

Coelho, Pedro G., Cardoso, João B., Fernandes, Paulo R., & Rodrigues, Hélder C. (2011). Parallel computing techniques applied to the simultaneous design of structure and material. *Advances in Engineering Software, 42*(5), 219-227. doi: 10.1016/j.advengsoft.2010.10.003

Cutrì, M. T.   . (2015). Pier Luigi Nervi e l'architettura strutturale. .

Fosdick, Roger, & Royer-Carfagni, Gianni. (2005). A Stokes theorem for second-order tensor fields and its implications in continuum mechanics. *International Journal of Non-Linear Mechanics, 40*(2), 381-386. doi: https://doi.org/10.1016/j.ijnonlinmec.2004.07.006

Fosdick, Roger, & Schuler, Karl. (2003). Generalized Airy stress functions. *Meccanica, 38*(5), 571-578.

Fujii, D, Chen, BC, & Kikuchi, Noboru. (2001). Composite material design of two-dimensional structures using the homogenization design method. *International journal for numerical methods in engineering, 50*(9), 2031-2051.

Gerald, Curtis F. (2004). *Applied numerical analysis*: Pearson Education India.

Gharibi, Kaveh, Hurley, Joel, & Tamijani, Ali. (2017). *Determination of Load Paths in Plates and Shells Using Load Path Function.* Paper presented at the 58th AIAA/ASCE/AHS/ASC Structures, Structural Dynamics, and Materials Conference.

Graczykowski, C, & Lewiński, T. (2006). Michell cantilevers constructed within trapezoidal domains—Part I: geometry of Hencky nets. *Structural and Multidisciplinary Optimization, 32*(5), 347-368.

Graczykowski, C, & Lewiński, T. (2007). Michell cantilevers constructed within trapezoidal domains. *Structural and Multidisciplinary Optimization, 33*(2), 113-129.

Groen, Jeroen P., & Sigmund, Ole. (2018). Homogenization-based topology optimization for high-resolution manufacturable microstructures. *International journal for numerical methods in engineering, 113*(8), 1148-1163. doi: 10.1002/nme.5575

Guedes, JoséMiranda, & Kikuchi, Noboru. (1990). Preprocessing and postprocessing for materials based on the homogenization method with adaptive finite element methods. *Computer methods in applied mechanics and engineering, 83*(2), 143-198.

Guest, J. K., Prévost, J. H., & Belytschko, T. (2004). Achieving minimum length scale in topology optimization using nodal design variables and projection functions. *International journal for numerical methods in engineering, 61*(2), 238-254. doi: 10.1002/nme.1064

Gurtin, Morton E. (1963). A generalization of the Beltrami stress functions in continuum mechanics. *Archive for Rational Mechanics and Analysis, 13*(1), 321-329.

Harasaki, Hirofumi, & Arora, Jasbir S. (2001). New concepts of transferred and potential transferred forces in structures. *Computer methods in applied mechanics and engineering, 191*(3), 385-406.

Hemp, WS. (1966). Studies in the theory of Michell structures *Applied Mechanics* (pp. 621-628): Springer.

Hoshino, Hiroaki, Sakurai, Toshiaki, & Takahashi, Kunihiro. (2003). Vibration reduction in the cabins of heavy-duty trucks using the theory of load transfer paths. *JSAE Review, 24*(2), 165-171.

Hotz, Ingrid, Sreevalsan-Nair, Jaya, Hagen, Hans, & Hamann, Bernd. (2010). *Tensor field reconstruction based on eigenvector and eigenvalue interpolation.* Paper presented at the Dagstuhl Follow-Ups.

Hou, Thomas Y, & Wu, Xiao-Hui. (1997). A multiscale finite element method for elliptic problems in composite materials and porous media. *Journal of computational physics, 134*(1), 169-189.

Jog, Chandrashekhar S, Haber, Robert B, & Bendsøe, Martin P. (1994). Topology design with optimized, self-adaptive materials. *International Journal for Numerical Methods in Engineering, 37*(8), 1323-1350.

Kelly, D, Reidsema, C, Bassandeh, A, Pearce, G, & Lee, M. (2011). On interpreting load paths and identifying a load bearing topology from finite element analysis. *Finite Elements in Analysis and Design, 47*(8), 867-876.

Kelly, DW, & Elsley, M. (1995). A procedure for determining load paths in elastic continua. *Engineering Computations, 12*(5), 415-424.

Kelly, DW, & Tosh, MW. (2000). Interpreting load paths and stress trajectories in elasticity. *Engineering Computations, 17*(2), 117-135.

Kohn, Robert V, & Strang, Gilbert. (1986a). Optimal design and relaxation of variational problems, I. *Communications on pure and applied mathematics, 39*(1), 113-137.

Kohn, Robert V, & Strang, Gilbert. (1986b). Optimal design and relaxation of variational problems, II. *Communications on pure and applied mathematics, 39*(2), 139-182.

Kohn, Robert V, & Strang, Gilbert. (1986c). Optimal design and relaxation of variational problems, III. *Communications on pure and applied mathematics, 39*(3), 353-377.

Larson, Mats G, & Bengzon, Fredrik. (2013). *The finite element method: theory, implementation, and applications* (Vol. 10): Springer Science & Business Media.

Locatelli, Davide. (2012). *Optimization of Supersonic Aircraft Wing-Box Using Curvilinear SpaRibs.* Virginia Polytechnic Institute and State University.

Lu, Kerr-Jia, & Kota, Sridhar. (2005). An effective method of synthesizing compliant adaptive structures using load path representation. *Journal of Intelligent Material Systems and Structures, 16*(4), 307-317.

Michell, A. G. M. (1904). LVIII. The limits of economy of material in frame-structures. *Philosophical Magazine Series 6, 8*(47), 589-597. doi: 10.1080/14786440409463229

Nakshatrala, P. B., Tortorelli, D. A., & Nakshatrala, K. B. (2013). Nonlinear structural design using multiscale topology optimization. Part I: Static formulation. *Computer methods in applied mechanics and engineering, 261-262*, 167-176. doi: 10.1016/j.cma.2012.12.018

Pantz, O., & Trabelsi, K. (2008). A Post-Treatment of the Homogenization Method for Shape Optimization. *SIAM Journal on Control and Optimization, 47*(3), 1380-1398. doi: 10.1137/070688900

Pedersen, Pauli. (1987). On Sensitivity Analysis and Optimal Design of Specially Orthotropic Laminates. *Engineering Optimization, 11*(3-4), 305-316. doi: 10.1080/03052158708941053

Pedersen, Pauli. (1989). On optimal orientation of orthotropic materials. *Structural optimization, 1*(2), 101-106.

Pejhan, Khashayar, Kuznetcov, Anton, Wang, Qingguo, Wu, Christine Q, & Telichev, Igor. (2018). Design assessment of a multiple passenger vehicle component using load transfer index U* method. *International Journal of Mechanics and Materials in Design, 14*(2), 213-229.

Pejhan, Khashayar, Wang, Qingguo, Wu, Christine Q, & Telichev, Igor. (2017). Experimental validation of the U* index theory for load transfer analysis. *International Journal of Heavy Vehicle Systems, 24*(3), 288-304.

Rodrigues, H., Guedes, J. M., & Bendsoe, M. P. (2002). Hierarchical optimization of material and structure. *Structural and Multidisciplinary Optimization, 24*(1), 1-10. doi: 10.1007/s00158-002-0209-z

Sakurai, Toshiaki, Takahashi, Kunihiro, Kawakami, Hiroshi, & Abe, Masatoshi. (2007). Reduction of calculation time for load path U* analysis of structures. *Journal of Solid Mechanics and Materials Engineering, 1*(11), 1322-1330.

Santer, M, & Pellegrino, S. (2009). Topological optimization of compliant adaptive wing structure. *AIAA journal, 47*(3), 523-534.

Sethian, James A, & Wiegmann, Andreas. (2000). Structural boundary design via level set and immersed interface methods. *Journal of computational physics, 163*(2), 489-528.

Sethian, James Albert. (1999). *Level set methods and fast marching methods: evolving interfaces in computational geometry, fluid mechanics, computer vision, and materials science* (Vol. 3): Cambridge university press.

Shang, Weiyan, & Wang, Qingguo. (2018). Design of a Submarine Vehicle for Higher Natural Frequency Using U Index Theory Approach. *Shock and Vibration, 2018*, 8. doi: 10.1155/2018/9496026

Simon, Jacques. (1980). Differentiation with respect to the domain in boundary value problems. *Numerical Functional Analysis and Optimization, 2*(7-8), 649-687.

Sivapuram, Raghavendra, Dunning, Peter D, & Kim, H Alicia. (2016). Simultaneous material and structural optimization by multiscale topology optimization. *Structural and Multidisciplinary Optimization, 54*(5), 1267-1281.

Soko*f*owski, Jan, & Żochowski, Antoni. (2001). Topological Derivatives of Shape Functionals for Elasticity Systems*. *Mechanics of Structures and Machines, 29*(3), 331-349. doi: 10.1081/sme-100105654

Strang, Gilbert, & Kohn, Robert V. (1983). Hencky-Prandtl nets and constrained Michell trusses. *Computer methods in applied mechanics and engineering, 36*(2), 207-222.

Svanberg, Krister. (1981). On local and global minima in structural optimization: ROYAL INST OF TECH STOCKHOLM (SWEDEN).

Svanberg, Krister. (1987). The method of moving asymptotes—a new method for structural optimization. *International journal for numerical methods in engineering, 24*(2), 359-373.

Tamijani, Ali Y, & Gharibi, Kaveh. (2016). Load Paths Visualization in Plane Elasticity Using Load Path Function Method.

Tamijani, Ali Y, Gharibi, Kaveh, Kobayashi, Marcelo H, & Kolonay, Raymond M. (2017). Load paths visualization in plane elasticity using load function method. *International Journal of Solids and Structures*.

Tamijani, Ali Y, Hurley, Joel, & Gharibi, Kaveh. (2018). Determination of load paths in plates and shells. *Thin-Walled Structures, 127*, 646-653.

Timoshenko, S, & Goodier, JN. (1951). Theory of elasticity. . *New York, 412*, 108.

Ugural, Ansel. (1999). *Stresses in plates and shells*: McGraw-Hill.

Vanderplaats, Garret N., & Salajegheh, Eysa. (1989). New approximation method for stress constraints in structural synthesis. *AIAA journal, 27*(3), 352-358. doi: 10.2514/3.10119

Vanderplaats, GN, & Thomas, HL. (1993). An improved approximation for stress constraints in plate structures. *Structural optimization, 6*(1), 1-6.

Venkataraman, Satchi, Marhadi, Kun S, & Haney, Mark A. (2009). Investigating Alternate Load Paths and Damage Tolerance of Structures Optimized for Multiple Load Cases. *Proceedings AIAA*

Waldman, W, Heller, M, Kaye, R, & Rose, F. (2002). Advances in two-dimensional structural loadflow visualisation. *Engineering Computations, 19*(3), 305-326.

Wang, Michael Yu, Wang, Xiaoming, & Guo, Dongming. (2003). A level set method for structural topology optimization. *Computer methods in applied mechanics and engineering, 192*(1), 227-246.

Wang, Qingguo, Pejhan, Khashayar, Telichev, Igor, & Wu, Christine Q. (2017). Extensions of the U* theory for applications on orthotropic composites and

nonlinear elastic materials. *International Journal of Mechanics and Materials in Design, 13*(3), 469-480.

Wang, Qingguo, Pejhan, Khashayar, Telichev, Igor, & Wu, Christine Q. (2016). Extensions of the U* theory for applications on orthotropic composites and nonlinear elastic materials. *International Journal of Mechanics and Materials in Design*, 1-12. doi: 10.1007/s10999-016-9348-z

Wang, Qingguo, Telichev, Igor, & Wu, Christine Q. (2017). A new load transfer index (U*) with considering six degrees of freedom and its application in structural design and analysis. *Mechanics Based Design of Structures and Machines*, 1-15.

Zhang, Weihong, & Sun, Shiping. (2006). Scale-related topology optimization of cellular materials and structures. *International journal for numerical methods in engineering, 68*(9), 993-1011. doi: 10.1002/nme.1743

Zhu, Ji-Hong, Zhang, Wei-Hong, & Xia, Liang. (2016). Topology optimization in aircraft and aerospace structures design. *Archives of Computational Methods in Engineering, 23*(4), 595-622.

APPENDICES

To develop load path based topology optimization, mastery of some structural

optimization methods was required. The author explored truss optimization, and level set

gradient based optimization, and evolutionary optimization.

A. Truss Optimization

For the minimum weight design, the weight of the structure is minimized subject to

the constraints such as maximum allowable stress and the equilibrium equations of the

truss. The mathematical representation of this optimization scheme is as follows:

$$min \sum_{j=1}^{m} a_j l_j$$

$$s.t. \sum_{i=1}^{n} q_j n_{ij} + f_i = 0$$

$$-\alpha a_j < q_j < \alpha a_j$$

In these equations, j represents the index for bars, i is the index for number of

vertices, a_j is the cross section of each bar, l_j is the length of each bar, q_j is the load in

each bar, n_{ij} is the directional cosine matrix of each bar, f_i is the applied load on each

vertex, and α is the maximum allowable stress in each bar. The variables in this problem

are the cross section area of each bar and this problem is linear meaning that the objective

function and the constraint are linear. Hence, this problem is convex and a global optimal

can be determined using linear programming. The results are as follows and they are

identical to the results in the literature (Bendsøe et al., 1994; Bendsoe et al., 2003).

Figure 6.1. Minimum-weight optimal truss in 9 by 5 grid verified based on (Bendsøe et al., 1994; Bendsoe et al., 2003)

Figure 6.2. Minimum-weight optimal truss in 6 by 9 grid verified based on (Bendsøe et al., 1994; Bendsoe et al., 2003)

Figure 6.3. Minimum-weight optimal truss in 9 by 13 grid verified based on (Bendsøe et al., 1994; Bendsoe et al., 2003)

Figure 6.4. Minimum-weight optimal truss in 9 by 19 grid verified based on
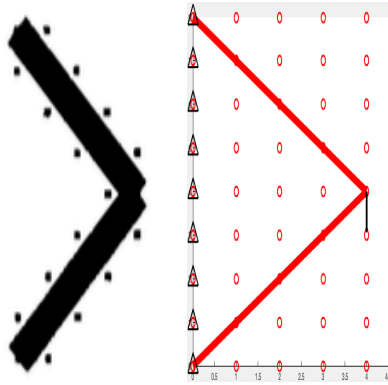(Bendsøe et al., 1994; Bendsoe et al., 2003)

Figure 6.5. Minimum-weight optimal truss in 9 by 9 grid verified based on
(Bendsøe et al., 1994; Bendsoe et al., 2003)

Figure 6.6. Minimum-weight optimal truss in 9 by 25 grid verified based on
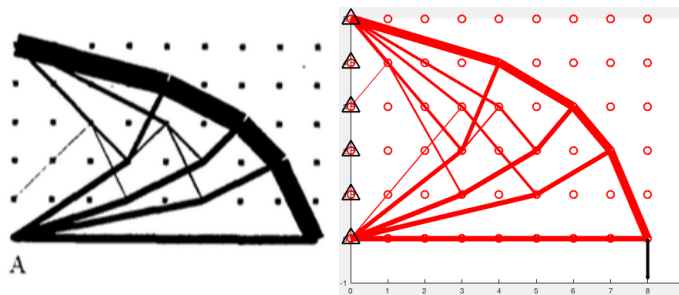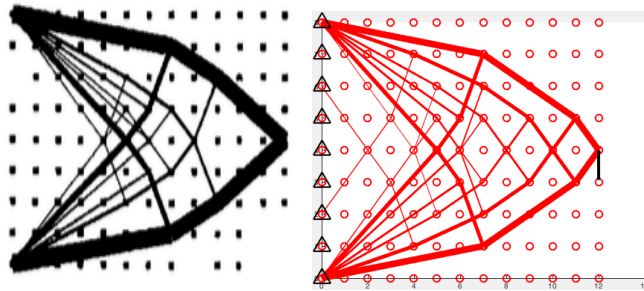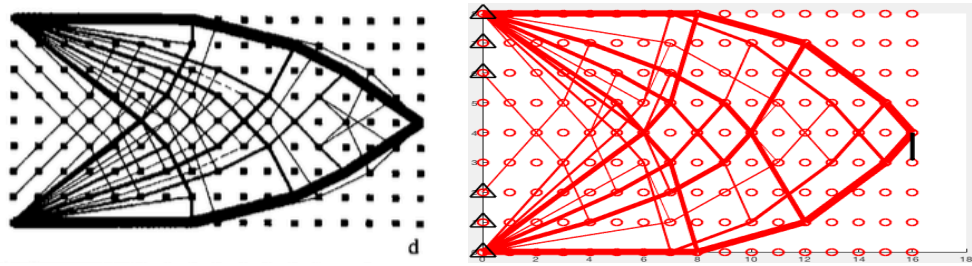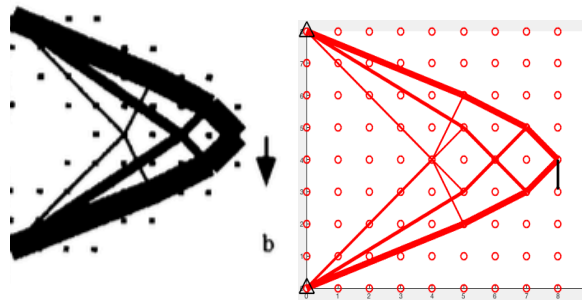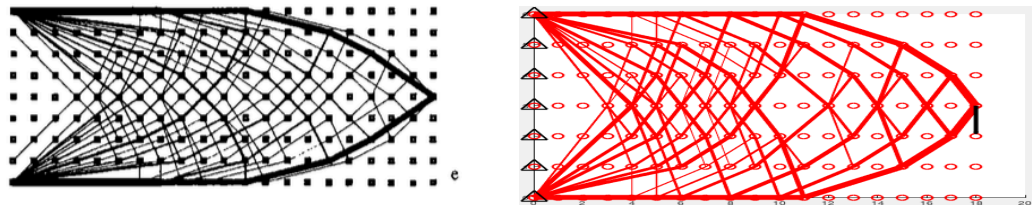(Bendsøe et al., 1994; Bendsoe et al., 2003)

B. Evolutionary Structural Optimization Using Level Set

The formulation of level set method is derived in this section. If we consider the high dimensional surface $\phi(x, y)$, the zero-level set of this function will create a curve on $z=0$. The topological changes in this curve are generated by moving the higher order function or by changing the speed of the higher order function. In other words, the zero level set curve of this function will change or move when $\phi(x, y)$ moves or changes. This representation has great advantage over conventional front propagating methods (Sethian, 1999). It can determine sharp edges and preserve the geometry in corners, whereas using the conventional methods of front propagation the corners and sharp edges will disperse with time. The initial value formulation of level set is as follows:

$$\phi_t + F|\nabla\phi| = 0$$

In this equation ϕ is the higher order level set function, F is the velocity of the level set function at every point on the level set function, $|\nabla\phi|$ is the direction of vector normal to the surface at each point on the level set function, and t is the time. The initial condition for this PDE is the following:

$$\phi(t = 0, x, y) \; is \; given$$

The initial conditions are usually the initial shape of the structure or the holes in the structure at the first step of optimization. The level set is initialized based on the initial shape of the structure. Usually the signed distance function is used for initialization. The areas that are void or holes are having a negative value of distance to the curve, and the areas that are not void have positive value of distance to the propagating curve. The initialization is as follows:

$$\begin{cases} \phi(t = 0, x, y) = d(x, y) & d > 0 \quad not\ void \\ \phi(t = 0, x, y) = -d(x, y) & d < 0 \quad void \end{cases}$$

The distance function $d(x, y)$ is the distance between every point in the x-y plane to the propagating front or the curve that creates the hole. An initialized level set function is shown in the following:
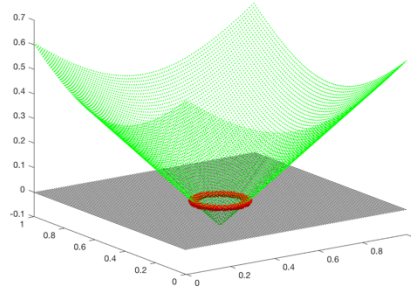
Figure 6.7 The level set function is shown in green and the zero level set is shown in red

Now that the level set is initialized, this PDE, $\phi_t + F|\nabla\phi| = 0$ must be solved. There are various methods for solving this Hyperbolic PDE such as forward in time backward in space (FTCS), Lax method, Lax-Wandroff, MacCormeck method. These methods cannot capture the shape of shock or sharp edges of the propagating front. In other words, these methods do not consider the direction of information propagation. The Upwind method can capture and determine these sharp edges; hence upwind method is used to solve the level set PDE. The discretizing scheme of the PDE based on upwind method is as follows (Sethian, 1999):

$$\phi_i^{n+1} = \phi_i^n - \Delta t \left(\max(F_{ij}, 0) \nabla^+ + \min(F_{ij}, 0) \nabla^- \right)$$

where,

$$\nabla^+ = \max(D_{ij}^{-x}, 0)^2 + \min(D_{ij}^{+x}, 0)^2 + \max(D_{ij}^{-y}, 0)^2 + \min(D_{ij}^{+y}, 0)^2$$

$$\nabla^- = \max(D_{ij}^{+x}, 0)^2 + \min(D_{ij}^{-x}, 0)^2 + \max(D_{ij}^{+y}, 0)^2 + \min(D_{ij}^{-y}, 0)^2$$

where,

$$D_{ij}^{-x} = (\phi_{i,j} - \phi_{i-1,j})/\Delta x \; ; D_{ij}^{+x} = (\phi_{i+1,j} - \phi_{i,j})/\Delta x$$

$$D_{ij}^{-y} = (\phi_{i,j} - \phi_{i,j-1})/\Delta y; D_{ij}^{+y} = (\phi_{i,j+1} - \phi_{i,j})/\Delta y$$

This discretized scheme is used to find the level set at each time step and the zero-level set can be found which represents the propagating front. The Courant-Fredrick-Levy (CFL) conditions of stability must be satisfied in each time step to have the accurate and relevant results. The proof of CFL can be found in numerical method books (Gerald, 2004). The CFL condition for level set can be written as follows:

$$\max(F)\Delta t \leq \Delta x$$

In other words, the speed of propagation of level set must not exceed passing one element on mesh at each time step. This ensures the numerical stability of the level set function. A simple example of the level set propagation is shown in the following:

(a)   (b)
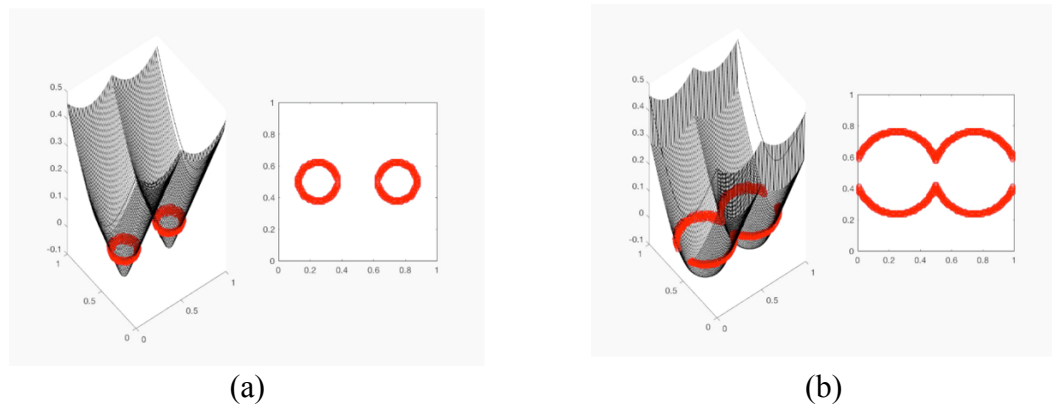
Figure 6.8 The evolution from (a) to (b) of the level set function (black), and the propagating front (red)

As can be seen in Figure 6.8, the zero-level set of the higher order 3D level set function on left is represents the geometry in 2D. Another important step is to reinitialize the level set in every five time-step to avoid flat or steep level set. Reinitializing will make the gradient level set function one by using the distance function as level set every five time-time step (Sethian, 1999).

Velocity Extension of Level set method

In previous sections, the level set formulation and numerical scheme to solve the

Level set hyperbolic PDE was discussed. In this section, the Level set velocity F is

discussed. The velocity of the level set depends on how the physical problem is related to

level set. For example, in fluid dynamics the level set velocity is the velocity of the fluid.

In aircraft collision avoidance, the velocity is the velocity of the aircraft. In structural

optimization, the velocity can be the von Mises stress (Sethian et al., 2000) or the

sensitivity of objective function to the topology (Allaire et al., 2004). In this research, I

have used the von-misses stress as the velocity of level set as it has been used by Sethian

to verify the results. To calculate the von Mises stress at each time step the equilibrium

equations are solved using finite element method and the von Mises stress is calculated in

the design domain.

$$-\mu\left(2u_{xx} + u_{yy} + v_{xy}\right) - \lambda\left(u_{xx} + v_{xy}\right) = f^u$$

$$-\mu\left(2v_{yy} + u_{xy} + v_{xx}\right) - \lambda\left(u_{xx} + v_{yy}\right) = f^v$$

where,

$$\lambda = \frac{Ev}{(1+v)(1-2v)}$$

$$\mu = \frac{E(1-v)}{(1+v)(1-2v)}$$

Also u and v are displacements, f^u and f^v are external forces, E and v are module

of elasticity and poisons ratio. After solving these equations using finite element method,

the von Mises can be found using the following:

$$\sigma = \frac{\mu(\nabla u + \nabla u^T)}{2} + \lambda trace(\nabla u)I$$

Then the velocity of the level set is chosen based on the von Mises stress. The relationship is as follows. This relation is based on ESO. Basically, if the stress is higher than a threshold, the level set front will propagate to increase the hole, and if the stress is more than a threshold, moving the level set fronts backwards will decrease the hole.

$$
\begin{cases}
F = 1 \ if & 10 > \dfrac{\sigma_{max}}{\sigma} > \sigma_{min} \\
\quad F = 0 \ if & 20 > \dfrac{\sigma_{max}}{\sigma} > 10 \\
F = -1 \ if & \sigma_{max} > \dfrac{\sigma_{max}}{\sigma} > 20
\end{cases}
$$

Numerical Examples

Level set method was used to find the optimal topology using the ESO inspired approach. The results are conforming to the ones in literature (Allaire et al., 2004; Bendsoe et al., 2003; Sethian et al., 2000; Wang et al., 2003). All the aforementioned literature use levels set method except one, which uses SIMP (Bendsoe et al., 2003). The results agree with level set methods that used sensitivity analysis of compliance energy, ESO approach level set, and SIMP method. It is important to mention, all of the level set methods find the local optimal and finding the global optimal is not guaranteed because these problems are non-convex. Only convex problems are guaranteed to reach global optimal such as minimum weight problem in truss optimization. However, there are several methods to find the global optimal of non-convex problems such as sequential linear programing (SLP), interior point penalty, and moving asymptotes method (MMA) (Svanberg, 1987). The level set optimal shapes that are shown in Figure 6.9, Figure 6.10, Figure 6.11, and Figure 6.12 are all benchmark problems of topology optimization. A concentrated load is applied on the right-hand side and the left-hand side is clamped to create a cantilever plate.

The most important factors in reaching the optimal in levels set methods are initial conditions, the mesh density of level set function, and the order of elements in finite element solver. Since level set method is based on a hyperbolic PDE with prescribed initial conditions, the solution is highly dependent on the initial conditions and the velocity of propagation. The initial shape can have multiple holes or single hole, with different shapes such as elliptical, circular, square, rectangle, or any arbitrary shape. In the author's experience, there is an optimal value of number of initial holes that can lead to the optimal design faster than others. Another important factor is the speed of level set which is based on the stress in the structure. The speed must be chosen in a manner to satisfy the CFL conditions to maintain numerical stability of level set. If the stability is not maintained, the level set behaves abnormal with abrupt changes.

The other important factor is the density of the mesh on the level set function; this is the mesh that the value of level set function is determined on. This mesh is different with finite element mesh, and ensures the accuracy of the level set function and consequently the zero-level set which is the propagating front. The order of finite element that is used to calculate the structural response is essential to calculate the stress accurately. Using the quadratic element versus linear elements make a lot of difference, and quadratic elements ensure the convergence to the optimal design.

The differences between author's approach and Sethian's approach (Sethian et al., 2000) are as follows. First, the outer boundary of the rectangle design area is not changing in author's approach and through these simulations and results it has been proven to reach to optimal. Second, in author's approach there is no new hole generation, and the holes are the evolution of the initial holes and no new holes are added. This also

has been proven to reach the optimal design. Third, Sethian used immersed method to calculate stresses and I used finite element method. Forth, Sethian uses narrow band level set, whereas, I used the original levels set. Fifth, in author's approach is reinitialized and Sethian does not reinitialize the level set because of using velocity extension method. When velocity extension is parallel to the boundaries the level set does not need re-initialization. The similarities are using level set and ESO approach together for topology optimization.

Figure 6.9. The optimal topology of a 8 by 16 cantilever plate under concentrated load at the tip verified (Allaire, Gournay, et al., 2005)
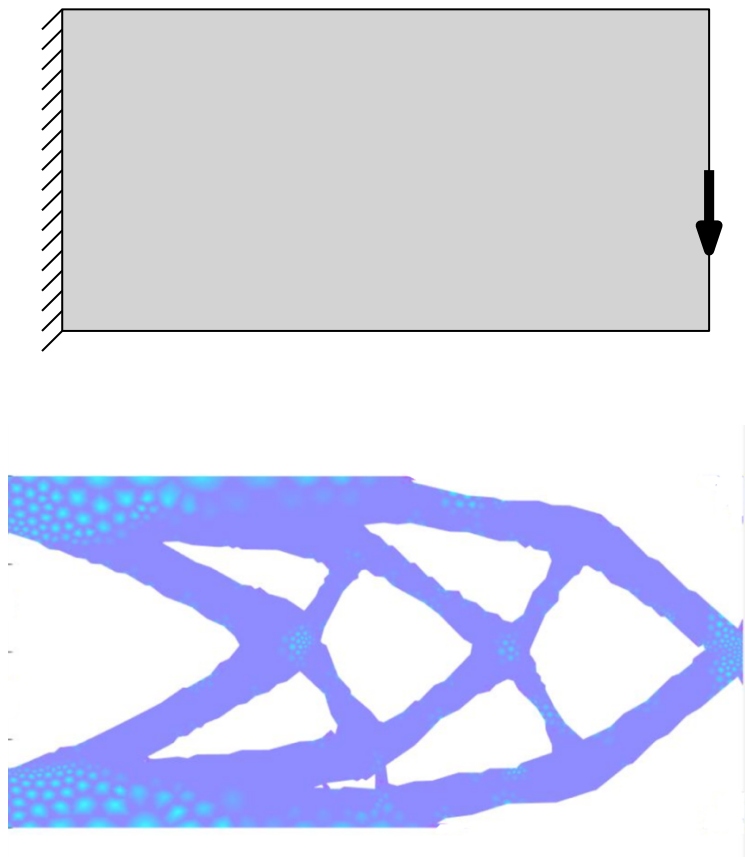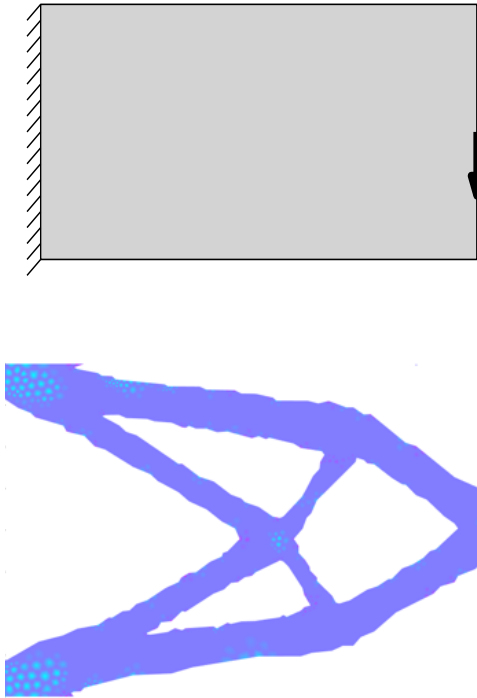
Figure 6.10. The optimal topology of a 8 by 12 cantilever plate under concentrated load at the tip (Bendsoe et al., 2003)

Figure 6.11. The optimal topology of a 1 by 3 cantilever plate under concentrated load at the tip (Wang et al., 2003)
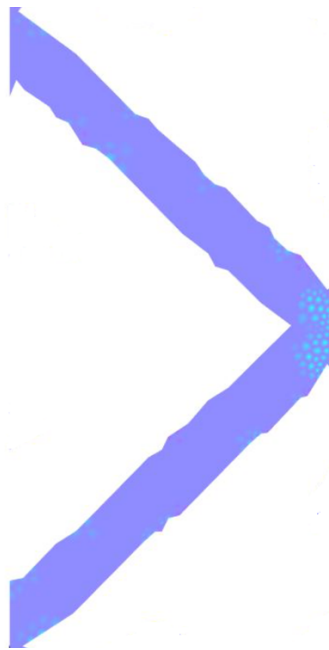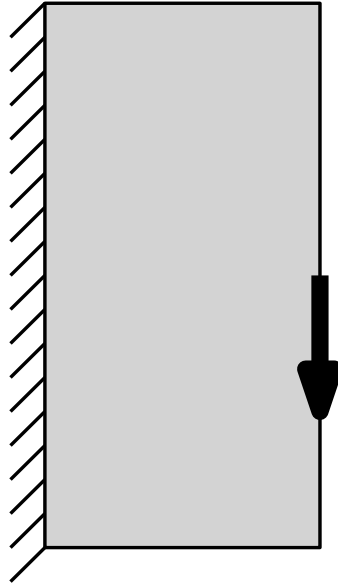
Figure 6.12 The optimal topology of a 2 by 1 cantilever plate under concentrated
load at the tip (Sethian et al., 2000)

C. Gradient Based Topology Optimization Using Level Set

The optimization problem can be posed as follows. The objective function J can be written as follows (Allaire et al., 2004):

$$J = \int_\Omega J(v)dx + \int_{\partial\Omega} l(v)\,ds$$

The constraints are as follows:

$$-\nabla.\left(Ae(v)\right) = f$$

$$v = 0 \; on \; \Gamma_D$$

$$Ae(v)\vec{n} = g \; on \; \Gamma_N$$

$$L(\Omega, v, q, \lambda_1, \lambda_2) = \int_\Omega J(v)dx + \int_{\partial\Omega} l(v)\,ds$$

$$\nabla.\left(Ae(v)\right) = f$$

$$\int_\Omega -q\nabla.\left(Ae(v)\right)dx \; = \int qf dx$$

Using integration by part and divergence theorem:

$$\int_\Omega -q\nabla.\left(Ae(v)\right)dx = -\int \nabla.\left(qA(e(v))\right)dx + \int \nabla qA(e(v))dx$$

$$-\int_\Omega \nabla.\left(qA(e(v))\right)dx = -\int_{\Gamma_N} qA(e(v))\vec{n}\,ds - \int_{\Gamma_D} qA(e(v))\vec{n}\,ds$$

Hence,

$$\int_\Gamma qA(e(v))\vec{n}\,ds + \int \nabla qA(e(v))dx = \int qf dx$$

Hence, the equilibrium constraint can be written in week form as follows:

$$\int_{\Gamma_N} qA(e(v))\vec{n}\,ds + \int_{\Gamma_D} qA(e(v))\vec{n}\,ds + \int_\Omega e(q)A(e(v))dx = \int_\Omega qf dx$$

Replacing the Neumann boundary conditions in the above equation.

$$(Ae(v)\vec{n} - g) = 0$$

$$\int_{\Gamma_N} qg ds + \int_{\Gamma_D} qA(e(v))\vec{n}\, ds + \int_{\Omega} e(q)A(e(v)) dx = \int_{\Omega} qf dx$$

The Dirichlet constraint can be written as follows in week form as follows using the Lagrange multiplier:

$$\int_{\Gamma_D} \lambda_1 v ds = 0$$

Using the Cea's example (Céa, 1986), you can see that $\lambda_1 = -\frac{\partial q}{\partial n}$

$$\int_{\Gamma_D} A\lambda_1 v ds = -\int_{\Gamma_D} A\nabla q\, v\, ds = -\int_{\Gamma_D} Ae(q)\, v ds$$

We derived The Lagrangian as seen above

The next step is to find the derivative of Lagrangian with respect to the variable u and the Lagrange multipliers.

The Lagrangian after the above calculations is as follows:

$$L(\Omega, v, q) = \int_{\Omega} j(v) dx + \int_{\partial\Omega} l(v) ds + \int Ae(v).e(q) dx - \int_{\Omega} q.f dx$$

$$- \int_{\Gamma_N} q.g ds - \int_{\Gamma_D} q.Ae(v)\vec{n} + v.Ae(q)\vec{n} ds$$

The next step is to find the derivative of Lagrange with respect to the variable v and the Lagrange multiplier q.

The Fréchet derivative is defined as follows:

$$< \frac{\partial F}{\partial A}, B > = F'(A; B) = \lim_{\rho \to 0} \frac{F(A + \rho B) - F(A)}{\rho}$$

We use the Fréchet derivative concept to find the optimality conditions.

Basically, we are perturbing variable A in the direction of Vector B, and we find the derivative in the direction of vector B.

Let's find the derivatives with respect to q (Lagrange multiplier) term by term as follows:

$$F = q.Ae(v)\vec{n}$$

$$< \frac{\partial F}{\partial q}, \vec{\phi} >= \frac{\lim_{h\to 0}\left(F(q+h\vec{\phi}) - F(q)\right)}{h} = \frac{\int Ae(v).e(q+h\vec{\phi})dx - \int Ae(v).e(q)dx}{h}$$

Since,

$$e(v) = \frac{\nabla v + \nabla^T v}{2}$$

where *e* is a linear operator,

$$e(q+h\vec{\phi}) = \frac{\nabla(q+h\vec{\phi}) + \nabla^T(q+h\vec{\phi})}{2} = \frac{\nabla q + h\nabla\vec{\phi} + \nabla^T q + h\nabla^T\vec{\phi}}{2} = e(q) + he(\vec{\phi})$$

Replace it in Fréchet derivative:

$$\frac{\int Ae(v).e(q+h\vec{\phi})dx - \int Ae(v).e(q)dx}{h} = \frac{\int hAe(v)e(\phi)dx}{h} = \int Ae(v)e(\phi)dx$$

Let's simplify it more,

$$\int_\Omega Ae(v)e(\phi)dx = \int A(\frac{\nabla v + \nabla^T v}{2})(\frac{\nabla\phi + \nabla^T\phi}{2})$$

We can only calculate the following term the rest are similar to the following by using integration by part:

$$\int_\Omega A\nabla v\nabla\phi dx = \int_\Omega \left(\nabla(\nabla v\,\phi) - \nabla^2 v\,\phi\right)dx = \int_\Gamma \nabla v\phi.\vec{n}ds - \int_\Omega \nabla^2 v\,\phi\,dx$$

$$\int_\Gamma \nabla v\phi.\vec{n}ds - \int_\Omega \nabla^2 v\,\phi\,dx = \int_{\Gamma_N} \nabla v\phi.\vec{n}ds + \int_{\Gamma_D} \nabla v\phi.\vec{n}ds - \int_\Omega \nabla^2 v\,\phi\,dx$$

Let's find the derivative of other terms.

$$F_2 = -\int_\Omega q.f dx - \int_{\Gamma_N} q.g ds - \int_{\Gamma_D} (q.A(v)\vec{n} + v.Ae(q)\vec{n})ds$$

$$< \frac{\partial F_2}{\partial q}, \phi >= -\int_\Omega \phi.f dx - \int_{\Gamma_N} \phi.g ds - \int_{\Gamma_D} \phi.A(v)\vec{n} + vA(e(\phi)\vec{n}$$

Adding all the Fréchet derivatives together yields the Fréchet derivative of the Lagrangian

$$< \frac{\partial L}{\partial q}, \phi > = < \frac{\partial F_2}{\partial q}, \phi > + < \frac{\partial F}{\partial q}, \phi > =$$

$$- \int_\Omega \phi . f \, dx - \int_{\Gamma_N} \phi . g \, ds$$

$$- \int_{\Gamma_D} \phi . A(v)\vec{n} + vA(e(\phi)\vec{n} \int_{\Gamma_N} \nabla v\phi . \vec{n} ds + \int_{\Gamma_D} \nabla v\phi . \vec{n} ds$$

$$- \int_\Omega \nabla . (\nabla v)\phi \, dx$$

$$= \int_\Omega (\nabla . (\nabla v) - f) \, \phi dx + \int_{\Gamma_N} \phi(\nabla v - g) ds + \int_{\Gamma_D} \nabla v . \, \phi$$

$$- \int_{\Gamma_D} \nabla v . \, \phi - \int_{\Gamma_D} v\nabla \phi \vec{n} ds = 0$$

We can do the same for $\nabla^T v$ and will get the same results then we can add the

results together and find the same equation for e.

Now let's find the Fréchet derivatives with respect to variable v (displacement)

$$L(\Omega, v, q) = \int_\Omega j(v) dx + \int_{\partial\Omega} l(v) ds + \int Ae(v) . e(q) dx - \int_\Omega q . f dx$$

$$- \int_{\Gamma_N} q . g ds - \int_{\Gamma_D} q . Ae(v)\vec{n} + v . Ae(q)\vec{n} ds$$

Let's find derivative for the first term

$$J = \int_\Omega j(v) dx$$

$$< \frac{\partial J}{\partial v}, \phi > = \lim_{h \to 0} \frac{\int J(v + h\phi) dx - J(v) dx}{h} = \frac{\lim_{h \to 0} \left(\int J(v) + J'(v)(h\phi) - J(v) \right)}{h}$$

$$= \int_\Omega J'(v)\phi dx$$

Let's find derivative for the third term.

Note: Since strain is $e(v) = \frac{\nabla v + \nabla^T v}{2}$ we can find the derivatives for ∇v and $\nabla^T v$,

and then add them and divide by 2. Hence here we just show the procedure to get

derivative of ∇v. $\nabla(q)$

$$J = \int_\Omega \nabla(v).\nabla(q)dx$$

$$< \frac{\partial J}{\partial v}, \phi >= \lim_{h \to 0} \frac{\int_\Omega \nabla(v + h\phi)\nabla q dx - \nabla(v)\nabla q dx}{h} = \frac{\lim_{h \to 0} \int_\Omega \nabla(h\phi)\nabla q}{h} = \int_\Omega \nabla\phi\nabla q\, dx$$

The next term is $q\nabla v$

Its Fréchet derivative is as follows:

$$J = \int_\Omega q\nabla(v)dx$$

$$< \frac{\partial J}{\partial v}, \phi >= \lim_{h \to 0} \frac{\int_\Omega \nabla(v + h\phi)q dx - \nabla(v)q dx}{h} = \frac{\lim_{h \to 0} \int_\Omega hq\nabla(\phi) + q\nabla v - q\nabla v}{h}$$

$$= \int_\Omega q\nabla\phi\, dx$$

After adding all the derivatives of all the terms of the Lagrangian, the derivative of

the Lagrangian can be written as follows:

$$< \frac{\partial L}{\partial v}, \phi >= \int_\Omega J'(u)\phi dx + \int_{\partial\Omega} l'(u)\phi ds + \int_\Omega \nabla\phi\nabla p - \int_{\Gamma_D} (p\nabla\phi + \phi\nabla p)\,\vec{n} ds$$

Now let's work on the second term.

$$\int_\Omega \nabla\phi\nabla p d\Omega = \int_\Omega \nabla(\phi\nabla p)dx - \int_\Omega \phi\nabla^2 p dx$$

$$= \int_\Gamma \phi\nabla p ds - \int_\Omega \phi\nabla^2 p dx = \int_{\Gamma_D} \phi\nabla p ds + \int_{\Gamma_N} \phi\nabla p ds - \int_\Omega \phi\nabla^2 p dx =$$

Then,

$$< \frac{\partial L}{\partial v}, \phi >= \int_{\Omega} J'(\mathrm{u})\phi - \phi \nabla.(\nabla p) dx$$

$$+ \int_{\Gamma_D} l'(u)\phi - p\nabla\phi\vec{n} ds + \int_{\Gamma_N} l'(u)\phi + \phi\nabla p\vec{n}\ ds$$

To find the adjoint state the derivative of the Lagrangian must be zero. Hence,

$$j'(u) = \nabla.(\nabla p)$$

$$\phi l'(u) = p\nabla\phi$$

$$l'(u) = -\nabla p$$

From the last two equations, we get:

$$-\phi\nabla p = p\nabla\phi$$

Hence,

$$-\phi\nabla p - p\nabla\phi = 0\ \ hence,\ \nabla(p\phi) = 0,\ \ \int_{\Gamma} p\phi ds = 0, \text{ hence } p = 0\ on\ \Gamma$$

There for the adjoint state can be found from

$$j'(u) = \nabla.(\nabla p)\ on\ \Omega$$

$$p = 0\ on\ \Gamma$$

Also from

$$\int_{\Gamma_N} l'(u)\phi + \phi\nabla p\vec{n}\ ds = 0$$

We get

$$\nabla p\vec{n} = -l'(u)$$

Converting all ∇p to $Ae(p)$ we get,

$$j'(u) = \nabla.(Ae(p))\ on\ \Omega$$

$$p = 0\ on\ \Gamma_D$$

$$Ae(p)\vec{n} = -l'(u)\ \ on\ \Gamma_N$$

Now according to adjoint sensitivity formulation we need to find the derivative of the Lagrangian with respect to shape Ω,

$$J(\Omega) = L(\Omega, u(\Omega), p(\Omega))$$

The Fréchet derivative of J with respect to Ω in the direction of vector θ is,

$$J'(\Omega)(\theta) = \frac{\partial L(\Omega, u, p)}{\partial \Omega}(\theta)$$

To get the derivative of the Lagrangian we need some more knowledge.

The Lagrangian is as follows:

$$L(\Omega, v, q) = \int_\Omega j(v)dx + \int_{\partial\Omega} l(v)ds + \int Ae(v).e(q)dx - \int_\Omega q.fdx$$

$$- \int_{\Gamma_N} q.gds - \int_{\Gamma_D} q.Ae(v)\vec{n} + v.Ae(q)\vec{n}ds$$

It can be proven that the shape derivative of Lagrangian is as follows:

$$\frac{\partial L}{\partial \Omega}(\Omega, u, p)(\theta)$$

$$= \int_{\partial\Omega} \theta.n(j(u) + Ae(u).e(p) - p.f)ds + \int_{\partial\Omega} \theta.n(\frac{\partial l(u)}{\partial n} + Hl(u))\,ds$$

$$- \int_{\Gamma_N} \theta.n\left(\frac{\partial(g.p)}{\partial n} + Hg.p\right)ds - \int_{\Gamma_D} \theta.n\left(\frac{\partial h}{\partial n} + Hh\right)ds$$

Where H is $\nabla.n$, and $h = u.Ae(p)n + p.Ae(u)n$

To prove the above Lagrangian the following must be proven.

Assume we have a function on the domain D (Simon, 1980),

$$J(\text{D}) = \int_\text{D} C(u(\text{D}))$$

Another function that

$$K(\text{D}) = \int_{\partial\text{D}} G(u(\text{D}))$$

If we perturb or change the domain D by a perturbation vector of θ, then these integrals will change to new domain $(I + \theta)D$,

$$J(\theta) = \int_{(I+\theta)D} C(u(\theta))$$

$$K(\theta) = \int_{(I+\theta)D} G(u(\theta))$$

Since the new domain after perturbation changing with perturbation θ, when getting the derivative with respect to θ from the integral $J(\theta)$, the derivative can not enter the integral if the domain is a function of θ. Hence, the domain needs to change to the original domain or Lagrangian domain from Eulerian domain.

$$J(\theta) = \int_{(I+\theta)D} C(u(\theta)) = \int_{D} C(u(\theta)).(I + \theta)Jac(I + \theta)$$

Now that we converted the domain to Lagrangian we can take the derivative into the integral hence,

We use the chain rule and because the derivative of the Jacobian is $\nabla.\tau$ in which τ is the perturbation vector,

$$\frac{\partial J(\theta)}{\partial \theta}(0)\tau = \int_{D} \frac{\partial\left(C(u(\theta)).(I + \theta)\right)}{\partial \theta}(0)\tau + C(u(0))\nabla.\tau$$

Let's calculate the derivative of Jacobian here, since the Jacobian represents the following matrix of transformation from one coordinate to another, from x to x' coordinate system, in which x is the Lagrangian coordinate and x' is the Eulerian.

$$x'_1 = x_1 + \tau_1 h$$

$$x'_2 = x_2 + \tau_2 h$$

The Jacobian is determinant of F (i.e. the transformation matrix),

$$F = \frac{\partial x_i'}{\partial xj} = \begin{bmatrix} \frac{\partial x_1'}{\partial x_1} & \frac{\partial x_1'}{\partial x_2} \\ \frac{\partial x_2'}{\partial x_1} & \frac{\partial x_2'}{\partial x_2} \end{bmatrix} = \begin{bmatrix} \frac{\partial(x_1+\tau_1 h)}{\partial x_1} & \frac{\partial(x_1+\tau_1 h)}{\partial x_2} \\ \frac{\partial(x_2+\tau_2 h)}{\partial x_1} & \frac{\partial(x_2+\tau_2 h)}{\partial x_2} \end{bmatrix} = \begin{bmatrix} 1+\frac{h\partial\tau_1}{\partial x_1} & \frac{h\partial\tau_1}{\partial x_2} \\ \frac{h\partial\tau_2}{\partial x_1} & 1+\frac{h\partial\tau_2}{\partial x_2} \end{bmatrix}$$

$$J = \det(F) = \left(1+\frac{h\partial\tau_1}{\partial x_1}\right)\left(1+\frac{h\partial\tau_2}{\partial x_2}\right) - \left(\frac{h\partial\tau_2}{\partial x_1}\right)\left(\frac{h\partial\tau_1}{\partial x_2}\right)$$

If there is no transformation the Jacobian will be as follows:

$$F_0 = \frac{\partial x_i'}{\partial xj} = \begin{bmatrix} \frac{\partial x_1}{\partial x_1} & \frac{\partial x_1}{\partial x_2} \\ \frac{\partial x_2}{\partial x_2} & \frac{\partial x_2}{\partial x_2} \\ \frac{\partial x_2}{\partial x_1} & \frac{\partial x_2}{\partial x_2} \end{bmatrix} = \begin{bmatrix} 1 & 0 \\ 0 & 1 \end{bmatrix}$$

$$J_0 = \det(F_0) = 1$$

Frechet derivative of the F in the direction of vector τ is,

$$<\frac{\partial J}{\partial\theta}, \tau> = \lim_{h\to 0}\frac{J(\det(F)) - J(\det(F_0)))}{h} = \lim_{h\to 0}\frac{\left(\left(1+\frac{h\partial\tau_1}{\partial x_1}\right)\left(1+\frac{h\partial\tau_2}{\partial x_2}\right) - \left(\frac{h\partial\tau_2}{\partial x_1}\right)\left(\frac{h\partial\tau_1}{\partial x_2}\right) - 1\right)}{h} =$$

$$\frac{\partial\tau_1}{\partial x_1} + \frac{\partial\tau_2}{\partial x_2} = \nabla.\tau$$

Now going back to the derivative of the integral over the domain,

$$\frac{\partial J(\theta)}{\partial\theta}(0)\tau = \int_D \frac{\partial\left(C(u(\theta)).(I+\theta)\right)}{\partial\theta}(0)\tau + C(u(0))\nabla.\tau$$

Let's calculate the first term using chain rule. Since this term is in Eulerian coordinates $C(u(\theta)).(I+\theta)$, its derivative with respect to θ, can be written as its derivative with respect to theta, plus its derivative with respect to the Eulerian coordinates multiplied by the derivative of the Eulerian coordinates. You have learned it in continuum mechanics.

$$\frac{\partial\left(C(u(\theta)).(I+\theta)\right)}{\partial\theta}(0)\tau = \frac{\partial\left(C(u(\theta))\right)}{\partial\theta}(0)\tau + \tau.\nabla C(u(0))$$

Also the first term of the above equation is as follows:

$$\frac{\partial\big(C(u(\theta))\big)}{\partial\theta}(0)\tau = \frac{\partial C}{\partial u}\frac{\partial u(\theta)}{\partial\theta}(0)\tau = \frac{\partial C}{\partial u}u'$$

$$\frac{\partial J(\theta)}{\partial\theta}(0)\tau = \int_D \frac{\partial C}{\partial u}u' + \tau.\nabla C(u(0)) + C(u(0))\nabla.\tau$$

The theory is Proven.

Now finding the derivative of integral on a surface in Lagrangian domain (initial shape coordinate system).

$$K(\mathrm{D}) = \int_{\partial\mathrm{D}} G(u(\mathrm{D}))$$

In terms of the perturbation θ, in the Eulerian domain (after shape is perturbed by θ to $(I + \theta)\mathrm{D}$,

$$K(\theta) = \int_{\partial(I+\theta)\mathrm{D}} G(u(\theta))$$

To get the derivative $\frac{\partial K}{\partial\theta}$ since the domain is changing with θ, we can not take the derivative inside the integral, so we first change the Eulerian domain to Lagrangian, hence we need to multiply the integrand to the Jacobian of surface.

$$K(\theta) = \int_{\partial\mathrm{D}} G(u(\theta))(I + \theta)Jac_{\partial D}(I + \theta)$$

Now the derivative in the direction of τ is calculated as follows:

$$\frac{\partial K}{\partial\theta}(0)\tau = \int_{\partial\mathrm{D}} \frac{\partial\Big(G(u(\theta))(I + \theta)Jac_{\partial D}(I + \theta)\Big)}{\partial\theta}(0)\tau$$

Using the chain rule,

$$\frac{\partial K}{\partial\theta}(0)\tau = \int_{\partial\mathrm{D}} \frac{\partial\Big(G(u(\theta))(I + \theta)\Big)}{\partial\theta}(0)\tau + \frac{\partial(Jac_{\partial D}(I + \theta))}{\partial\theta}G(u(0))$$

It can be shown that the $\frac{\partial(Jac_{\partial D}(I+\theta))}{\partial\theta} = \nabla_{\partial D}.(\tau)$

Also from continuum mechanics we know that the Jacobian term on the surface is

$Jac_{\partial D} = Jac_D(F^{-1})^T$ in which $F = \frac{\partial x_i}{\partial X_j}$, and x_i is the Eulerian coordinate system and X_j is

Lagrangian.

Also in continuum mechanics, we have learned that the,

$$\nabla_{\partial D}.(\tau) = \nabla.\tau - \dot{\tau}n.n$$

$$\frac{\partial K}{\partial \theta}(0)\tau = \int_{\partial D} \frac{\partial\left(G(u(\theta))(I+\theta)\right)}{\partial \theta}(0)\tau + \frac{\partial(Jac_{\partial D}(I+\theta))}{\partial \theta}G(u(0))$$

$$= \int_{\partial D} \frac{\partial\left(G(u(\theta))(I+\theta)\right)}{\partial \theta}(0)\tau + \nabla_{\partial D}.(\tau)\,G(u(0))$$

Using the chain rule, we can right the partial in Eulerian in terms of partial in Lagrangian,

$$\frac{\partial\left(G(u(\theta)).(I+\theta)\right)}{\partial \theta}(0)\tau = \frac{\partial(G(u(\theta)))}{\partial \theta}(0)\tau + \tau.\nabla G(u(0))$$

Also, using the chain rule

$$\frac{\partial(G(u(\theta)))}{\partial \theta}(0)\tau = \frac{\partial G}{\partial u}\frac{\partial u(\theta)}{\partial \theta}(0)\tau = \frac{\partial G}{\partial u}u'$$

$$\frac{\partial K}{\partial \theta}(0)\tau = \int_{\partial D} \frac{\partial G}{\partial u}u' + \tau.\nabla\left(G(u(0))\right) + \nabla_{\partial D}.(\tau)G(u(0))$$

Now we decompose the $\nabla\left(G(u)\right)$ into normal and tangential components according

to the following equation:

$$\nabla_{\partial D}g = \nabla\hat{g} - n\frac{\partial\hat{g}}{\partial n}$$

Where g is the level set of $\hat{g}$.

You can see this in the following example.

$$g: x^2 + y^2 = 1$$

$$\hat{g}: Z = x^2 + y^2 - 1$$

As you can see g is the zero-level set of $\hat{g}$,

$$\nabla_{\partial D}\, g = 2x\,i + 2y\,j$$

$$\nabla \hat{g} = 2x\,i + 2y\,j - k$$

$$n\frac{\partial \hat{g}}{\partial n} = -k$$

As can be seen the equation is satisfied.

$$\nabla_{\partial D} g = \nabla \hat{g} - n\frac{\partial \hat{g}}{\partial n}$$

$$\frac{\partial K}{\partial \theta}(0)\tau = \int_{\partial D}\frac{\partial G}{\partial u}u' + \tau.\nabla\big(G(u(0))\big) + \nabla_{\partial D}.(\tau)G(u(0))$$

Decomposing $\tau.\nabla\big(G(u(0))\big)$,

$$\frac{\partial K}{\partial \theta}(0)\tau = \int_{\partial D}\frac{\partial G}{\partial u}u' + \tau.\nabla\big(G(u(0))\big) + \nabla_{\partial D}.(\tau)G(u(0))$$

$$= \int_{\partial D}\tau\nabla_{\partial D}G\big(u(0)\big) + \tau.n\frac{\partial G\big(u(0)\big)}{\partial n} + \frac{\partial G}{\partial u}u' + \nabla_{\partial D}.(\tau)G\big(u(0)\big)$$

The sum of these terms is,

$$\tau\nabla_{\partial D}G\big(u(0)\big) + \nabla_{\partial D}.(\tau)G\big(u(0)\big) = \nabla_{\partial D}.(\tau G(u(0))$$

$$\int_{\partial D}\tau.n\frac{\partial G\big(u(0)\big)}{\partial n} + \frac{\partial G}{\partial u}u' + \nabla_{\partial D}.(\tau G(u(0)) =$$

To find divergence on the boundary consider the following:

$$v_{\partial D} = v - n(n.v)$$

$$\nabla.v_{\partial D} = \nabla.v - \nabla.n(n.v)$$

We call $H = \nabla.n$

Using the equation above,

$$\nabla_{\partial D}.(\tau_{\partial D}G(u(0)) = \nabla.(\tau G\big(u(0)\big) - \tau.nHG(u(0))$$

$$\nabla.\left(\tau G\big(u(0)\big)\right) = \nabla_{\partial D}.\left(\tau_{\partial D}G\big(u(0)\big)\right) + \tau.nHG\big(u(0)\big)$$

Then,

$$\int_{\partial D} \tau.n\frac{\partial G\big(u(0)\big)}{\partial n} + \frac{\partial G}{\partial u}u' + \nabla_{\partial D}.\left(\tau_{\partial D}G\big(u(0)\big)\right) + \tau.nHG\big(u(0)\big)$$

The term,

$$\int_{\partial D} \nabla_{\partial D}.\left(\tau_{\partial D}G\big(u(0)\big)\right) = \int_{\partial D} \left(\tau_{\partial D}G\big(u(0)\big).\vec{n}\right) = 0$$

Because $\tau_{\partial D}.\vec{n} = 0$, because $\tau_{\partial D}$ is tangent to the curve and perpendicular to $\vec{n}$.

$$\frac{\partial K}{\partial \theta}(0)\tau = \int_{\partial D} \tau.n\frac{\partial G\big(u(0)\big)}{\partial n} + \frac{\partial G}{\partial u}u' + \tau.nHG\big(u(0)\big)$$

proved.

We can use these proven equations to find the shape derivative of the Lagrangian,

$$L(\Omega, v, q) = \int_{\Omega} j(v)dx + \int_{\partial\Omega} l(v)ds + \int Ae(v).e(q)dx - \int_{\Omega} q.fdx$$

$$- \int_{\Gamma_N} q.gds - \int_{\Gamma_D} q.Ae(v)\vec{n} + v.Ae(q)\vec{n}ds$$

as follows:

$$\frac{\partial L}{\partial\Omega}(\Omega, u, p)(\theta)$$

$$= \int_{\partial\Omega} \theta.n\big(j(u) + Ae(u).e(p) - p.f\big)ds + \int_{\partial\Omega} \theta.n\left(\frac{\partial l(u)}{\partial n} + Hl(u)\right) ds$$

$$- \int_{\Gamma_N} \theta.n\left(\frac{\partial(g.p)}{\partial n} + Hg.p\right)ds - \int_{\Gamma_D} \theta.n\left(\frac{\partial h}{\partial n} + Hh\right)ds$$

where H is $\nabla.n$, and $h = u.Ae(p)n + p.Ae(u)n$

After also applying the boundary conditions

$$u = p = 0 \; on \; \Gamma_D$$

$$Ae(u).e(p) = \mu \frac{\partial u}{\partial n}\frac{\partial p}{\partial n} + (\mu + \lambda)\left(\frac{\partial u}{\partial n}.n\right)\left(\frac{\partial p}{\partial n}.n\right) \ on \ \Gamma_D$$

Then,

$$\frac{\partial L}{\partial \Omega}(\Omega, u, p)(\theta)$$

$$= \int_{\Gamma_N} \theta.n\left(j(u) + Ae(u).e(p) - p.f - \frac{\partial(g.p)}{\partial n} - Hg.p\right)ds$$

$$+ \int_{\partial \Omega} \theta.n\left(\frac{\partial l(u)}{\partial n} + Hl(u)\right)ds + \int_{\Gamma_D} \theta.n\big(j(u) - Ae(u).e(p)\big)ds$$

Example 1- Compliance of Structure with Body Force and Pressure

$$J_3(\Omega) = \int_\Omega f.u dx + \int_{\Gamma_N} p_0 n.u \ ds$$

For the proved equation which is on page 367 of (Allaire et al., 2004), equation 8,

$$J(\Omega) = \int_\Omega f.u dx + \int_{\Gamma_N} g.u ds$$

Subject to

$$-\nabla.\big(Ae(u)\big) = f \ on \ \Omega$$

$$u = 0 \ on \ \Gamma_D$$

$$(Ae(u))n = g \ on \ \Gamma_N$$

The shape derivative was proven to be as follows:

$$J'(\Omega) = \int_{\Gamma_N}\left(2\left(\frac{\partial(g.u)}{\partial n} + Hg.n + f.u\right) - Ae(u).e(u)\right)\theta.nds + \int_{\Gamma_D} Ae(u).e(u)\theta.n$$

Now for this problem, $g = p_0 n$, replacing this into the proven shape derivative equation:

$$J_3{'}(\Omega) = \int_{\Gamma_N} \left(2\left(\frac{\partial(p_0 n.u)}{\partial n} + Hp_0 n.n + f.u\right) - Ae(u).e(u)\right)\theta.nds$$

$$+ \int_{\Gamma_D} Ae(u).e(u)\theta.n$$

Then replacing:

$$\frac{\partial(p_0 n.u)}{\partial n} = \nabla(p_0 n.u).n, \text{ and } H = \nabla.n$$

$$J_3{'}(\Omega) = \int_{\Gamma_N} \left(2(\nabla(p_0 n.u).n + \nabla.n \, p_0 n.n + f.u) - Ae(u).e(u)\right)\theta.nds$$

$$+ \int_{\Gamma_D} Ae(u).e(u)\theta.n$$

Then we can replace as follows:

$$\nabla.(p_0 n.u)n + \nabla.n \, p_0 n.n = \nabla.(p_0 n.u.n) = \nabla.(p_0 u)$$

Then,

$$J_3{'}(\Omega) = \int_{\Gamma_N} \left(2(\nabla.(p_0 u) + f.u) - Ae(u).e(u)\right)\theta.nds + \int_{\Gamma_D} Ae(u).e(u)\theta.n \, ds$$

Proved.

Example 2, Cantilever Beam with Force at The Edge

The compliance added to the area multiplied with Lagrangian can be written as follows:

$$J(\Omega) = \int_{\partial D_N} g.uds + L\int_{\Omega} dx$$

Using the proven formula of shape derivative,

$$L = \int_{\Omega} j(u)dx + \int_{\partial\Omega} l(u)ds$$

$$\frac{\partial L}{\partial \Omega}(\Omega, u, p)(\theta)$$

$$= \int_{\Gamma_N} \theta.n \left(j(u) + Ae(u).e(p) - p.f - \frac{\partial (g.p)}{\partial n} - Hg.p \right) ds$$

$$+ \int_{\partial \Omega} \theta.n \left(\frac{\partial l(u)}{\partial n} + Hl(u) \right) ds + \int_{\Gamma_D} \theta.n \big(j(u) - Ae(u).e(p) \big) ds$$

As you can see we can use the formula by first replacing $l(u) = g.u \; and \; j(u) = L$

Also since this problem is self adjoint because using the adjoint state equations,

$$j'(u) = \nabla.(Ae(p)) \; on \; \Omega$$

$$p = 0 \; on \; \Gamma_D$$

$$Ae(p)\vec{n} = -l'(u) \; on \; \Gamma_N$$

Since $j'(u)$=L'=0 and $l'(u)$=g, the adjoint equations will be,

$$0 = \nabla.(Ae(p)) \; on \; \Omega$$

$$p = 0 \; on \; \Gamma_D$$

$$Ae(p)\vec{n} = -g \; on \; \Gamma_N$$

Compare these with the equilibrium equation which are,

$$0 = -\nabla.(Ae(u)) \; on \; \Omega$$

$$u = 0 \; on \; \Gamma_D$$

$$Ae(u)\vec{n} = g \; on \; \Gamma_N$$

It is seen that u=-p , this problem is self adjoint then. We replace p=-u, also we know f=0 because no body force is applied.

$$\frac{\partial L}{\partial \Omega}(\Omega, u, p)(\theta)$$

$$= \int_{\Gamma_N} \theta.n \left(L - Ae(u).e(u) + u.f + \frac{\partial(g.u)}{\partial n} + Hg.u \right) ds$$

$$+ \int_{\partial \Omega} \theta.n \left(\frac{\partial(g.u)}{\partial n} + H(g.u) \right) ds + \int_{\Gamma_D} \theta.n \left(L + Ae(u).e(u) \right) ds$$

Dividing the boundary to Dirichlet Γ_D, non-Homogenous Neumann Γ_N and homogeneous Neumann Γ_0, the Dirichlet boundary and the non-homogenous Neumann are not moving because the load location and the clamped boundary are fixed. Hence all terms on Dirichlet Γ_D, non-Homogenous Neumann Γ_N, are goanna vanish because $\theta.n$=0. Hence,

$$\frac{\partial L}{\partial \Omega}(\Omega, u, p)(\theta)$$

$$= \int_{\Gamma_0} \theta.n \left(L - Ae(u).e(u) + \frac{\partial(g.u)}{\partial n} + Hg.u \right) ds$$

$$+ \int_{\Gamma_0} \theta.n \left(\frac{\partial(g.u)}{\partial n} + H(g.u) \right) ds$$

Also on homogeneous Neumann Γ_0, g=0 hence,

$$\frac{\partial L}{\partial \Omega}(\Omega, u, p)(\theta) = \int_{\Gamma_0} \theta.n \left(L - Ae(u).e(u) \right) ds$$

Proved.

As you saw in the previous slides, you can see that the general form of the shape derivative is as follows:

$$J'(\Omega)(\theta) = \int_{\partial \Omega} v\theta.n \, ds$$

As can be seen to get to the minimum, the shape derivative should be negative to decrease.

Choosing the perturbation as $\theta = -vn$ will ensure the negativity of the derivative

$$J'(\Omega)(\theta) = \int_{\partial\Omega} v(-vn).n \ ds = \int_{\partial\Omega} -v^2 ds$$

$$J'(\Omega)(\theta) < 0$$

If either v or θ is not smooth it is desirable to smooth them.

One way is to solve the following to get the smooth θ:

$$-\nabla^2\theta = 0 \ \ on \ \ \Omega$$

$$\frac{\partial\theta}{\partial n} = -vn \ \ on \ \partial\Omega$$

which means θ is a decent direction.

Because $\int_\Omega |\nabla\theta|^2 dx = -\int v\theta.nds{>}0$

Hence, $\int v\theta.nds{<}0$

Proof:

$$\int_\Omega |\nabla\theta|^2 dx = \int_\Omega \nabla\theta.\nabla\theta dx = \int_\Omega \nabla(\nabla\theta.\theta) - \nabla^2\theta.\theta = \int_{\partial\Omega} \nabla\theta.\theta.\vec{n}ds - \int_\Omega \nabla^2\theta.\theta dx$$

If $-\nabla^2\theta = 0 \ \ on \ \Omega$ and $\frac{\partial\theta}{\partial n} = -vn$ on $\partial\Omega$ then

$$\int_{\partial\Omega} \nabla\theta.\theta.\vec{n}ds - \int_\Omega \nabla^2\theta.\theta dx = -\int_\Omega v\theta.n$$

Numerical Examples

The following examples are the results of above gradient based shape optimization method similar to example 2 above. For different initial conditions, different optimal structures are achieved because gradient based methods find local minima that is near to the initial design as seen in Figure 6.14. Level set method and shape derivative has been used based on legendary work of Allaire et al. (Allaire et al., 2004) .The compliance minimization with weight constraint is carried out in all the examples. This shows how the final design is dependent on the initial design. This can be alleviated by using the topology derivative, which creates holes in the design when the topology derivative is negative. Analytical derivation of topology derivative for different objective functions has been derived in (Soko$f$owski et al., 2001).

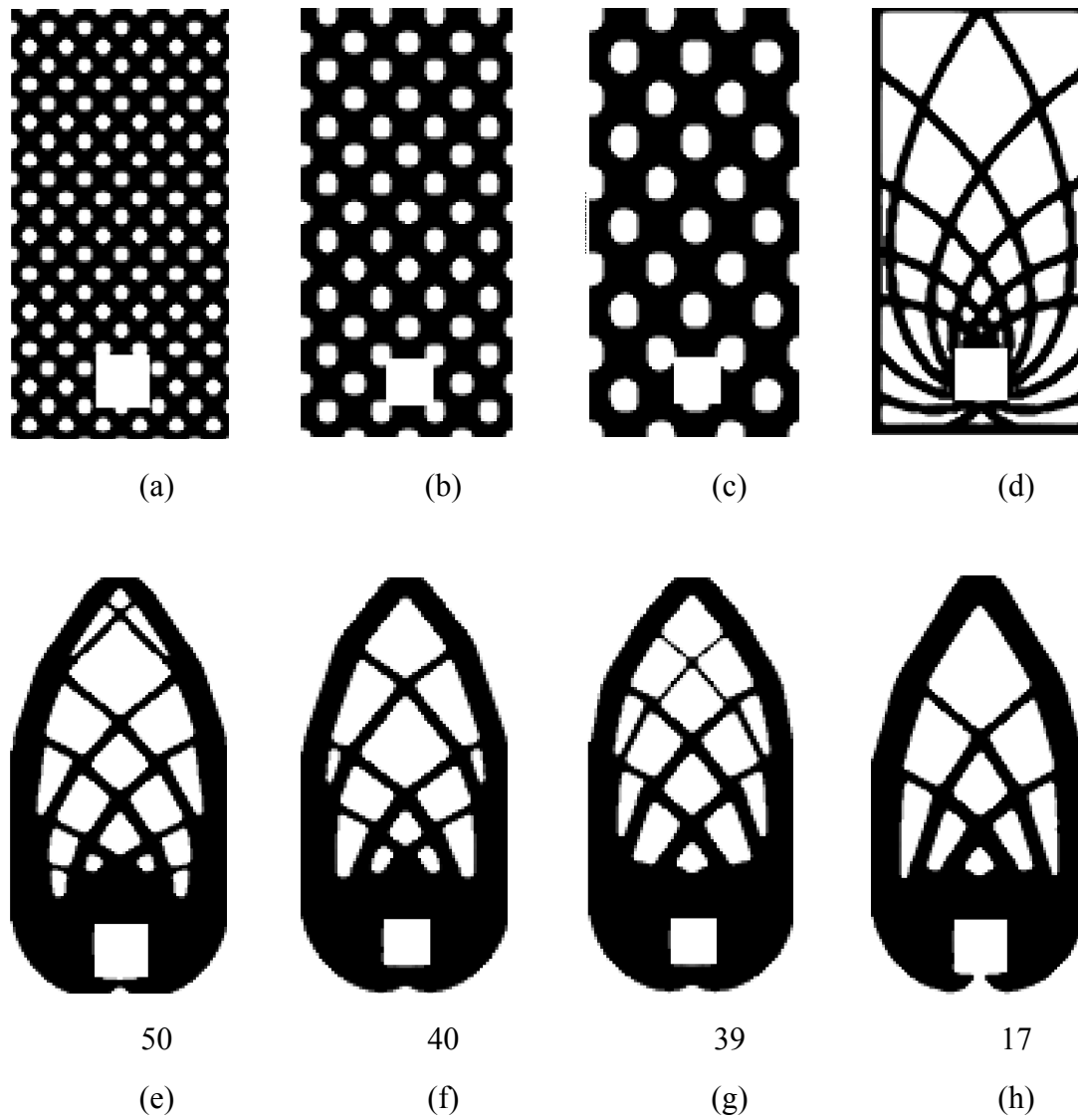Figure 6.13 Load case of a two by one cantilever beam

Figure 6.14 Different Initial designs (a-c) with different hole sizes, and (d) initial design based on principal stress vectors. Different optimal designs (e-f), with different number of iterations to achieve the optimal.